

DISSERTATION
ZUR
ERLANGUNG DER DOKTORWÜRDE
DER
NATURWISSENSCHAFTENLICH-MATHEMATISCHEN
GESAMTFAKULTÄT
DER
RUPRECHT-KARLS-UNIVERSITÄT
HEIDELBERG

VORGELEGT VON

M.Sc. NOZAIR A. KHAWAJA

AUS: WAZIRABAD-PAKISTAN

TAG DER MÜNDLICHEN PRÜFUNG: 22.12.2016

Organic compounds in Saturn's E-ring and its
compositional profile in the vicinity of Rhea

-

Organische Verbindungen in Saturns E Ring und sein
Zusammensetzungsprofil in der Umgebung von Rhea

Gutachter:
PD Dr. Frank Postberg
PD Dr.-Ing. Ralf Srama

Dedicated to my father

Table of Contents

ABSTRACT.....	3
1. INTRODUCTION.....	6
1.1. OVERVIEW.....	6
1.2. THE CASSINI-HUYGENS MISSION	9
1.3. THE SATURNIAN SYSTEM.....	11
1.3.1. <i>Enceladus – Saturn’s active ice world</i>	13
2. METHODS AND INSTRUMENTATION.....	18
2.1. TIME-OF-FLIGHT MASS SPECTROMETRY OF WATER ICE PARTICLES	18
2.1.1. <i>Ion mass separation and calibration of time-of-flight mass spectra</i>	19
2.2. THE DUST IMPACT-IONIZATION MECHANISM	21
2.2.1. <i>The Cassini Cosmic Dust Analyzer—CDA</i>	24
2.2.1.1. The CDA Chemical Analyzer subsystem	25
2.3. ANALOGUE SPECTRA BY WATER DISPERSION AND INFRARED MALDI TIME-OF-FLIGHT MASS SPECTROMETRY (IR-MALDI-TOF-MS)	28
2.3.1. <i>Comparison of molecular fragment clusters between IR-MALDI-MS and CDA</i> ..	29
2.4. BASIC PRINCIPLES OF WATER DOMINATED MASS SPECTRA	30
2.4.1. <i>Compositional types of ice grains in the E ring and the Enceladian plume</i>	34
2.5. METHOD TO DETERMINE THE COMPOSITIONAL PROFILES OF ICE GRAINS AT SATURN	36
3. ORGANIC MATERIAL IN E RING ICE GRAINS.....	38
3.1. INTRODUCTION	38
3.1.1. <i>CDA mass spectra of organic enriched E ring ice grains</i>	38
3.2. RESULTS.....	41
3.2.1. <i>Identification of amine species in E ring ice grains</i>	42
3.2.1.1. Laboratory measurements.....	42
3.2.1.2. Amine species as seen in CDA Type-2 spectra	45
3.2.2. <i>Identification of carbonyl species in E-ring ice grains</i>	47
3.2.2.1. Laboratory measurements.....	48
3.2.2.2. Carbonyl species as seen in CDA Type-2 spectra	52
3.2.3. <i>Identification of aromatic species in E-ring ice grains</i>	54
3.2.3.1. Laboratory measurements.....	54
3.2.3.2. Aromatic species as seen in CDA Type-2 spectra.....	63
3.2.3.3. Complex aromatic material.....	65
3.3. DISCUSSION AND CONCLUSION	67
3.3.1. <i>Amines</i>	67
3.3.2. <i>Carbonyls</i>	68
3.3.3. <i>Aromatics</i>	69
3.3.3.1. N- or O- bearing fragments ions	70
3.3.3.2. High mass cations	71
4. COMPOSITIONAL MAPPING OF THE E RING IN THE VICINITY OF RHEA	73
4.1. INTRODUCTION	73
4.1.1. <i>The impactor-ejecta mechanism</i>	74
4.1.2. <i>The flyby geometry</i>	75
4.2. METHODS.....	76
4.2.1. <i>Classification of Spectra</i>	76
4.2.2. <i>Spectral count database</i>	77
4.3. RESULTS.....	78
4.3.1. <i>Compositional profiles</i>	79
4.3.1.1. Size dependent compositional profile.....	80
4.4. DISCUSSION AND CONCLUSION	86

5. SUMMARY	89
REFERENCES	93
ACKNOWLEDGEMENT	100

Abstract

The general topic of this dissertation is the analysis of impact ionization time-of-flight mass spectra of ice grains in Saturn's E ring sampled in-situ by the Cosmic Dust Analyzer (CDA) onboard the Cassini-Huygens spacecraft. The source of these E ring ice grains is the subsurface ocean of Saturn's cryo-volcanically active icy moon Enceladus. The Chemical Analyzer subsystem of CDA generated mass spectra of cations that form when the ice grains impinge onto the instrument's target plate with high speed.

The first aim of this work is a detailed compositional analysis of the organic material in the ice grains ejected from subsurface Enceladus' into the E ring. Many of these ice grains carry diverse organic material that is characterized in this work. A laser-based analogue laboratory experiment is used to simulate the impact ionization CDA spectra of ice grains enriched in organic material. This experiment allowed to understand the varying cationic fragmentation patterns from organic material in a water ice matrix. Despite the relatively low mass resolution of the CDA, results of the analogue experiment allow to identify characteristic finger prints of certain classes of organic compounds in many CDA mass spectra. Three main categories are classified: (i) Amine-, (ii) Carbonyl-, and (iii) Aromatic-type mass spectra. Furthermore, some aromatic-type CDA spectra show features that correspond to breakup-products of larger complex aromatic species with masses above 200u. On the whole, the analysis of E ring ice grains in this work gives first insights into the largely varying and complex organic chemistry inside the ocean of Enceladus.

The second aim of this thesis is to infer the compositional profile of ice particles in the E ring in the vicinity of Saturn's moon Rhea, from a series of spectra recorded on Cassini's Rhea flyby (R4) in 2013. No striking change in the frequency of different compositional types is observed along the spacecraft trajectory. However, a varying size distribution of different compositional populations of ice grains is observed and discussed. Sodium salts and organic compounds are more frequent in relatively large ice grains, whereas pure water ice particles become more abundant in smaller E ring grains. A generally higher number density of ice grains is observed in the close vicinity of Rhea, which might indicate either the presence of an ejecta cloud from Rhea's surface or a general confinement of particles near the equatorial plane of the E ring.

Zusammenfassung:

Das übergreifende Thema dieser Dissertation, ist die Analyse von Einschlagsionisations-Flugzeit-Massenspektren von Eispartikeln in Saturns E ring, die vom Cosmic Dust Analyzer (CDA) in situ an Bord der Raumsonde Cassini-Huygens aufgenommen wurden. Die Quelle dieser E ring Eispartikel ist der Ozean unterhalb der Eiskruste von Saturns cryo-vulkanisch aktivem Mond Enceladus. Das Chemical Analyzer Subsystem des CDA erzeugt Massenspektren von Kationen die beim Hochgeschwindigkeitseinschlag dieser Eispartikel auf die Prall-Platte des Instrumentes entstehen.

Das erste Ziel dieser Arbeit ist eine detaillierte Analyse der Zusammensetzung von organischem Material in den Eispartikeln, die von Enceladus' in den E Ring geschleudert werden. Viele dieser Eispartikel enthalten verschiedene organische Verbindungen, die in dieser Arbeit näher charakterisiert werden. Dabei wird ein Laser-basiertes Analogexperiment verwendet, um die Einschlagionisations-Massenspektren des CDA von organisch angereicherten Eispartikeln zu simulieren. Dieses Experiment stellte sich als entscheidend heraus, um die verschiedenen kationischen Fragmentationsmuster organischer Moleküle in einer Wassereismatrix zu verstehen. Trotz der relativ geringen Massenauflösung des CDA ermöglicht es das Analogexperiment, charakteristische „Fingerabdrücke“ bestimmter organischer Substanzklassen in vielen CDA Massenspektren zu identifizieren. Drei Hauptkategorien werden klassifiziert: (i) Amine, (ii) Carbonyle und (iii) Aromatisch. Des Weiteren zeigten einige der CDA Spektren des aromatischen Typs, Merkmale, die Bruchstücken weit größerer aromatischer Verbindungen, mit Massen jenseits von 200u, zugeordnet werden können. Zusammengenommen gibt die hier vorgenommene Analyse von E Ring Eisteilchen, erste Einblicke in eine äußerst variantenreiche und komplexe organische Chemie des Enceladusozeans.

Das zweite Ziel dieser Arbeit besteht darin, anhand einer Serie von Spektren, die bei Cassini's Rhea-Vorbeiflug (R4) im Jahre 2013 aufgenommen wurde, das Zusammensetzungsprofil der Eispartikel des E Ringes in der Nähe des Saturnmondes Rhea zu ermitteln. Es werden keine auffälligen Änderungen in der Häufigkeit verschiedener Zusammensetzungstypen entlang der Trajektorie der Raumsonde festgestellt. Allerdings wird eine unterschiedliche Größenverteilungen der verschieden zusammengesetzten Eisteilchen-Populationen festgestellt und diskutiert. Salze und organische Komponenten

sind häufiger in größeren Eispartikeln zu finden, während die Häufigkeit purer Wassereisteilchen in kleinen Eispartikeln zunimmt. Generell wird eine erhöhte Anzahldichte von Eisteilchen in der Nähe von Rhea gemessen, was entweder auf das Vorhandensein einer Ejekta Wolke von Rhea's Oberfläche oder auf eine generelle Konzentration von Partikeln in der Nähe der äquatorialen Ringebene hinweist.

1. Introduction

1.1. Overview

Dust particles in the universe play an important role in many astrophysical phenomena as extinction and polarization of starlight, zodiacal light, comet's tails, and probably also the abiotic synthesis of complex organic molecules ((Austin, 2003) & (Greenberg & Caro, 2000)). The sizes of the particles vary between few tenths of nm up to 200 μ m and can be classified as: interstellar, interplanetary and planetary dust particles ((Grün et al., 1994) & (Mocker, 2011)).

The interstellar dust (ISD) is defined as particulate matter outside of the solar system. The ISD grains are created in the cool atmospheres of red giants (Binney & Merrifield, 1998), supernova explosions (Amari & Lodders, 2007) and carbon-rich stars ((Grün et al., 2000), (Austin, 2003) & (Dorschner & Henning, 1995)). The grains are considered as the building blocks of next generation stars and planetary systems and are continuously recycled by the galactic evolution process (Dorschner & Henning, 1995).

The dust within the solar system is referred as interplanetary dust (IDP). IDPs travel on different orbits between planets of the solar system. There are number of IDP sources including cometary debris, planetary rings, collisions of larger bodies in asteroid and Kuiper belt and, also planets and moons without an atmosphere (Hillier et al., 2007a).

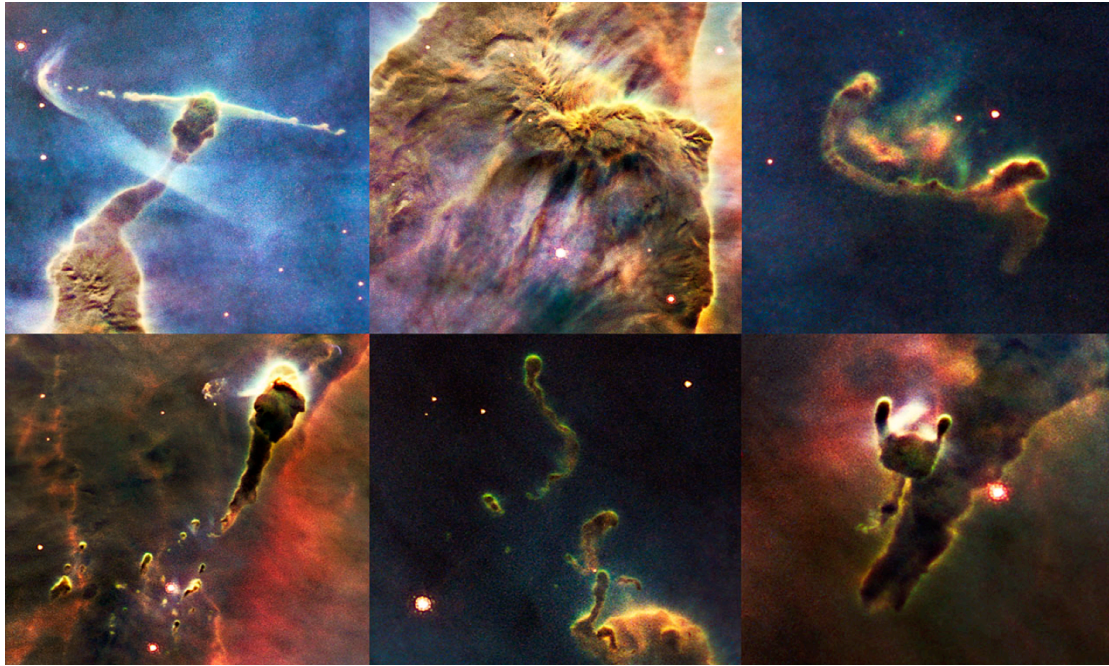


Figure 1.1 (Adapted from (NASA/ESA, 2010)): *Complex gas structures laced with dust in Carina Nebula. The UV light from young stars erodes the cloud of dust and gas.*

Another important type of cosmic dust is the planetary dust, which is normally bounded by the gravity of a central body—planet or its moon(s). The planetary dust is known from the dust rings of the gas giants—Jupiter and Saturn as well as the ice giants—Uranus and Neptune. Earth bound remote sensing investigations of the planetary environments provide very limited detail about the composition and dynamics of the planetary dust grains of the outer planets. Therefore, various spacecrafts have been sent out for in-situ measurements of the planetary dust grains since the early seventies (Grün et al., 1980). A number of dust detectors have been launched on interplanetary spacecrafts e.g., Ulysses, Galileo (Grün et al., 1992a & 1992b) & (Krüger et al., 2005)) and Cassini (Srama et al., 2004). In contrast to Ulysses and Galileo, the dust detector on the Cassini spacecraft is capable not only to investigate the dynamic properties (Kempf et al., 2008) but also the composition of ice/dust grains (Figure 1.2) ((Hillier et al., 2007b), (Postberg et al., 2008 & 2009a), (Hsu et al., 2015) & (Altobelli et al., 2016)).

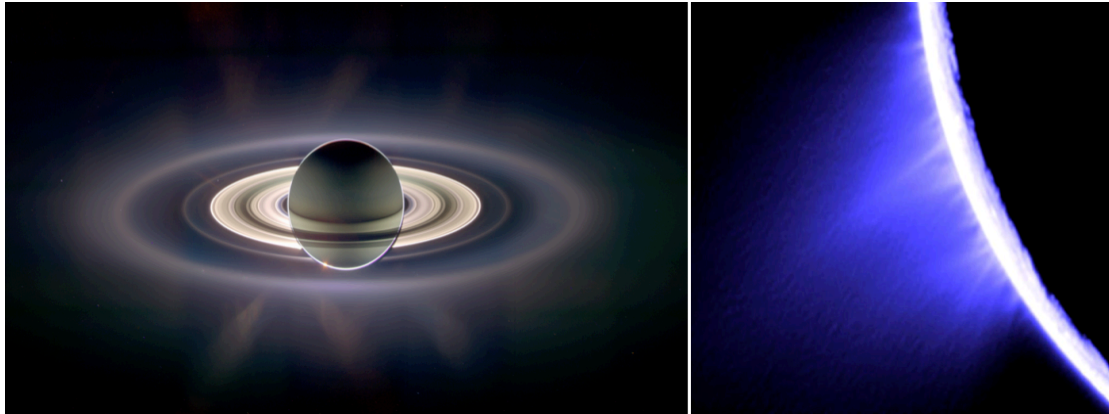


Figure 1.2 (credit: NASA/JPL): *(Left) Global view of Saturn and its rings system. The wide-angle camera aboard the Cassini spacecraft took the image. The diffused bluish outer E-ring along with the orbit of moon Enceladus is visible. (Right) Dust plumes emitting from the fractured zone near the south pole of Enceladus.*

In this thesis, the focus is on the chemical analysis of dust/ice grains of Saturn's E-ring and Enceladus' plume sampled by the Cosmic Dust Analyzer (CDA) onboard the Cassini spacecraft. The CDA's time-of-flight mass spectrometer provided in-situ impact ionization mass spectra to characterize the composition of the sampled ice grains.

The thesis consists of 5 chapters and structured as follows. The first chapter gives an introduction of the Cassini-Huygens mission and the Cassini spacecraft. Then follows a brief introduction of the Saturnian system with the focus on Saturn's E-ring and its moon—Enceladus. The second chapter focuses on the methods and instrumentation. There, the basic principle of time-of-flight mass spectrometry is described, followed by an introduction of the Cosmic Dust Analyzer (CDA) with a special focus on its Chemical Analyzer (CA) subsystem. It also covers the description of the laser experiment that was used to simulate spectra from CDA with analogue materials. The basic ideas from previous work on mass spectra of the E-ring water ice grains conclude the second chapter. In the first result section, Chapter three covers the major science investigation of this thesis and provides a detailed insight into the diverse organic materials found in many E-ring ice grains. Here, CDA mass spectra of organic enriched E-ring ice grains are classified into three classes corresponding to three different groups of organic compounds. The characteristics 'finger prints' of organic compounds in CDA spectra are compared with analogue laboratory mass spectra. In chapter four the compositional profile of the E-ring is measured based on a Cassini's flyby of Saturn's icy moon Rhea. The search for particle ejected from the moon's surface by micrometeorite bombardment is also discussed. In chapter

five a conclusive summary of the results of this thesis and an outlook for future work is presented.

1.2. The Cassini-Huygens mission

The Cassini-Huygens mission is a NASA-ESA-ASI flagship class mission that was launched towards the outer planets to intensely study the Saturnian system. The mission was named after the Giovanni Domenico Cassini—a French-Italian astronomer and Christian Huygens—a Dutch astronomer. The spacecraft was launched in 1997 and entered in the orbit around Saturn in 2004 (Figure 1.3). The mission will end in September 2017. The primary objectives of the mission include the exploration of the structure and dynamics of the Saturn’s rings system, the dynamics of Saturn’s magnetosphere and atmosphere, icy satellites’ surfaces and their geological history, the nature of dark material on Iapetus and Titan’s surface and atmosphere. Enceladus initially was not a particular relevant mission goal, but Cassini’s discoveries certainly made it one of the most important scientific objects Cassini explored in the course of the mission.

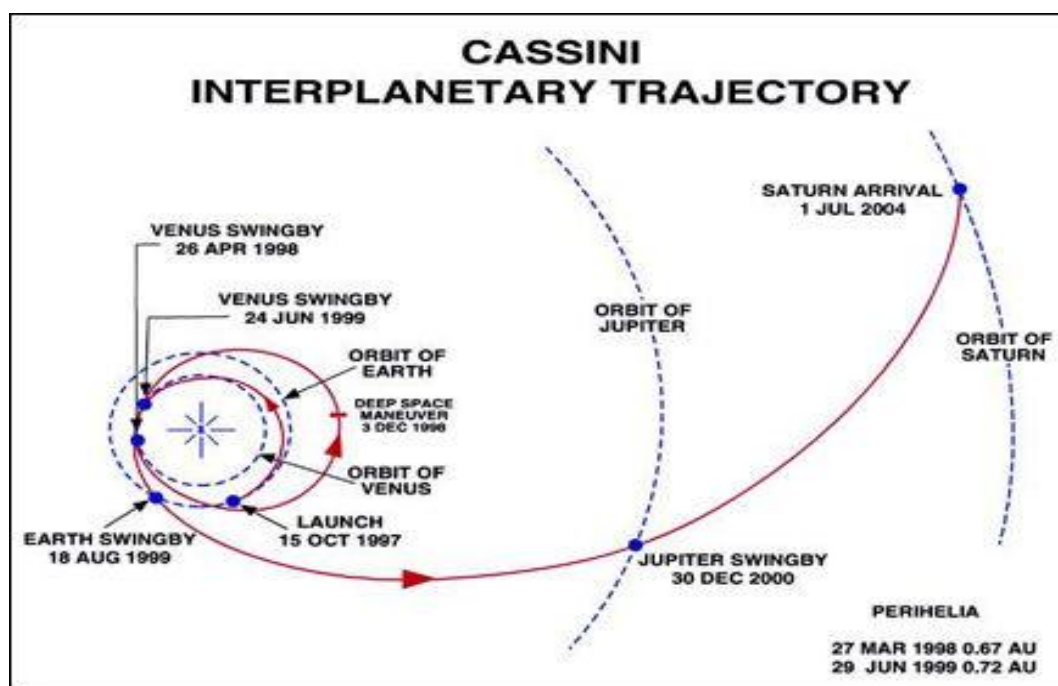


Figure 1.3 ((Fiege, 2013), (Postberg, 2007) & NASA/JPL): *Shown is the trajectory of Cassini spacecraft from Earth to Saturn.*

To achieve the mission goals the orbiter (Cassini) is equipped with a number of versatile instruments (Figure 1.4):

- Cassini Plasma Spectrometer (CAPS) performs in-situ measurement of plasma inside Saturn and in the surroundings.
- Cosmic Dust Analyzer (CDA) carries in-situ investigation of dust grains in the Saturnian system.
- Dual Technique Magnetometer (MAG) measures the magnetic field of Saturn and its interaction with the solar wind.
- Ion and Neutral Mass Spectrometer (INMS) performs in-situ analysis of the composition of charged and neutral particles inside the magnetometer.
- Magnetospheric Imaging Instrument (MIMI) takes images of global magnetosphere and also performs in-situ measurements of Saturn's magnetosphere and its interaction with solar wind.
- Radio and Plasma Wave Science (RPWS) measures electric and magnetic fields and as well it measures the electron density and temperature in the interplanetary medium and inside the Saturn's magnetosphere.
- CASSINI Radar (RADAR) performs radar imaging, altimetry and as well passive radiometry on the surface of Titan.
- Composite Infrared Spectrometer (CIRS) performs infrared studies of the temperature and composition of surfaces, atmospheres and the Saturnian rings.
- Imaging Science Subsystem (ISS) takes multispectral images of Saturn, Titan, rings and icy satellites in visible light.
- Radio Science Instrument (RSS) studies the atmosphere and structure of rings. In addition, it measures gravity field and gravity waves.

- Ultraviolet Imaging Spectrograph (UVIS) takes ultraviolet spectra and low-resolution images of the atmospheres and rings for the study of structure, chemistry and composition.

In addition to the above-described suit of instruments on the orbiter, Cassini, the spacecraft also carried the Huygens Probe that was dropped to the surface of Titan to explore its atmosphere and surface.

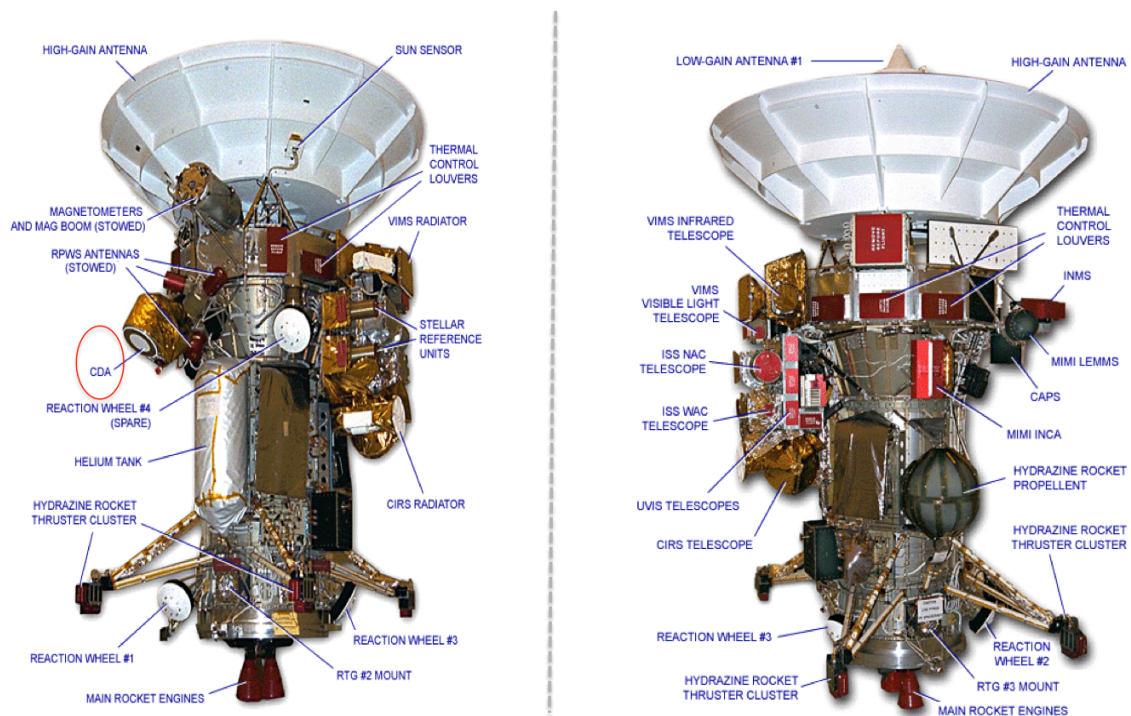


Figure 1.4 (Credit: NASA): The Cassini spacecraft with the onboard suit of instruments. (Left) Plus-Y side of the spacecraft. (Right) Minus-Y side of the spacecraft. The Cosmic Dust Analyzer (CDA) is visible on +Y side of the spacecraft.

1.3. The Saturnian system

Saturn is the sixth planet from the Sun and second-largest after Jupiter. Saturn possesses the most significant ring system in the solar system (Figure 1.5). The shape of Saturn is an oblate spheroid due to its rapid rotation and the quasi-fluid state. The polar radius differs by almost 10% from the equatorial radius (Kempf, 2007). The Saturnian atmosphere is mainly composed of hydrogen. Above the rocky core Saturn has a metallic layer of hydrogen followed by a layer of molecular super critical hydrogen ((Courtin et al., 1984) & (Kempf, 2007)).

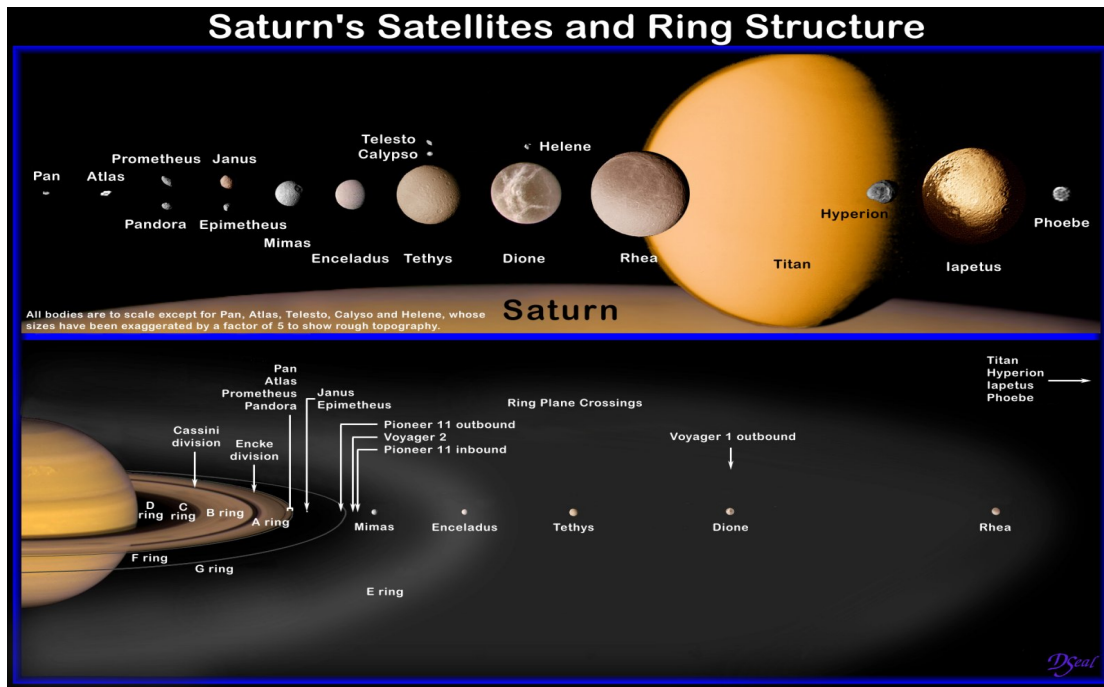


Figure 1.5 (Adapted from (Seal, 2004)): *Illustration of Saturn, its rings and satellites.*

The mean density of Saturn is less than water, which is the lowest among all planets of the solar system. Saturn atmosphere displays bands that are close to the planet's equator and since 2010 also exposes a Great White Spot on its northern hemisphere due to a storm with a periodicity of about 30 years. There is a warm polar vortex at the North Pole, which is characterized by a significant hexagonal wave ((Godfrey, 1988) & (Kempf, 2007)).

In 1610 Galileo Galilei discovered the vast rings system of Saturn and later between 1655-1659 Christian Huygens explored the true nature of the rings. He discovered also the Saturn's largest satellite, Titan. As shown (Figure 1.5), the main ring system consists of two broad rings, A and B, and the two optically thinner rings C and D. During the years 1671-1684 Giovanni Domenico Cassini discovered the gap between the A and B rings known as the Cassini division. He also discovered the moons—Dione, Iapetus, Rhea and Tethys. Wilhelm Herschel calculated the thinness of the rings and also for the first time observed Saturn's moons Mimas and Enceladus in 1789. James Maxwell, in 1857, discovered that the rings are composed of individual particles orbiting Saturn and are not solid structures.

Saturn's tenuous E ring is the second outermost ring after the so called 'Phoebe ring' (Verbiscer et al., 2009). Being much larger than the main rings, the diffuse E

ring extends from $\sim 3.1 R_s$ to $20 R_s$ (Saturn radius $R_s = 60,330$ km) and consists mostly of μm and sub- μm sized icy dust particles. As shown in figure 1.5, E ring surrounds Saturn's icy moons Mimas ($r_M = 3.07 R_s$), Enceladus ($r_E = 3.95 R_s$), Tethys ($r_T = 4.88 R_s$), Dione ($r_D = 6.25 R_s$), and Rhea ($r_R = 8.73 R_s$) (Kempf et al., 2008) and extends further outward to Titan's orbit ($r_T = 20 R_s$). In 1981, Enceladus was proposed as the dominant source of the E ring because of the edge-on brightness profile peaks near the Enceladian mean orbital distance (Baum et al., 1981). Later, Saturn's moon Tethys was identified as a secondary source of E ring (de Pater et al., 2004). One of the important findings was the blue color of E ring (Larson et al., 1981), indicative of the small particles it is made from. With the first in situ measurements of Cassini water ice was found as the dominating material in the E ring (Hillier et al., 2007b).

1.3.1. Enceladus – Saturn's active ice world

Five mid-sized Saturn's moons (Figure 1.6) Mimas, Enceladus, Tethys, Dione and Rhea orbit within Saturn's E ring, beyond the main ring system. These are nearly spherical moons and have relatively low density and high albedo. The interiors of these moons are made-up of water ice surrounding a small silicate core, whereas the surfaces are composed mainly of water ice (Spencer & Nimmo, 2013).

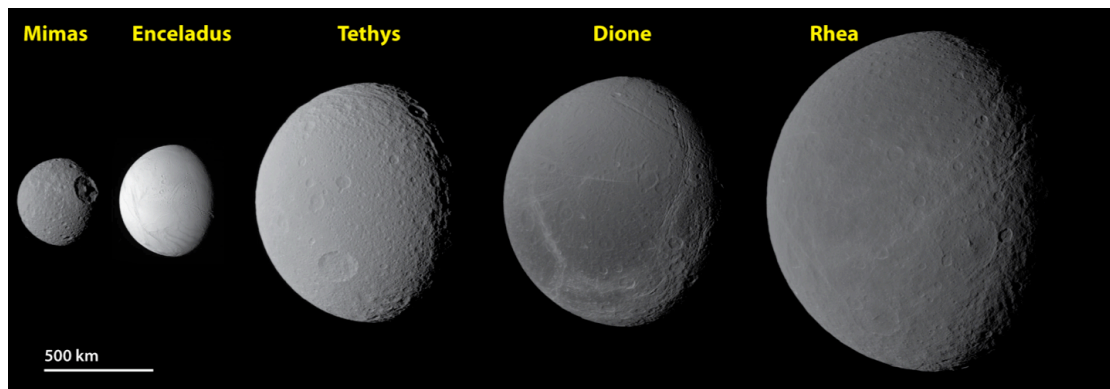


Figure 1.6 (Adapted from (Spencer & Nimmo, 2013), graphics by E. Lakdawalla): Shown are five mid-sized satellites embedded in E ring, which are scaled with relative brightness.

All surfaces of moons in the E ring, except Enceladus, are dominated by impact craters (Figure 1.6) and have been considered as geologically inactive for billions of years. The high albedo and relatively young uncratered geology of wide areas on Enceladus was discovered during Voyager Saturn flybys ((Smith et al., 1982) & (Spencer & Nimmo, 2013)). In 2004-05 Cassini performed number of flybys of

Saturn's icy satellites. Clearly the most spectacular discovery was the geological activity near Enceladus' south pole.

An anomaly in the magnetic field near Enceladus observed by the Cassini Magnetometer (Dougherty et al., 2006) in February 2005, led to a closer flyby to investigate the phenomenon. On 14 July 2005 Cassini performed a flyby of Enceladus with the closest approach of ~ 168 km from the moons surface. The onboard Cassini's Imaging Science Subsystem (ISS) acquired images of Enceladus' South Polar Terrain (SPT) and discovered jets of icy particles (Figure 1.7) emitting from 135 km long fractures, situated at $\sim 55^\circ$ S latitude (Porco et al., 2006). The Composite Infrared Spectrometer (CIRS) aboard Cassini pointed out endogenic activity from SPT. The CIRS instruments detected 3 to 7 gigawatts of thermal emission from the SPT centered on the four linear stripes (Figure 1.8), the so called "tiger stripes" (Spencer et al., 2006). The High Rate Detector (HRD) of the Cosmic Dust Analyzer (CDA) onboard Cassini observed great increase in the flux of icy dust particles jettisoned from Enceladus' south pole into space (Spahn et al., 2006). The analyses made clear that many of these ice particles escape Enceladus' gravitational influence and form the E ring. Likewise, the onboard Ion and Neutral Mass Spectrometer (INMS) detected water gas emerging from the same surface area (Waite et al., 2006). The onboard Ultraviolet and Imaging Spectrograph (UVIS) observed the gas plume (Hansen et al., 2006).

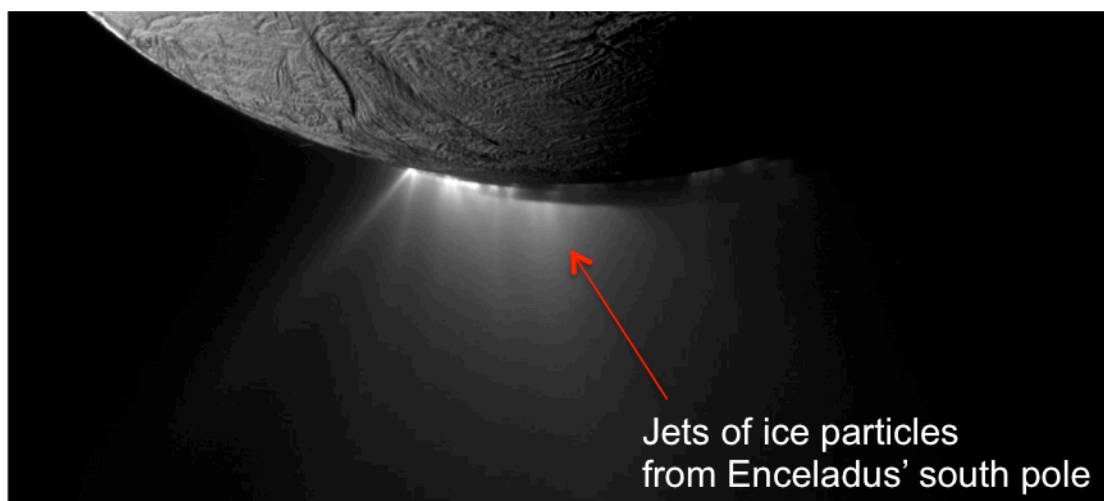


Figure 1.7: *Cassini narrow-angle camera image of Enceladus' south pole. Jets of ice particles and vapours are emanating from the south polar terrain.*

A model of the formation of ice grains inside Enceladus was proposed in 2008. According to the model (Schmidt et al., 2008), the grains condense and grow

from vapour in vertical ice channels of variable width under Enceladus surface, which in turn suggested the liquid water beneath Enceladus south pole. Amongst others ((Collins & Goodman, 2007), (Nimmo et al., 2007), (Tobie et al., 2008) & (Patthoff & Kattenhorn, 2011)), the discovery of salt rich ice grains in E ring gave the first solid evidence of an ocean below the surface of Enceladus (Postberg et al., 2009a). A distinct family of CDA spectra was identified by Postberg et al., 2009(a) showing a pattern of mass lines that reflected high sodium content in many E-ring ice grains. These spectra exhibited mass lines representing sodium salts e.g., NaCl, NaHCO₃ and/or Na₂CO₃. Dissolved Na-salts from the Enceladian rock core remain in the liquid phase and therefore, these spectra strongly suggested an existing liquid source in direct connection to the plume material. A liquid dispersion model was used for the formation of Na-rich grains, where aerosol-like droplets are formed due to upward movements of plume gases (CO₂, N₂, CO, CH₄) and subsequent bubble bursting when reaching the water table that is standing in ice channels inside the icy crust hundreds of meters or a few km below the surface (Postberg et al., 2009a & 2011a).

Based on Doppler from Cassini's main antenna data obtained during three Cassini's flybys of Enceladus, the quadrupole gravity field of Enceladus and its hemispherical asymmetry was determined. A negative anomaly was observed in the south polar terrain that was greatly adjusted by a positive subsurface anomaly and it was consistent with the presence of regional subsurface ocean. The suggested depth of ocean ranged 30 to 40 km and extended up-to 50° of southern latitudes. However, these findings did not rule out the presence of a global subsurface ocean. The estimated value of moment of inertia $0.335MR^2$ (where M is the mass and R is the radius of Enceladus) indicated that Enceladus is a differentiated body with a low-density and probably porous core. (Iess et al., 2014).

Furthermore, Enceladus' precise rotation state was determined from different control points across the surface of Enceladus over the period of seven years. The estimated forced physical libration of Enceladus ($0.120 \pm 0.014^\circ$) was too high to be consistent with the possibility of a rigid connection between core and crust, only plausible with the existence of a global ocean (Figure 1.8) that decoupled the ice shell from the rocky core (Thomas et al., 2016). In addition, the re-interpretation of gravity data along with a higher-order rotational corrections also proposed a thin and a wide spread subsurface ocean (McKinnon, 2015).

Cadek et al., 2016 developed a model of Enceladus' interior structure by taking into account an ice shell, an internal ocean and a rocky core, which satisfied liberation, shape and gravity data. These data sets were synchronized by considering isostatic compensation of surface topography together with the effect of a few hundred meter thick elastic lithosphere. The results implied the subsurface ocean density of $\sim 1030 \text{ kg m}^{-3}$ and the ocean volume of $\sim 40\%$ of the total volume. The model predicted the core radius of $\sim 180\text{--}185 \text{ km}$ and the average thickness of ice shell $\sim 18\text{--}22 \text{ km}$. Particularly, at the south polar region it suggested an average thickness of ice shell of only 2 to 5 km. (Cadek et al., 2016).

The discovery of salt rich ice grains, the measurements of gravitational fields and the satellite's precise rotational state all indicated that the ocean is in contact with the core and thus intense rock-water interactions inside Enceladus occur. The CDA analysis of nanometer-sized silica (SiO_2) particles from Enceladus' even implied on going hydrothermal activity within the satellite (Hsu et al., 2015 & Sekine et al., 2015) (Figure 1.8). In a plausible scenario for hydrothermal activity, alkaline hot water ($\text{pH} \sim 8\text{--}10.5$ & $T \geq 90 \text{ }^\circ\text{C}$) flows through silicate rocks on the Enceladian ocean floor or inside the porous core and dissolves silica. This hot water-silica solution flows out into the ocean and cools down as it contacts with the surrounding water. At this stage, colloidal nano-silica particles form with an initial radii of $\sim 1\text{--}1.5 \text{ (nm)}$. Under the alkaline conditions and moderate salinity ($< 4\%$) the nano-silica colloid cannot grow further quickly to macroscopic grains and does not precipitate. Instead they grow slowly to radii of $\sim 6\text{--}9 \text{ (nm)}$ by the addition of dissolved silica and also by a spontaneous process of particle's growth in a colloidal suspension known as Ostwald ripening. These nano grains float with the large scale thermal convection and are transported from the bottom of the ocean to the water table, from where these ascend into the ice channels and are finally ejected, embedded in ice grains, into the E-ring. The plasma sputtering erosion of these E-ring ice grains releases the embedded nano-silica particles, which were detected by Cassini's CDA.

The CDA mass spectra of these particles showed silicon as the most significant particle constituent and oxygen as the second abundant specie but no metals, which is in agreement with the composition of pure silica (SiO_2) particles. The detection of these nano-silica particles up to radii $\sim \leq 9 \text{ nm}$ strongly indicates on-going hydrothermal activity at Enceladus and provides an opportunity to probe directly into the Enceladus' subsurface ocean in present time. (Hsu et al., 2015).

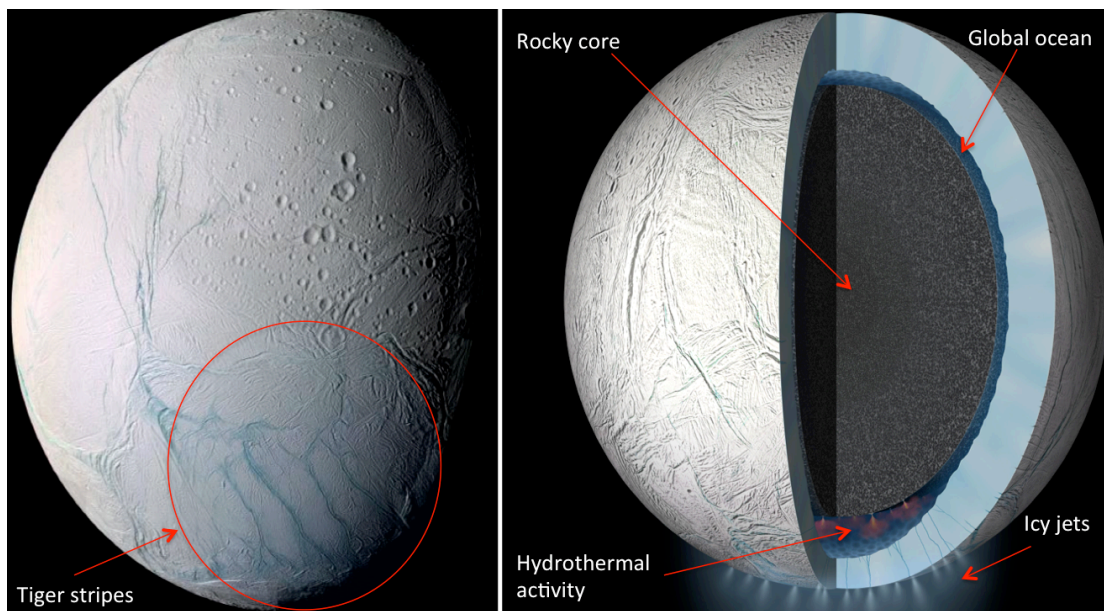


Figure 1.8 (Adapted and modified from NASA/JPL): (Left) Shown is the false-color view of the anti-Saturn hemisphere of Enceladus. The craters and complex fractured terrain (tiger stripes) near moon's south pole is visible. (Right) Artistic view of the interior of Enceladus. The global ocean and hydrothermal activity are indicated here. Enceladus is emitting a plume of ice particles, water vapours and organic molecules from the south polar fractured zone.

The Cassini's instruments (INMS and CDA) already provided evidences of an organic enriched Enceladian plume gas and ice grains ((Waite et al., 2009), (Postberg et al., 2008, 2009a & 2011a)), which indicate interesting subsurface chemistry and may be even prebiotic chemistry. As a major aim of this thesis I will discuss in-depth compositional characterization of organic enriched ice grains that can be used by future work to explore the habitability of Enceladus.

2. Methods and instrumentation

In this chapter, I will describe an overview of the principles of Time-of-Flight Mass Spectrometry (ToF-MS) and the impact ionization process of water ice particles. Further, I will introduce the Cosmic Dust Analyzer (CDA) and the Chemical Analyzer (CA) subsystem, which performs in situ measurements of ice and dust particles in the Saturnian system. The description of an analogue laboratory set up to simulate water ice spectra with an Infrared MALDI Mass Spectrometer (IR-MALDI-MS) is an important part of the following section. In the end, I will discuss the basic principle of the clustering mechanism as seen in CDA water dominated mass spectra as well as in the analogue experiment. Based on this understanding, the basic compositional types of the ice grains in the E ring and the Enceladian plume will be introduced.

2.1. Time-of-flight mass spectrometry of water ice particles

In TOF-MS, ions from the analyte are accelerated by an electric field and subsequently move in the same direction at a constant kinetic energy. The distribution of ion masses corresponds to their velocities (and thus their 'time-of-flight' to cross a certain distance), where the velocity of an ion is inversely proportional to its mass-to-charge ratio $\sqrt{m/q}$ (Guilhaus, 1995).

A simple TOF mass spectrometer (Figure 2.1) works in three steps; i) transforms sample material into ions, ii) accelerate ions and finally iii) separate ions by measuring their mass-to-charge (m/q) ratios in terms of their times of flight, in a field free drift region (Thomson, 1913).

In a general setup of a TOF mass analyzer the distance "s" between the source plate and grid I is of the order of a few centimeters. The electric field in the source region depends on the potential difference between the source plate and the grid I. Under the influence of the potential difference $E = U_{acc}/s$ ions accelerate through the source region and drift through a field free region "d",

between the grids I & II, with velocities inversely proportional to the square root of their mass-to-charge ratios (m/q). Therefore, ions with lower m/q have higher velocities and hence arrive at the detector faster than the ions with higher m/q (Figure 2.1).

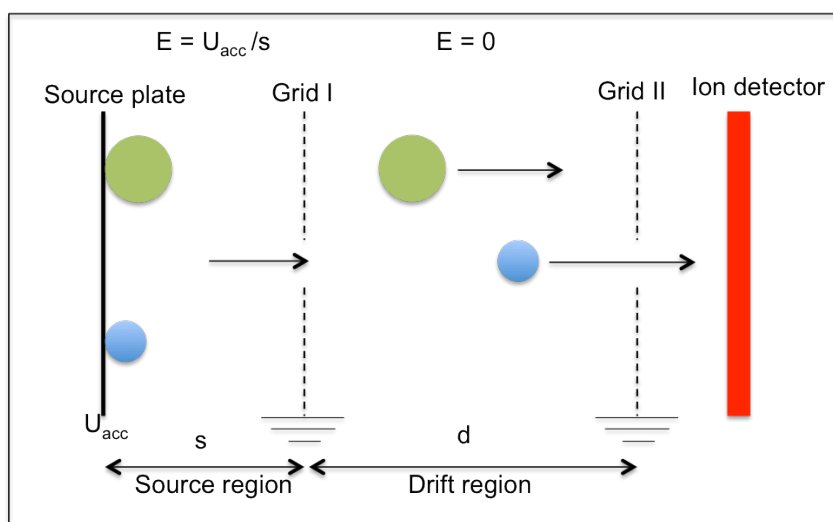


Figure 2.1 (After (Mocker, 2011)): Shown is the basic principle of a TOF mass analyzer. The setup consists of two main regions: the source and the drift region. The green sphere represents the heavier ion and the blue sphere corresponds to the lighter ion.

Upon impact of ion species of a certain mass, the detector produces a specific current that is measured as a function of time and converted into a mass spectrum. The resultant mass spectrum shows the relative intensity of the current signal over the mass to charge ratio of the detected ions.

2.1.1. Ion mass separation and calibration of time-of-flight mass spectra

Generally, the formation of ions takes place in an ionization region at a certain instant. Ions that emerge from the source plate at zero initial energy are accelerated through the source region, until they reach the verge of the drift region with a uniform energy (Cameron & Eggers, 1948).

$$\frac{1}{2}mv^2 = q \cdot U_{acc}$$

Here, " U_{acc} " is the accelerating potential in the source region; " m " is the mass and " v " is the final velocity of the ion.

$$v = \sqrt{\frac{2qU_{\text{acc}}}{m}}$$

The above equation shows an inverse relation of mass and velocity, which is the governing principle of separation of ions in time. In case of single charged ions, smaller ions move faster in the drift region of a mass analyzer and get separated from larger slower moving ions. The accelerated ions cover the distance d in the drift region with a uniform velocity v and arrive at the detector at time t that depends on the square root of the mass of ions.

$$t = \sqrt{\frac{d^2}{2qU_{\text{acc}}}} \cdot \sqrt{m}$$

The above equation shows the time-of-flight of an ion through the drift region of a mass spectrometer. The rearrangement of the equation provides the conversion of the time-of-flight of an ion into the mass-to-charge ratio, as shown below.

$$\frac{m}{q} = 2U_{\text{acc}} \left[\frac{t}{d} \right]^2$$

Providing the dimension “ d ” of the drift tube and the accelerating potential “ U_{acc} ”, the “ m/q ” ratio of an ion can be determined by the time-of-flight “ t ”. Based on the empirical determination of the TOF of known masses, the equation of mass calibration is formulated for the calibration of TOF mass spectra.

$$\frac{m}{q} = at^2 + b$$

$$t = b + a \cdot \sqrt{\frac{m}{q}}$$

Here the stretch parameter “ a ” is the constant of proportionality, which is related to the instrument’s field strength and determined by the physical setup of the instrument. The shift parameter “ b ” corresponds to any offsets in the time span between the triggering of the mass analyzer and the start of the spectrum.

Both “a” and “b” parameters can be evaluated by fitting “n” assigned mass lines to their corresponding mass lines via a least square linear regression, which converts the detector’s output current into a mass spectrum. In another approximation, both parameters can be derived from the following equation by fitting two-assigned mass lines “t₁” and “t₂” to masses “m₁” and “m₂”.

$$t_2 - t_1 = a (\sqrt{m_2} - \sqrt{m_1})$$

In another method, parameters “a” and “b” can be estimated through the cross correlation of a spectrum with a theoretical template spectrum (Lavila, 2002). An important parameter for the quality of a mass spectrometer is its mass resolution. It defines the spectrometer’s ability to differentiate two ions of slightly different masses. Mass resolution is defined as the ratio of the mass “m” of ions of one specific specie to the deviation in the mass Δm (Cotter, 1997), which is scaled to the mass range under consideration.

$$\frac{m}{\Delta m} = \frac{t}{2\Delta t}$$

Where “m” is the average mass of two ions and “ Δm ” is the difference in masses.

2.2. The dust impact-ionization mechanism

Impact ionization of dust grains is a very specific ionization method used exclusively in space instruments. If a dust particle hits the instrument’s target surface with sufficiently high velocity (> 1km/s) a portion of the impactor and the target surface are vaporized and ionized (Figure 2.2 right). In space environment, the hyper velocity impact ionization process with subsequent TOF-MS plays a vital role in determination of the elemental composition of ice and dust particles. Impact ionization TOF mass spectrometry has been employed in various space missions for compositional analysis.

For the first time the impact ionization process was characterized in 1964 (Friichtenicht, 1964). In later studies, the hyper velocity impact ionization process was used to evaluate the properties of cosmic dust particles ((Auer & Sitte, 1968) & (Friichtenicht et al., 1971)).

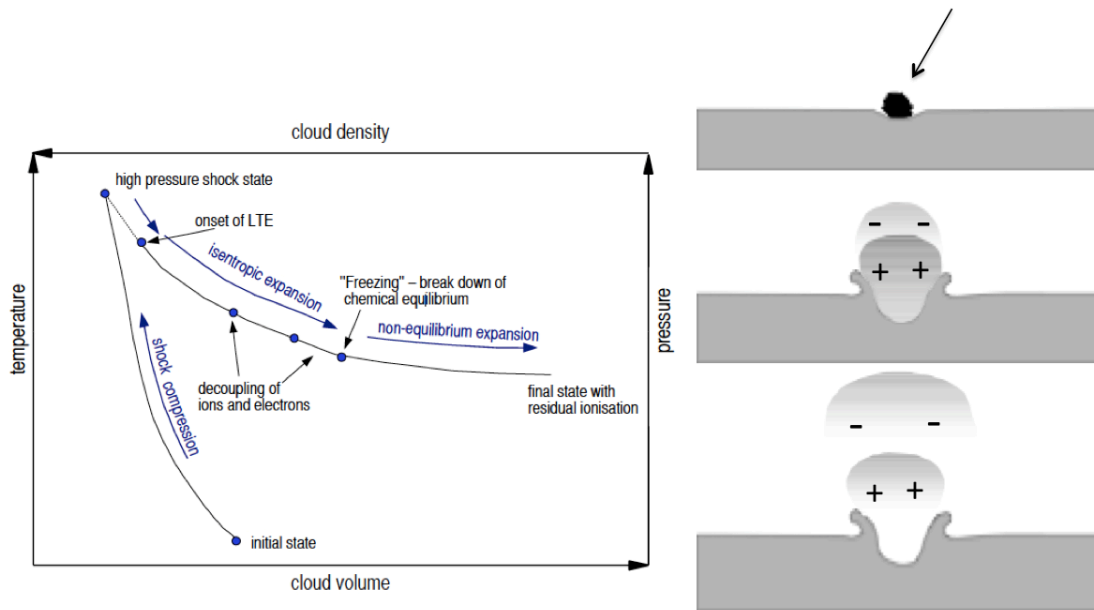


Figure 2.2 (Adapted from (Hornung & Drapatz, 1981) & (Austin, 2003)): (Left) Shown is the principle of shock wave ionization of dust particles. (Right) Shown is the schematic of the impact ionization mechanism: A micron-sized particle hits, melts and creates a crater on the target surface. The clouds of vapors and plasma (electrons and ions) are formed from the particle as well as the target material.

The shock wave dissociates and ionizes molecules and atoms in a dense expanding plasma. Depending on the impact velocity and mass, the dust grain partially or completely evaporates and subsequently ionizes at high temperatures after the release from the high-pressure state, the so-called unloading. Inside the particle, shock waves travel outward and rarefaction waves move inward. This results in an isentropic expansion, which expands the material in all directions and the gas reaches local thermodynamic equilibrium (LTE) (Left Figure 2.2).

At an early stage of the sudden expansion the gas remains in equilibrium. Depending on the density and the temperature, the recombination of species with opposite charges starts at a certain instant of the gas expansion. At this instant the degrees of ionization and dissociation decreases with the time under a power law. Later, the recombination process slows down due to continuous expansion of the gas until it reaches a partially dissociated state with residual ionization, which is known as freezing. Eventually the residual ions are recorded and appeared in a mass spectrum. (After (Mocker, 2011) & (Fiege, 2013) and references therein)

Wiederschein et al., 2015, studied the process of charge separation and isolation during laser dispersion of liquid water matrix as well as in a solid matrix of water ice particle. According to the study, a high-energy impact of ice particle, containing charge carrier, results in separation of charge. On strong impact the fast dispersion of ice particles with embedded charge carriers creates charged fragments (Figure 2.3 left). Most importantly, this phenomenon takes place even if the kinetic energy of the system is lower than that of molecular ionization. Therefore we can observe impact ionization of charged molecules from a water ice matrix already at impact speeds as low as 2 km/s.

The laboratory experiment (IR-MALDI-TOF-MS) (see section 2.3) was used by Wiederschein et al., 2015 to simulate strong impacts of ice particles (Figure 2.3 right). Additionally it was observed that a neutral water beam disperses not only into charged molecules but also into charged macroscopic droplets. The detailed explanation of this experiment is provided in section 2.3.

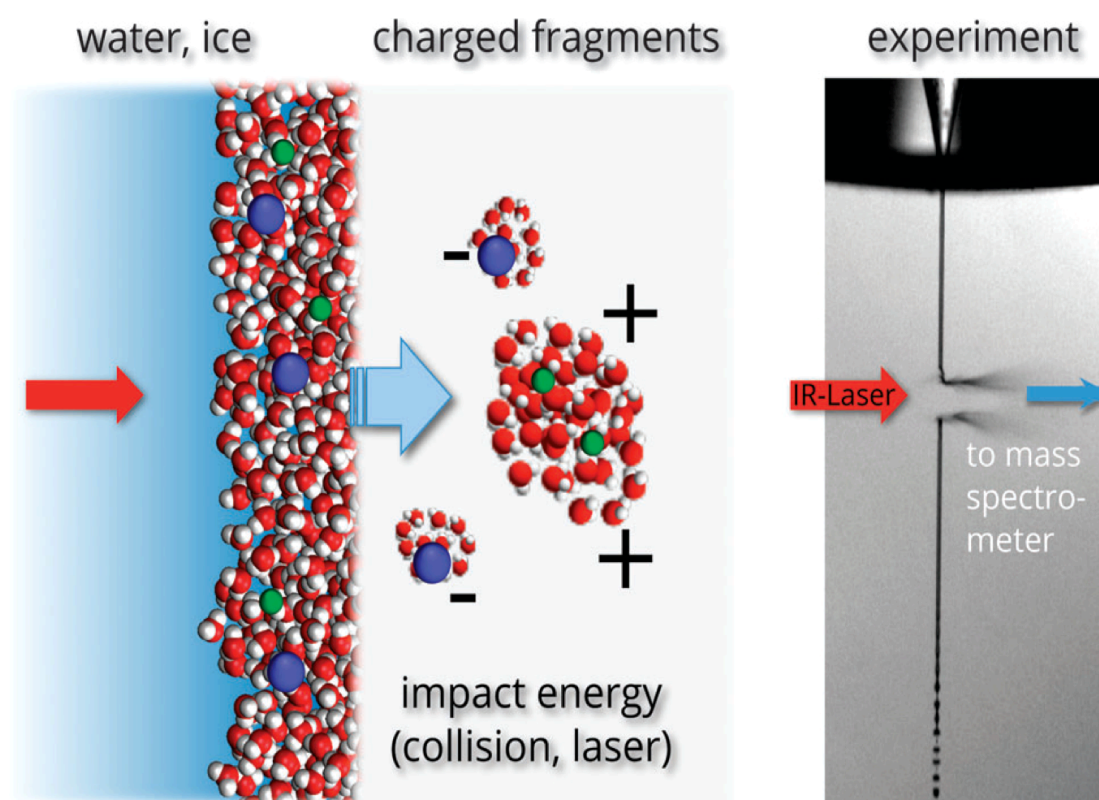


Figure 2.3 (adapted from (Wiederschein et al., 2015)): (Left) Shown is the process of charge separation and charged droplet formation. At high-energy impact of water ice particles or water droplets containing charge carriers (green and blue) disperse fast to produce charged fragments (aggregates & droplets). The excess charge of the system is marked by - or +. (Right) Shown is the analogue experiment for impact ionization of ice particles. The micron-sized water beam containing charge carriers exposed to IR laser of pulse length 7ns at 2.8 μ m. The

beam is irradiated, dispersed and finally produces charged molecules, which are analyzed by TOF mass spectrometer.

2.2.1. The Cassini Cosmic Dust Analyzer—CDA

The Cosmic Dust Analyzer (CDA) (Figure 2.4) was designed and manufactured to characterize the micron- and sub-micron particles at Saturn. The instrument determines speed, mass, electric charge and composition of individual dust particle that enter the CDA. It consists of two independent sub-systems: i) the High Rate Detector (HRD) and ii) the Dust Analyzer (DA).

The High Rate Detector (HRD) is a foil detector capable to monitor high impact rates (up to 10^4 s^{-1}) in dust rich environments at Saturn (Srama et al., 2004). The Dust Analyzer (DA) consists of a suite of three detectors:

- The QP detector: It is a charge-sensing grid that measures the charge carried by the entering dust grain.
- The Impact Ionization Detector (IID): It is similar to the Ulysses- and Galileo-type dust detectors (Grün et al., 1992a & 1992b).
- The Chemical Analyzer (CA): It is a linear TOF mass spectrometer that produces cationic TOF mass spectra from impact ionization.

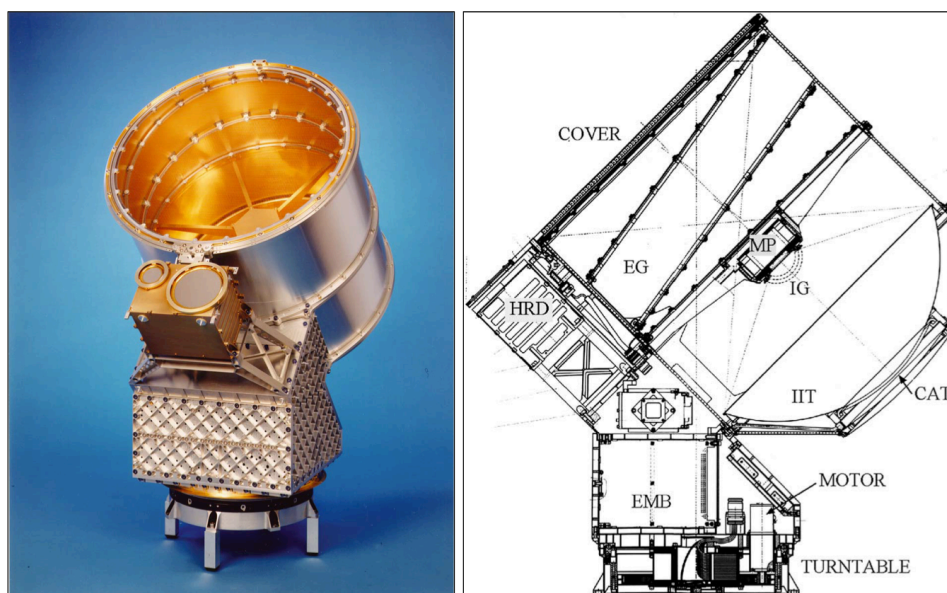


Figure 2.4: (Left) Shown is the photograph of Cosmic Dust Analyzer (CDA). (Right) Side view of a technical drawing of Cosmic Dust Analyzer (CDA) is shown here. The

subsystems of CDA are labeled in the drawing. MP—Multiplier; located in the middle of the instrument. In the left photograph, the backside of the MP is visible. EG—Entrance Grid; in front of the multiplier. IIT—Impact Ionization Target; a large gold plated target. CAT—Chemical Analyzer Target; small Rh target plate in the middle of IIT. IG—Ion Grid; located in front of CAT before MP. HRD—High Rate Detector; located below the dust analyzer. EMB—Electronic Main Box; located below HRD.

2.2.1.1. The CDA Chemical Analyzer subsystem

The CDA data analysis of this thesis almost exclusively uses spectra from the Chemical Analyzer (CA) subsystem. It is described in detail by many previous studies ((Ratcliff & Allahdadi, 1996), (Srama et al., 2004), (Kempf et al., 2005), (Hillier et al., 2006 & 2007a)& (Postberg et al., 2008)). Here, I will give a brief introduction of the functional principle of the CA.

The CA (Figure 2.5) subsystem provides compositional information of an impinging dust particle onto its target plate and works on the principle similar to a simple TOF mass spectrometer after impact ionization (see section 2.1). The dust particle enters into CDA and hits either the central rhodium target plate (Chemical Analyzer Target—CAT), or the surrounding gold plate (Impact Ionization Target—IIT), or the inner walls of the instrument. Mass spectra are only produced when a dust particle hit onto the CAT. It has an effective field of view of 28° (Hillier et al., 2006 & 2007a). The impinging dust particle with hyper velocity on the CAT is completely vaporized and partially ionized. The plasma produced by the impact consists of the ions from the particle material and as well as the target material together with electrons and neutral species. The CA mass spectrometer is sensitive to positive ions only, a strong electric field extracts the cations from the plasma cloud and accelerates them towards the multiplier.

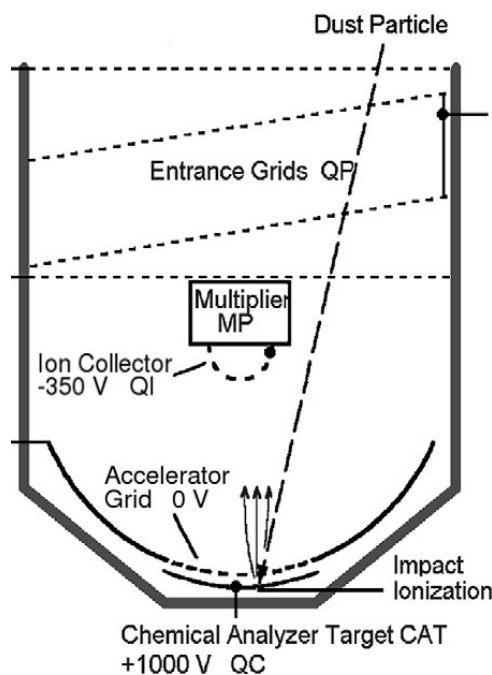


Figure 2.5 (Adapted from (Postberg et al., 2008)): A time-of-flight mass spectrum is generated by the particle impact on the Chemical Analyzer Target (CAT). The CAT is made of rhodium metal, which is held at $\sim +1000$ V with respect to an electrically grounded grid situated ~ 0.003 m in front of it. The QC channel of the CAT records the integrated charge signal from electrons and negative ions, and the positive ions are accelerated towards the grounded grid. The cations pass through the grounded grid and drift through a weak electric field ~ 1.8 kVm^{-1} towards the logarithmic amplifying detector, referred as multiplier (MP). The cations are separated by their time-of-flight to reach the multiplier, which depends on mass-to-charge ratio (m/q). Almost 50% of the accelerated ions are collected at the QI grid in front of the multiplier, where the integrated charge of positive ions is registered. After passing through the QI grid, cations enter a strong field region ~ 100 kVm^{-1} where the cations are accelerated finally into the MP showing the output, volts at the final dynode, as a function of time to produce TOF mass spectrum.

The spectrum recording can be triggered either when the collected negative charge exceeds the threshold on the CAT* or when the first abundant cation species (e.g., $[\text{H}]^+$, $[\text{H}_3\text{O}]^+$, $[\text{Na}]^+$) arrive at the MP after impact**. In many cases, a spectrum recording of the water-dominated ice particles is triggered by hydronium ions $[\text{H}_3\text{O}^+]$ arriving at the MP. As a result the mass line corresponds to $[\text{H}_3\text{O}^+]$ and ions with lower mass-to-charge ratio do not appear in the mass spectrum.

* Upon impact, the instrument collects negative charge and converts into current up to a certain threshold to trigger the spectrum recording. ** After impact positive ions accelerate towards the MP, where charge is amplified into a current that, above a threshold, triggers the spectrum recording.

The quasi-logarithmically amplified spectra are recorded for a period of 6.4 microseconds after triggering — over the mass up to ~ 190 atomic mass units (u), assuming that the incident was triggered by impact and ions are singly charged. If the spectrum was triggered by a mass line, the mass range is shifted to higher masses (e.g. ≈ 230 u for a trigger by H_3O^+).

Since

$$\text{TOF} = s/v \sim \sqrt{m/q}$$

the TOF mass spectrum can be calibrated over a mass scale as

$$\text{TOF} = a\sqrt{m} + b.$$

Here “a” corresponds to stretch parameter that is related to field strength of the instrument and “b” refers to a zero offset (“delay” or “shift” parameter) that is related to the trigger time of the instrument (see section 2.1). The changes in the distance and voltage between the CAT and the acceleration grid can alter the stretch parameter, which is normally set on a constant value by the physical set up of the instrument. On the other hand, the shift parameter may vary between spectra due to the production process of ions, different triggering times or other electronic effects.

The initial velocities of ions in the impact cloud are broadly distributed that in turn affects the TOF due to the expansion of plasma cloud (Mocker, 2011). In addition, the TOF is influenced by the variations in ions’ flight paths and also by the plasma shielding effects (Hillier et al., 2006).

The CA is sensitive only for positive ions. The resolution of the MS varies between 10—50, depending on the atomic masses of ions (1—190 u). Generally this resolution is in most cases not sufficient for the detailed analysis of complex chemical structures, and only allows classifying different compositional types of the impact projectiles such as water ice-, organic- and mineral-particles.

However, using analogue materials to mimic CDA spectra in the laboratory can drastically improve the chemical spectra analysis. Suitable setups for analogue experiments are either a dust accelerator (Mocker, 2011) for mineral, metal and

organic grains, or a laser experiment for icy grains, as described in the following section.

2.3. Analogue spectra by water dispersion and infrared MALDI time-of-flight mass spectrometry (IR-MALDI-TOF-MS)

Laser ionization (IR-MALDI-TOFMS) (Figure 2.6) ((Gebhardt et al., 1999) & (Charvat & Abel, 2007)) is used to simulate the impact ionization process of icy dust particles onto space borne instruments. In the experimental setup, aqueous solutions of organic and inorganic compounds are vertically injected into a vacuum chamber at a pressure $p \approx 5 \cdot 10^{-5}$ mbar. The injected sample is then passed through a quartz nozzle with high pressure (10-20 bar) forming a liquid micro-beam of 12 - 16 μm in diameter at a flow speed of 20 - 40 m/s. The liquid beam is excited by a pulsed nanoseconds infrared laser adjusted to $\lambda = 2850$ nm, which is the OH-stretch absorption of bulk water.

The adjustable Infrared (IR) laser can be used to simulate different impact energies of an ice grain onto the CDA target plate. The liquid beam is exposed to the IR laser at a distance of 1 cm from the opening of the accelerator of the mass spectrometer. The shock wave propagates through the exposed liquid beam and creates individual ions and water clusters of different masses, a part of which enters the TOF mass spectrometer. The single positively charged ions are accelerated into the drift-tube of the MS using the pulsed ion optics (4-6 kV) and uncertainties in kinetic energy are compensated by the built-in reflectron. The single positively charged ions are accelerated into the drift-tube of the MS using the pulsed ion optics (4-6 kV) and uncertainties in kinetic energy are compensated by the built-in reflectron.

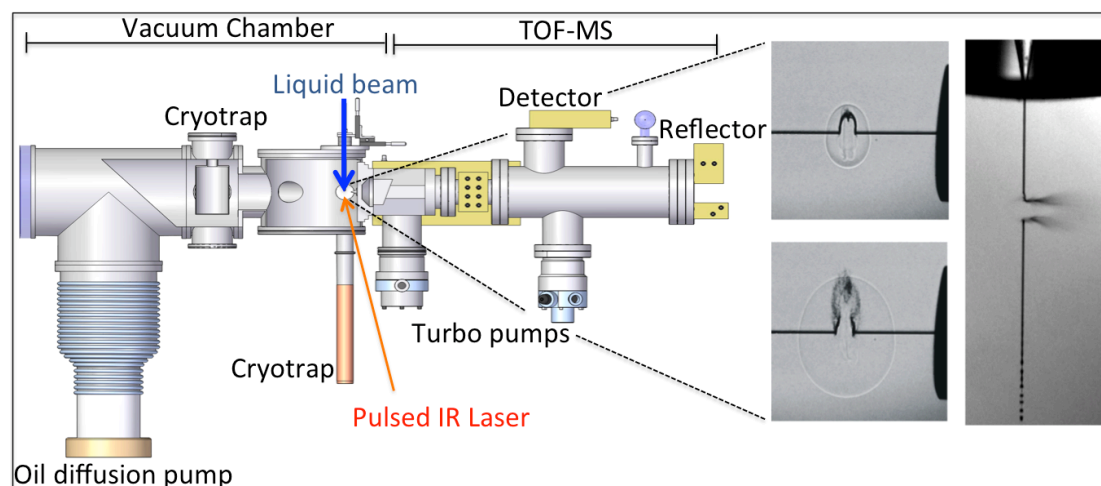


Figure 2.6 (Adapted and modified from (Beinsen, 2011)): *The experimental setup (IR-MALDI-MS) used to simulate CDA organic rich ice spectra from space at*

different impact velocities. The dispersion scheme of 12-16 micrometer liquid water beam with an IR laser is also shown as an enlarged image (right).

The adjustable energy density on the liquid beam in combination with delay time settings for ion extraction simulates variety of impact energies of ice grains on the CDA target. The ions are then accelerated to the extracted region of the MS. The time required to reach the extraction (delay time: T_D) region is different for different m/z values of ions. The extraction ion optics of the laboratory setup transmits ions of specific m/z values into the mass spectrometer, hence acts as an ion gate. (Charvat et al., 2004)

2.3.1. Comparison of molecular fragment clusters between IR-MALDI-MS and CDA

Laser ionization process in the laboratory is a new technique to simulate the impact ionization process of ice particles in space ((Postberg et al., 2009a) & (Wiederschein et al., 2015)). The analyte is exposed to similar energy densities in both processes to form similar cationic fragment clusters (Figure 2.7 A & B), which can be analyzed by TOF mass spectrometry.

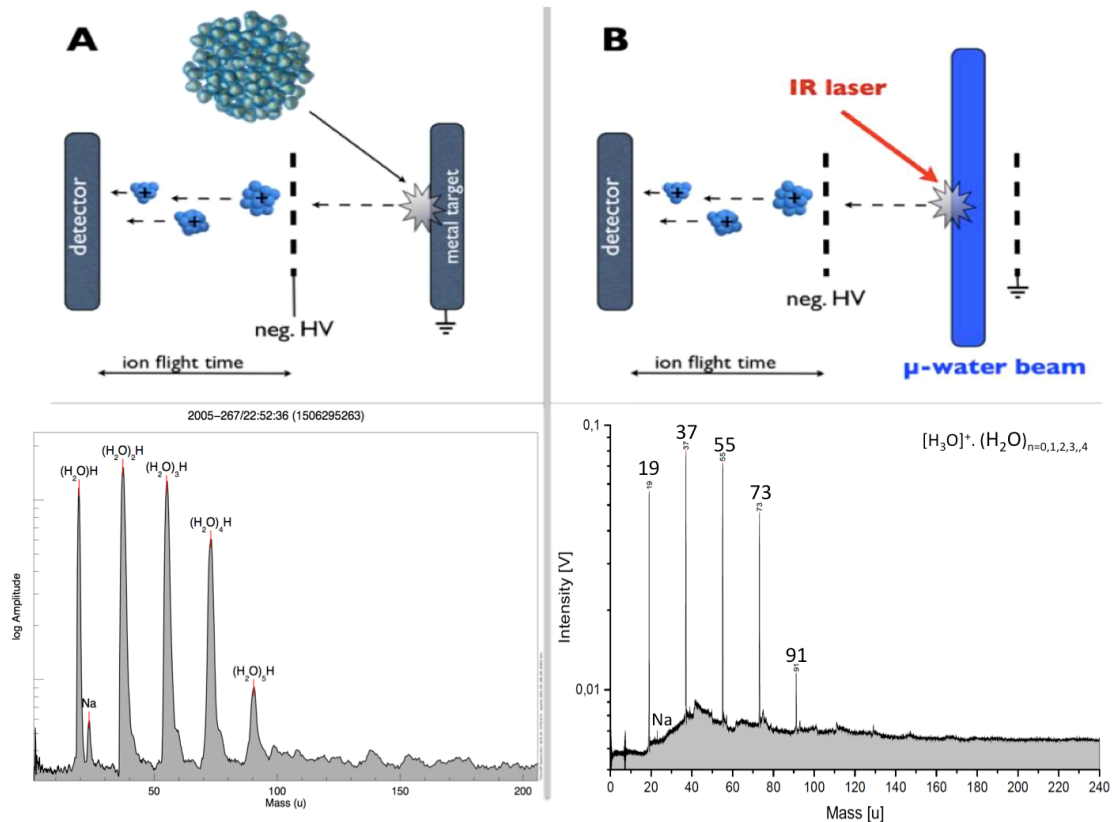


Figure 2.7 (Adapted from (Postberg et al., 2009a) supplement & references therein): Schematic of the impact and laser ionization processes. (A) High velocity

impact of a micron sized ice grain on CDA target. (B) Laser dispersion of a liquid water filament in the laboratory. Similar cationic fragment water clusters are shown from both processes. The example spectra show that the laser assisted analogue experiment reproduced the CDA mass spectra with high accuracy.

2.4. Basic principles of water dominated mass spectra

The majority of the CDA impact spectra at Saturn are due to E ring water ice particles impinging onto the CAT. Understanding patterns of water features in the impact spectra is important for the identification of non-water species embedded in the ice particles.

The water-cluster peaks dominate in most of the CDA water ice mass spectra. Depending on impact speed the size of water-clusters $[\text{H}_3\text{O}]^+(\text{H}_2\text{O})_n$ varies between $n = 0$ to $n = 15$ and the relative amplitudes of cluster-peaks vary as well, where the highest amplitudes remains between $n = 1$ to $n = 4$.

The neutral water molecules form clusters with a hydronium ion as an ion core. In addition, the water molecules also form clusters with other ion species e.g. rhodium- $[\text{Rh}]^+$ and sodium- $[\text{Na}]^+$. Three different water cluster patterns are discussed here in the CDA water-rich mass spectra.

- $[\text{H}_3\text{O}]^+$ —neutral water clusters
- $[\text{Na}]^+$ —neutral water clusters
- $[\text{Rh}]^+$ —neutral water clusters

Amongst others Shi et al., 1993 and Wang et al., 2003 investigated in detail the clustering of water molecules after ionization in the gas phase. Moreover, the process of water clustering inside the impact plasma was investigated by Timmermann (1989) and Timmermann & Grün (1991). Here I give a brief introduction of the clustering mechanism.

The impact of a water ice particle onto the instrument's target (Figure 2.5) leads to the generation of charged elemental and molecular fragments (e.g. $(\text{H}_2\text{O})_n\text{-H}_3\text{O}^+$) (see section 2.2), not only from the particle itself but also from the target material (Rh^+). The CA, collects negatively charged species at the CAT, which

cannot be measured in the form of mass spectrum (see section 2.2.1.1). In addition, the impact also results in abundant formation of neutrals (e.g. $(\text{H}_2\text{O})_n$). The presence of target-projectile ions of the form $(\text{H}_2\text{O})_n\text{Rh}^+$ shows that these neutrals might subsequently attach to ions present in the impact cloud (Figure 2.9).

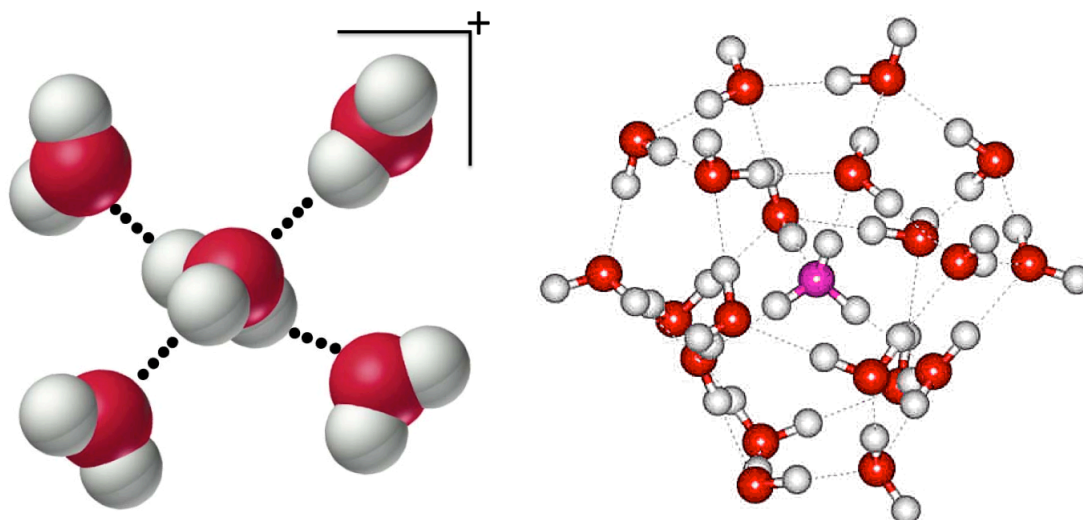


Figure 2.8: Shown is the clustering of neutral water molecules with hydronium ion $[\text{H}_3\text{O}]^+$. Three hydrogen atoms of the ion core form bonds with the oxygen atoms of the neighboring neutral water molecules. The electron rich part of the ion core (oxygen) forms a bond with the hydrogen of another neutral water molecule. This process could produce large cluster ions. ((Postberg et al., 2008) & <http://www1.lsbu.ac.uk/water/magic.html>)

The stability of clusters depends on the energy content of the system i.e. clusters are stable when the kinetic energy (temperature) of molecules is lower than the cluster energy. The distribution of different sizes of cluster ions thus also depends on temperature of the plasma cloud (Figure 2.9) and thus on impact speed. If the temperature is high, large cluster fragment to smaller and more stable ones.

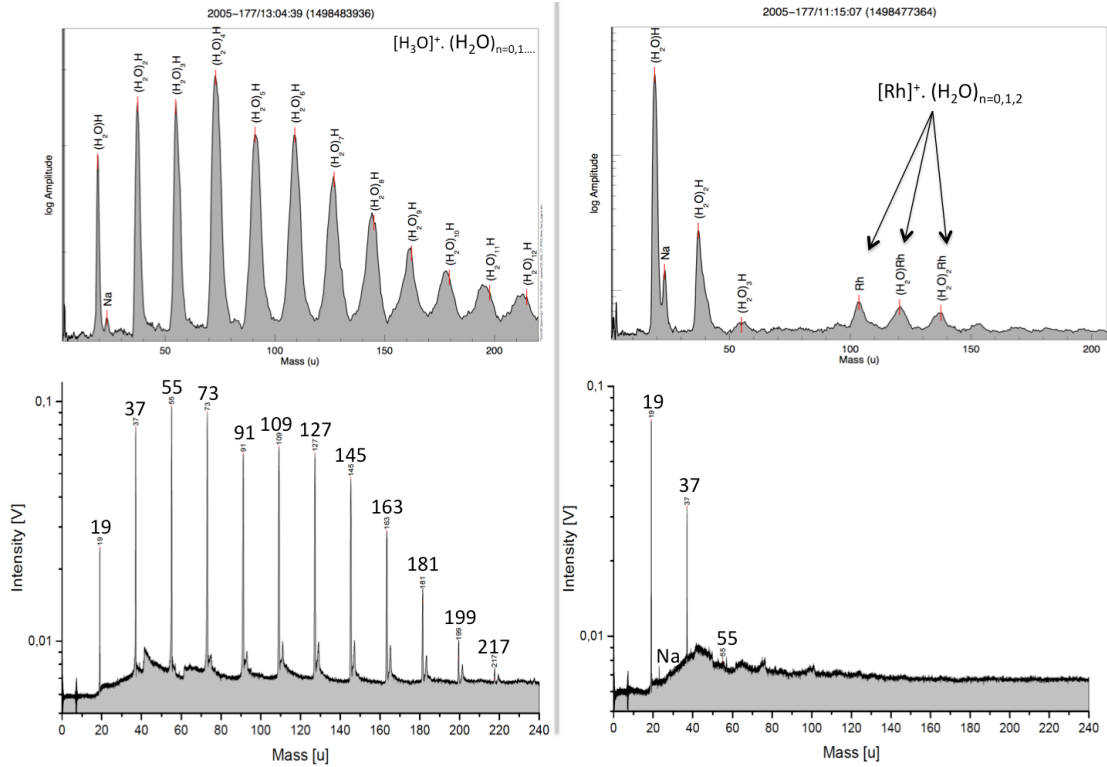


Figure 2.9: Shown are CDA spectra from E-ring water ice impacts (Top) and their respective analogue laboratory (IR-MALDI) mass spectra (Bottom). The hydronium $[H_3O]^+$ mass line at 19 u is followed by a sequence of peaks with the periodic spacing of 18 u of the form $[H_3O]^+(H_2O)_n$. The appearance of water clusters changes with the impact conditions. For example, the low impact speed and energy density leads to lower temperatures and thus large water clusters, whereas at high energy densities small water clusters are preferred. (Left) Shown are the large water cluster species up-to $n = 11$. (Right) Water clusters peaks decrease exponentially at relatively higher impact speed and energy density. Neutral water molecules also form clusters with other ion species. At 103 u, the water ice CDA spectrum shows a peak corresponding to the CDA impact target material Rhodium (Rh), which forms target-projectile clusters of the form $[Rh]^+(H_2O)_n$. Rhodium-clusters only appear at impact speeds that are sufficiently high (above about 9 km/s) to form cations from the target material.

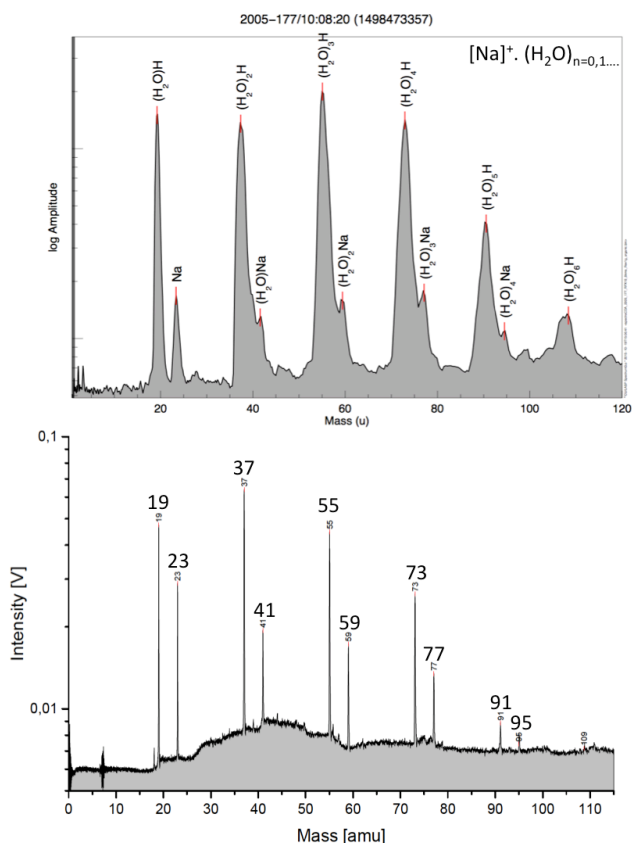


Figure 2.10: Shown are the peaks due to water-water and Na-water clusters in a CDA water ice spectrum (Top) and in the related laboratory spectrum (Bottom). Similar to $[\text{H}_3\text{O}]^+$ and $[\text{Rh}]^+$, water forms clusters with $[\text{Na}]^+$, which are often observed in CDA spectra. The $[\text{Na}]^+(\text{H}_2\text{O})_{n=1,2,3,\dots}$ clusters appear, in general, on the right flank of hydronium-water clusters. Depending on the abundance of sodium ions, the amplitudes and the sizes of Na-water clusters can alter.

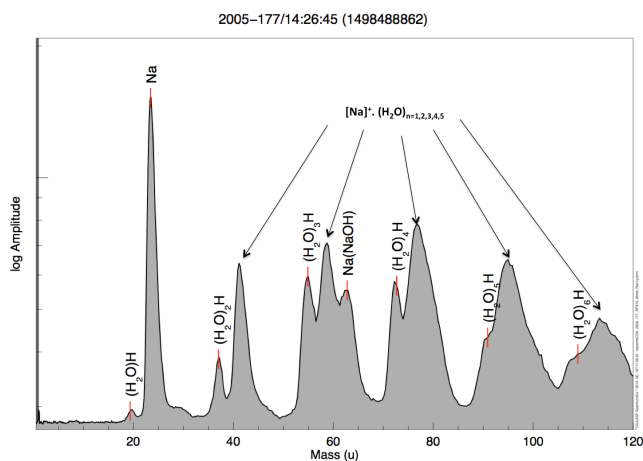


Figure 2.11: Shown is the CDA water ice spectrum with a high $[\text{Na}]^+$ peak. In addition to Na-water clusters, a peak at 63 u represents $[\text{Na}]^+(\text{NaOH})$, which indicates a much higher Na concentration in the case shown in Figure 2.10 (see section 2.4.1). The sodium peak and the related clusters dominate the whole spectrum. For different impact conditions the peak maxima of Na-water and Na-hydroxide clusters, $[\text{Na}]^+(\text{H}_2\text{O})_n$ and $[\text{Na}]^+(\text{NaOH})_n$ varies from $n = 1$ to 10.

2.4.1. Compositional types of ice grains in the E ring and the Enceladian plume

The CA subsystem of CDA has produced thousands of cationic TOF mass spectra of ice particles impinging onto the instrument's metal target. Postberg et al., 2008 & 2009a have identified three compositionally distinct families of the ice grains. In this section, I will give a brief introduction of these spectrum types.

Table 2.1: Three families (types) of ice grains and their characteristic features (Postberg et al., 2008 & 2009a).

Ice particles	Type-1 (Na-poor)	Type-2 (Na-poor)	Type-3 (Na-rich)
Composition	Almost pure water ice with Na and/or K traces	Water ice with Na and/or K traces and organic compounds	Water ice with abundant Na and K salts

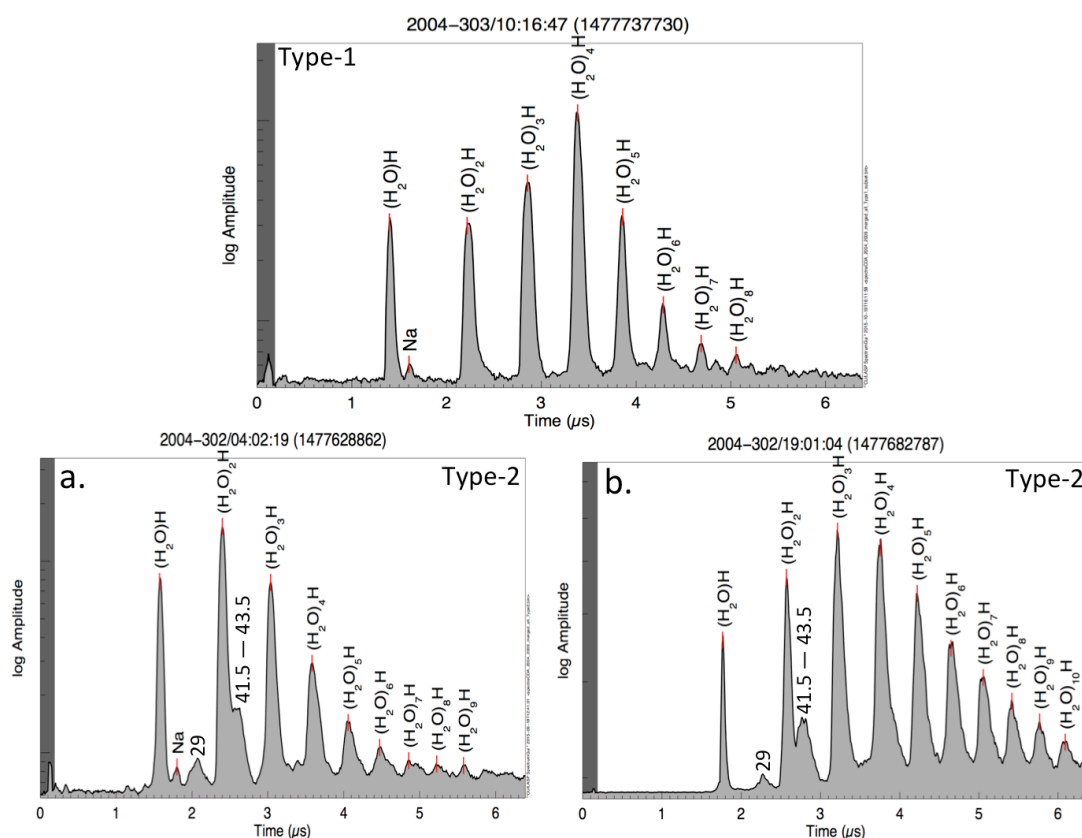


Figure 2.12: Shown is the comparison between Type-1 and Type-2 spectra. The Type-1 spectrum (Top) shows only traces of Na^+ (23 u) as the only non-water feature and the respective water cluster $[\text{Na}]^+(\text{H}_2\text{O})_n$. (Bottom): Type-2 (a) shows small $[\text{Na}^+]$, whereas Type-2 (b) shows no $[\text{Na}^+]$. The defining peak of Type-2 spectrum at a TOF corresponding to 29 u is visible in both examples (a & b). The broad defining feature contains multiple-components between 26–31 u. In addition, Type-2 spectra regularly also show a characteristic broad feature at a

TOF equivalent to the mass range between 41—44 u. The 29-feature and the broad feature between 41.5—43.5 (u) in Type-2 spectra can represent organic cationic species of the form $[C_xH_y]^+$, $[C_xH_yO]^+$ and $[C_xH_yN]^+$ ((Goldsworthy et al., 2003), (Srama et al., 2009) & (Postberg et al., 2008)).

The characteristic difference between the pure water ice spectra (Type-1) and the organic enriched spectra (Type-2) is the mass line (s) at 26—29 (u) (Figure 2.12). Both spectral types show a low or no mass line at 23 u $[Na]^+$. In addition, some spectra occasionally show ions from the Rh-target material preferably at high impact speeds.

Type-3 spectra (Figure 2.13) exhibit a totally different mass lines pattern, which is attributed to ice particles containing about 1% sodium salts. These spectra show no or strongly suppressed water cluster but cationic molecular fragments corresponding to NaCl, NaHCO₃ and/or Na₂CO₃.

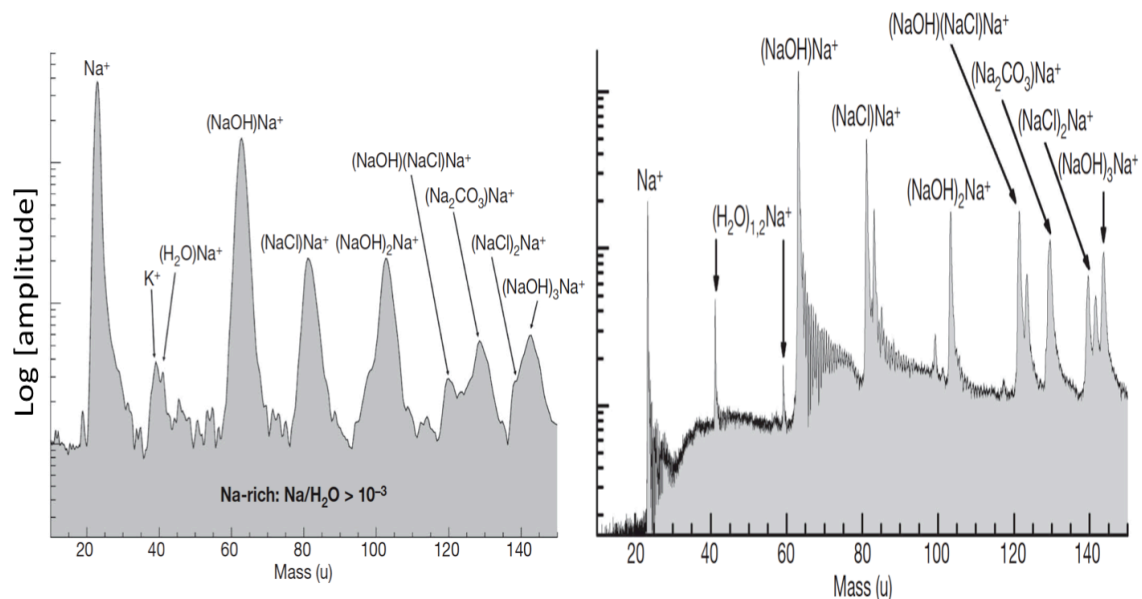


Figure 2.13 (Adapted from (Postberg et al., 2009a)): (Left) Co-added CDA spectra of sodium rich water ice particles (Type-3). The water cluster $[H_3O]^+(H_2O)_n$, $[Na]^+(H_2O)_n$ are suppressed. Instead, Type-3 spectra are characterized by mass lines at 23 and 63 (u) corresponding to $[Na]^+$ and $[Na]^+(NaOH)$, respectively, followed by a sequence of higher order hydroxyl cluster ions. Often these spectra show also $[Na]^+(NaCl)_{n=1,2,3}$ and $[Na]^+(Na_2CO_3)$. (Right) Shown is the Type-3 spectrum reproduced in the laboratory by laser dispersion of salt water. The correlation between laboratory and CDA spectra allows estimating the abundances of NaCl, NaHCO₃ and KCl in the Type-3 E-ring ice grains to 0.5 – 2%.

2.5. Method to determine the compositional profiles of ice grains at Saturn

A statistical method, called Boxcar Analysis (BCA), is used to determine the compositional profiles of the E-ring ice particles during Cassini's flybys.

Following are the systematic steps of this method:

- Step-1: Calibration of the mass spectra and the assignment of the compositional type to each spectrum. For example Type-1, Type-2 & Type-3 (for more detail about these types see section 2.4.1).
- Step-2: Preparation of a database of each spectrum type of the ice particles recorded at a unique instant of time (e.g., a second).
- Step 3: The BCA provides the number of spectra of each type over a selected time interval, the so-called box size. A suitable step size is selected to repeat the integration of counts in the defined box size for the whole time duration.

For example;

Box size = 10 seconds

Step size = 5 seconds

The box size is larger than the step size, thus the boxes for the different steps overlap:

Time bins (sec) = $T_{b(sec)} = [1.....10], [5.....15], [10.....20]....., [T_{(N-10)}.....T_N]$

The counts of each spectrum type are summed up in each interval (time bin).

For example;

Absolute abundance of Type-1 in one time bin = $\sum \text{Type-1}$

- Step 4: The number of each compositional type of particles in absolute abundances is then converted into the respective proportions for each interval.

$$\text{Relative proportions of each type} = [\Sigma\text{Type-1}/(\Sigma\text{Type-1}+\Sigma\text{Type-2}+\Sigma\text{Type-3})] * 100$$

- Finally the graphical output is generated, which shows the proportions of each compositional type during each time bin along the spacecraft trajectory (For more detail see chapter 4 of this thesis) (Figure 4.5).

3. Organic Material in E ring Ice Grains

3.1. Introduction

Enceladus is emanating sub-surface material in the form of gas plume and ice particles from fractures near its south pole ((Porco et al., 2006), (Schmidt et al., 2008), (Postberg et al., 2009a & 2011a) & (Hsu et al., 2015)) and feeding the Saturn's E-ring ((Spahn et al., 2006) & (Kempf et al., 2008)). On one hand the Cassini's Ion and Neutral Mass Spectrometer (INMS) has already identified a multitude of volatile organic species in the plume's gas phase (Waite et al., 2009). On the other hand the Cassini's CDA is sensitive to measure condensed organic material in the ice grains and the major aim of this thesis is to investigate the nature of organic material embedded in the E-ring ice grains.

During the E-ring crossings and the flybys of Enceladus, three major types of mass spectra of the ice grains have previously been identified in the E-ring and in the plume of Enceladus. The spectrum types represent the compositional types of E-ring ice grains, which are briefly summarized here ((Hillier et al. 2007b), (Postberg et al., 2008 & 2009a)). For detail of these types see section 2.4.1.

- 1) Almost pure water ice — Type-1
- 2) Organic enriched — Type-2
- 3) Salt rich — Type-3

3.1.1. CDA mass spectra of organic enriched E ring ice grains

The spectra of pure water (Type-1) and salt rich (Type-3) ice grains have already been well investigated (Postberg et al., 2008 & 2009a), whereas Type-2 spectra (Figure 3.1) still need to be characterized in detail. The only previous investigation of CDA spectra of organic enriched ice grains (Type-2) showed a

characteristic signature at about 29u covering a mass range between 26 and 31 (u), which represents multiple organic species (Postberg et al., 2008). In addition other organic species $[C_3H_x]^+$ were also observed. The more in-depth study of Type-2 spectra carried out in this work can help us to investigate refractory organic compounds from Enceladus' subsurface ocean.

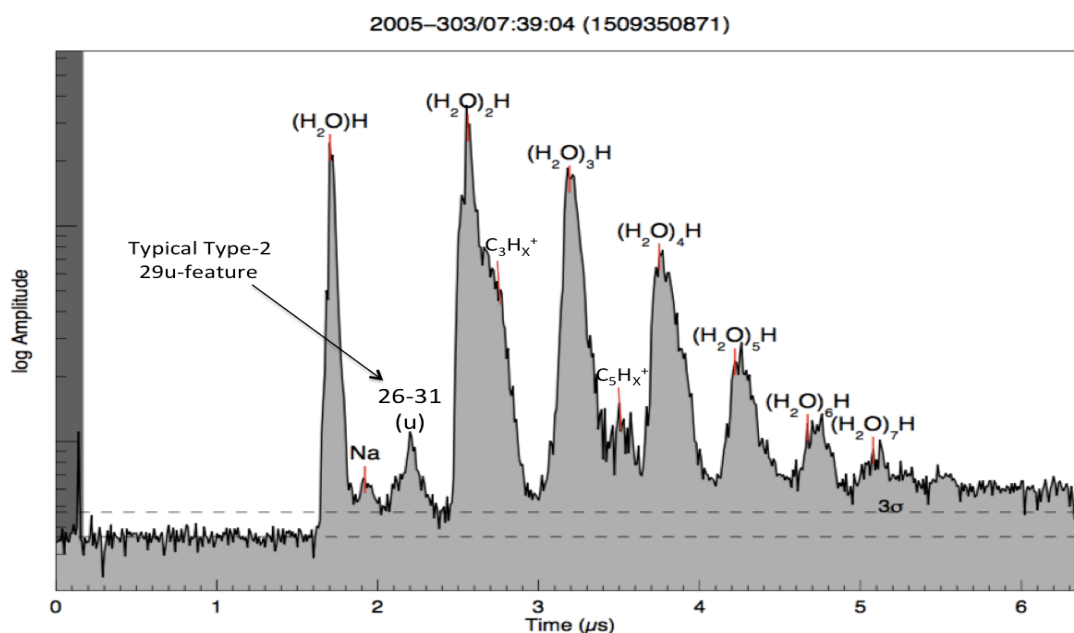


Figure 3.1: Shown is the typical example of a Type-2 spectrum with its defining peak typically covering at a mass range of 26-31(u). In most of the Type-2 spectra other typical organic features are also observed at m/z 42-45(u), possibly, as $C_3H_x^+$. In some of these spectra peak at m/z 63-65(u) is also observed (Postberg et al., 2008).

In contrast to Type-1 and Type-3 spectra, which in most of the cases show a very characteristic peak pattern, Type-2 display a great diversity indicating varying contribution of different organic species. The figure below (Figure 3.2) shows diverse organic features (marked in red) in three different Type-2 spectra, in addition to water clusters. Although these spectra exhibit similar characteristic Type-2 features, there exists significant variation in their peak patterns because of the presence of different organic species. With the help of analogue laboratory experiments, I have categorized Type-2 spectra based on these peak patterns and attributed them to certain classes of organic compounds.

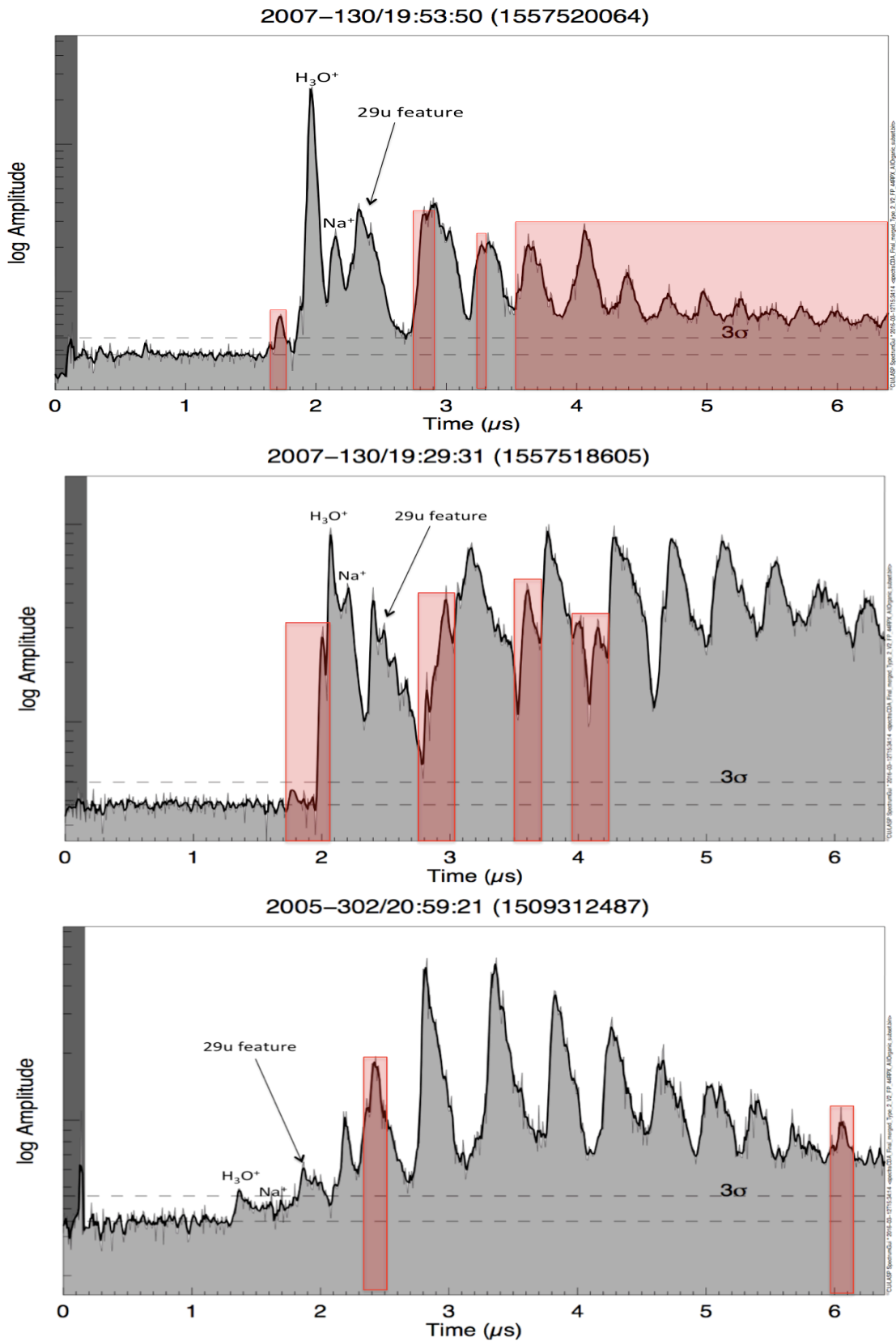


Figure 3.2: Shown is the diversity of peaks pattern in three different CDA Type-2 spectra of the space born ice particles. The prominent organic features in each spectrum are shown in red. The diversity in peak patterns of organic features suggests the presence of a variety of organic species in the ice grains. The organic

signatures are discussed in detail in next section 3.2. The peaks not marked in red are mostly due to water-cluster cations (see section 2.4.1).

3.2. Results

The aim of this section is to analyze CDA salt poor Type-2 spectra and to identify and assign unique organic signatures other than the characteristic 29u-feature. The relatively low mass resolution of CDA spectra makes it difficult to correctly identify different organic compounds. However, based on the peak patterns of fragment cations families of organic compounds are identified in this work that can be verified with the laser assisted analogue experiment (for detail about the experiment see section 2.3).

Table 3.1: Pattern of common cationic fragments of different types of organic compounds ((Korth et al., 1990) & (McLafferty & Turecek, 1993)).

m/z	Formula	Cationic fragments	Compound type
15, 29, 43,	$C_nH_{2n+1}^+$	CH_3^+ , $C_2H_5^+$, $C_3H_7^+$,	Saturated alkyl
13, 27, 41,	$C_nH_{2n-1}^+$	CH^+ , $C_2H_3^+$, $C_3H_5^+$,	Un-saturated alkyl
31, 45, 59,	$C_nH_{2n+1}O^+$	CH_3O^+ , $C_2H_5O^+$, $C_3H_7O^+$,	Aliphatic alcohols, ethers
45, 59, 73,	$C_nH_{2n-1}O_2^+$	CHO_2^+ , $C_2H_3O_2^+$, $C_3H_5O_2^+$,	Acids, esters
33, 47, 61,	$C_nH_{2n+3}O^+$	CH_5O^+ , $C_2H_7O^+$, $C_3H_9O^+$,	Alcohols, polyols
33, 47, 61,	$C_nH_{2n+1}S^+$	CH_3S^+ , $C_2H_5S^+$, $C_3H_7S^+$,	Thiols, sulfides
39, 53, 67,	$C_nH_{2n-3}^+$	$C_3H_3^+$, $C_4H_5^+$, $C_5H_7^+$,	Dienes, alkenes
38-39, 50-52, 63-65, 75-78, 89-91	$C_nH_{5n}^+$	$C_3H_3^+$, $C_4H_3^+$, $C_5H_5^+$, $C_6H_5^+$, $C_7H_7^+$	Aromatic series
18, 30, 44,	$C_nH_{2n+2}N^+$	NH_4^+ , $CH_2NH_2^+$, $C_2H_5NH_2^+$,	Amines
29, 43, 57,	$C_nH_{2n-1}O^+$	CHO^+ , CH_3CO^+ , $CH_3CH_2CO^+$,	Aldehydes, ketones

Distinct cationic fragmentation patterns were identified in certain groups of exemplary ‘archetype spectra’, suggesting the presence of at least three families of organic compounds in certain ice grains; i) Amines, ii) Carbonyl and iii) Aromatics.

In this study ~ 729 Type-2 spectra were analyzed. Out of these, 320 Type-2 spectra with apparent characteristic signatures were compared with different

signatures from organic compounds with the help of the analogue experiment. From the compared spectra, 197 'archetype spectra' allowed the specification of certain organic families (amines, carbonyls and aromatics). Among these 197 spectra, about 18% exhibit combined features of the detected organic families. The other 123 spectra showed weak or ambiguous signatures of these organic families.

In the following sections, CDA and the laboratory spectra of each family of organic compounds are explained in three steps. In the first step, the calibration of a spectrum is discussed by assigning the known reference mass lines at m/z 19, 23, 37 & 41 that correspond to $[\text{H}_3\text{O}]^+$, $[\text{Na}]^+$, $[\text{H}_3\text{O}]^+(\text{H}_2\text{O})$ & $[\text{Na}]^+(\text{H}_2\text{O})$, respectively. In the second step water cluster species are highlighted and in the final step characteristic features of each organic family are discussed.

3.2.1. Identification of amine species in E ring ice grains

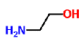
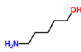
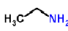

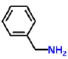
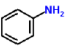
With the help of ToF spectra from the analogue experiment, typical cationic fragment of amines are identified. In addition, cluster pattern of amines species are also discussed and identified.

3.2.1.1. Laboratory measurements

In order to study the fragmentation pattern of amines, specifically the characteristic cationic fragments, spectra of different amines in a water matrix were measured.

Three different kinds of amines were selected and tested: alkanolamines, primary alkyl amine and aromatic amines (Table 3.2). To investigate the dependence of fragmentation on chain length in each group, two compounds with varying number of carbon atoms were selected.

Table 3.2: List of measured amines in the analogue experiment. Molecular weights and the most apparent ions in the spectra are listed.

Molecule	Formula	Structural formula	Mol. weight	Mol. peak	Ammonium cation	Other significant peaks
<i>Alkanolamines</i>						
Ethanolamine	C ₂ H ₇ NO		61	[M+1] ⁺	18	[C ₂ H ₄ NH ₂] ⁺ [CH ₂ NH ₂] ⁺
5-Amino-1-pentanol	C ₅ H ₁₃ NO		103	[M+1] ⁺	18	[M-OH-NH ₂ +H] ⁺ , [M-OH] ⁺ [CH ₂ NH ₂] ⁺ , [C ₂ H ₄ NH ₂] ⁺
<i>Primary alkyl amines</i>						
Ethylamine	C ₂ H ₇ N		45	[M+1] ⁺	18	[CH ₂ NH ₂] ⁺
Butylamine	C ₄ H ₁₁ N		73	[M+1] ⁺	18, 17	[M-NH ₂] ⁺ [CH ₂ NH ₂] ⁺ , [C ₂ H ₄ NH ₂] ⁺
<i>Aromatic amines</i>						
Benzylamine	C ₇ H ₉ N		107	[M-1] ⁺	18	aromatic fragments [CH ₂ NH ₂] ⁺
Aniline	C ₆ H ₇ N		93	[M+1] ⁺	18	aromatic fragments

The analysis of all amines shows a distinct hydrogenated or dehydrogenated molecular ion. For example the above figure (Figure 3.3) exhibits the hydrogenated molecular cation of butyl amine at m/z 74 as [C₄H₉-NH₂+H]⁺. The loss of NH₂ is also observed at m/z 57 as [C₄H₉]⁺. Very frequently observed with all amines is a mass line at m/z 30. This corresponds to a characteristic fragment [CH₂NH₂]⁺ where the amine group (NH₂) is directly attached to an alkyl group – CH₂ (Table 3.2).

All amines (Table 3.2) show a very intense fragment at m/z 18, which corresponds to the ammonium cation [NH₄]⁺. The Ammonium cation is produced due to cleave of the bond next to NH₂ in amine species. In addition, some amines also showed a minor peak at m/z 17 as [NH₃]⁺ (Table 3.2). In case of butyl amine (Figure 3.3) 18u is a base peak, which also forms clusters with neutral water molecules at m/z 36 and 54.

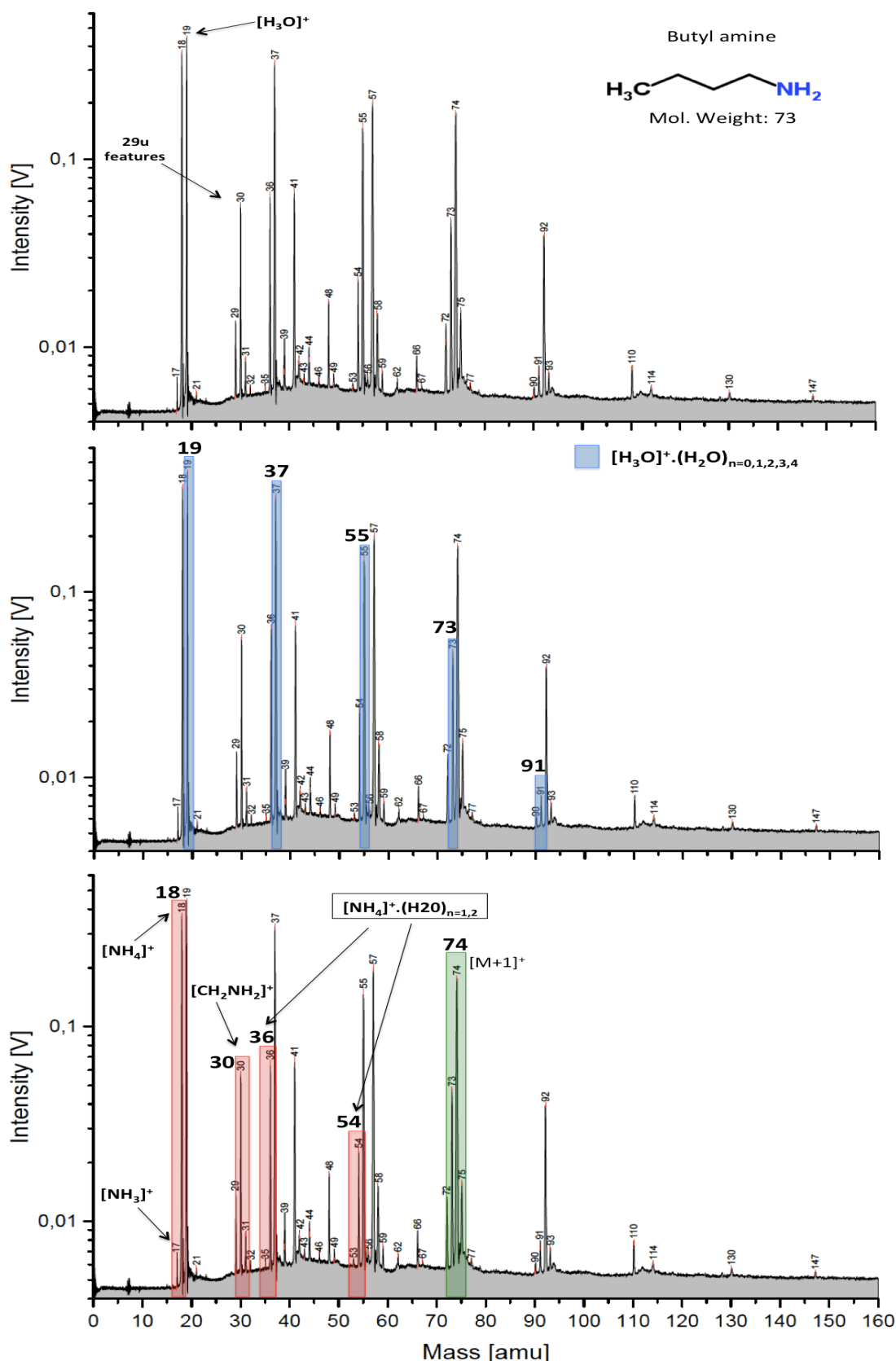


Figure 3.3: Three identical ToF laboratory spectra of butyl-amine at the concentration of 0.05 mol/kg in H₂O. For clarity the same spectrum is explained in three steps. In the top spectrum, the hydronium peak and the 29u-feature (as observed in CDA Type-2 spectra) is labeled. Water-clusters are shown in blue in the middle spectrum. In the bottom spectrum, typical fragments of amines and their

water-clusters are labeled and highlighted in red. The hydrogenated molecular peak of butyl-amine is labeled in green.

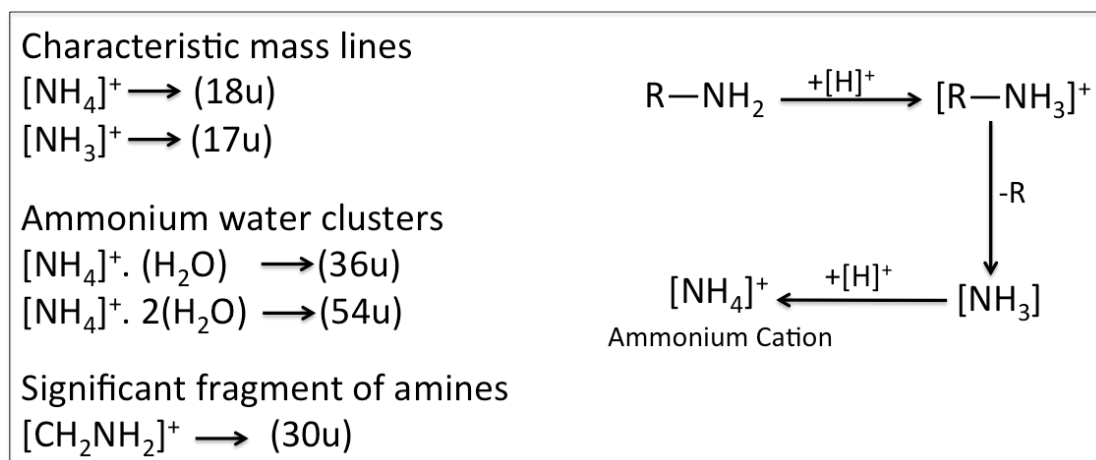


Figure 3.4: Possible fragmentation pathway of amines to produce an ammonium cation (Right). The most prominent features to characterize amines fragments in CDA Type-2 spectra are shown (Left).

3.2.1.2. Amine species as seen in CDA Type-2 spectra

The focus of this section is to analyze CDA Type-2 spectra, which show characteristic cationic features of amines previously identified in the laboratory (see section 3.2.1.1). The characteristic signature of amines $[\text{NH}_4]^+$ is identified in almost 8% of the total analyzed Type-2 spectra, which were recorded at impact velocities ≤ 8.5 km/s. Together with this mass line at 18u, in some spectra a peak at m/z 17 is also observed, which corresponds to $[\text{NH}_3]^+$. The figure below (Figure 3.5) shows a single ToF Type-2 mass spectrum of an organic rich E-ring ice grain, which strongly indicates amines.

The peak at m/z 18 is identified as an ammonium cation $[\text{NH}_4]^+$, which is characteristic to analogue spectra of amines (Table 3.2). Similar to $[\text{H}_3\text{O}]^+$ neutral-water-clusters, the neutral-water-clusters of ammonium cation $[\text{NH}_4]^+(\text{H}_2\text{O})_{n=1,2}$ are also observed (in Figure 3.5(c), left flanks (in red) of the first three water-cluster species). In addition, a peak at the right flank of 29u-feature is also highlighted in red, which can be attributed to $[\text{CH}_2\text{NH}_2]^+$. After 3.5 μs ToF, hydronium-water-clusters dominate the ammonium-water clusters.

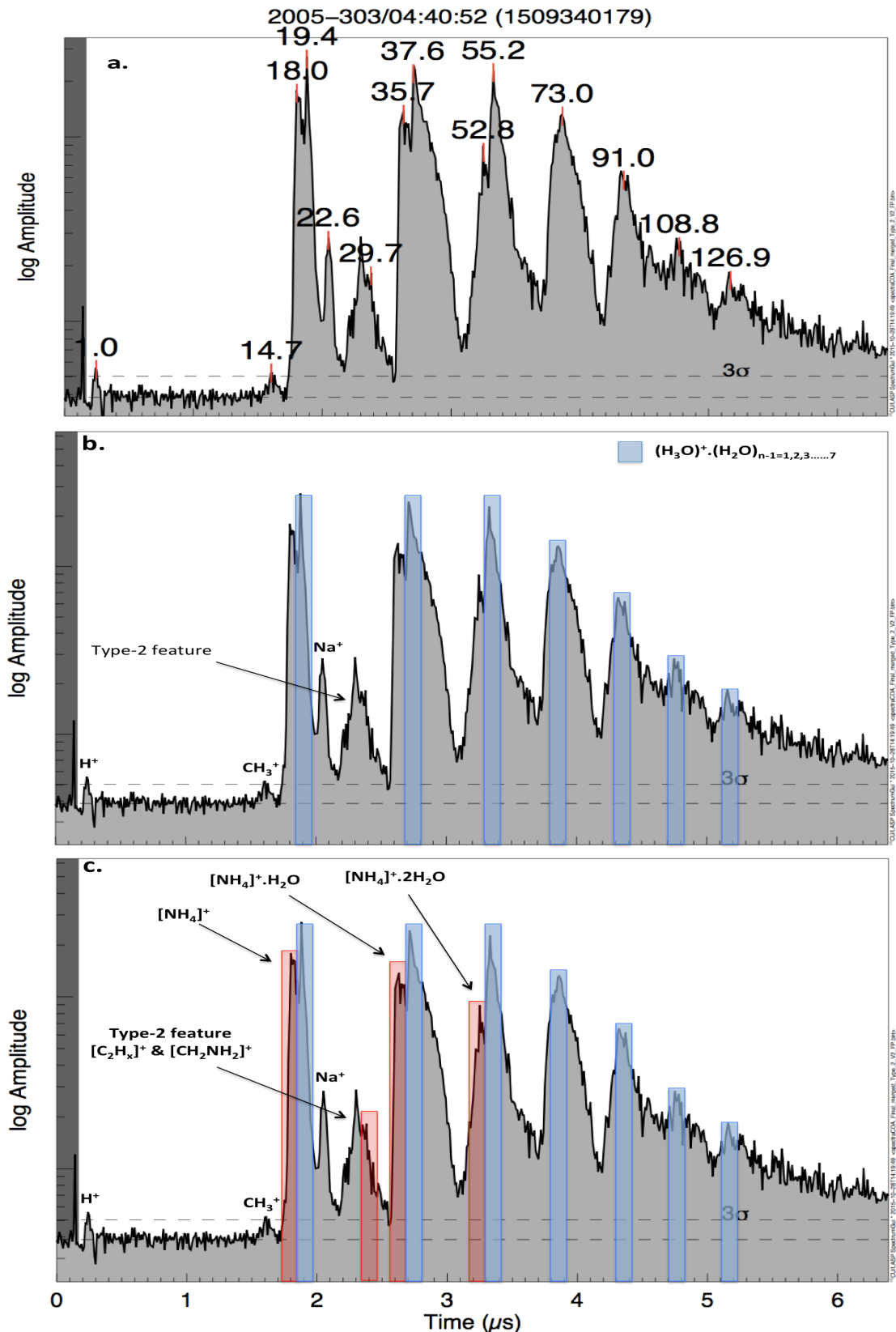


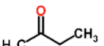
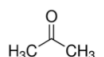
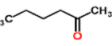
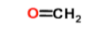
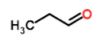
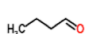
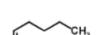

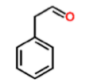
Figure 3.5: A systematic process to identify amine species in a CDA spectrum. Shown is a single ToF Type-2 mass spectrum of E-ring ice grain that exhibits signatures of amines. The spectrum was recorded at an impact velocity of 6.5 km/s. In each part a, b & c, peaks are labeled in a systematic way to identify non-water features. The pure water-clusters are highlighted in blue, whereas peaks that

correspond to amines are shown in red. The mass calibration of the spectrum is done with known reference mass lines (see section 3.2). The spectrum shows double peaks at a ToF of 1.8-2.0, 2.5-2.9 and 3.1-3.5 (μs). Above that, potential double peaks are not distinguishable. For details about water-clusters pattern in CDA spectra see section 2.4. The typical Type-2 feature (26-31 u) is also labeled along with other species including H^+ , CH_3^+ and Na^+ .

3.2.2. Identification of carbonyl species in E-ring ice grains

This section will demonstrate the identification of carbonyl species in E ring ice grains with the help of the analogue laboratory experiments. The ToF laboratory spectra were used to study the fragmentation pattern of carbonyl species in order to identify the characteristic cations of carbonyl species in CDA spectra.

Table 3.3: List of measured carbonyls Molecular weights and the most apparent ions in the spectra are listed.

Molecule	Formula	Structural formula	Mol. weight	Mol. peak	Acylium cation	Other significant peaks
<i>Ketones</i>						
2-Butanone	$\text{C}_4\text{H}_8\text{O}$		72	$[\text{M}+1]^+$	43	$[\text{M}-\text{OH}]^+$
Acetone	$\text{C}_3\text{H}_6\text{O}$		58	$[\text{M}+1]^+$	43	---
2-Hexanone	$\text{C}_6\text{H}_{12}\text{O}$		100	$[\text{M}+1]^+$	43	45 $[\text{M}-\text{OH}]^+$
<i>Aliphatic aldehydes</i>						
Formaldehyde	CH_2O		30	$[\text{M}+1]^+$	---	---
Propionaldehyde	$\text{C}_3\text{H}_6\text{O}$		58	$[\text{M}+1]^+$	43	31
Butanal	$\text{C}_4\text{H}_8\text{O}$		72	$[\text{M}+1]^+$	43	31, 45 $[\text{M}-\text{OH}]^+$
Pentanal	$\text{C}_5\text{H}_{10}\text{O}$		86	$[\text{M}+1]^+$	43	31, 45 $[\text{M}-\text{OH}]^+$
Hexanal	$\text{C}_6\text{H}_{12}\text{O}$		100	$[\text{M}+1]^+$	43	44, 45 $[\text{M}-\text{OH}]^+$
<i>Aromatic aldehydes</i>						
Phenylacetaldehyde	$\text{C}_8\text{H}_8\text{O}$		120	$[\text{M}+1]^+$	43	Aromatic fragments $[\text{M}-\text{OH}]^+$

3.2.2.1. Laboratory measurements

Different carbonyl compounds were selected to record analogue spectra. They are categorized into ketones, aliphatic aldehydes and aromatic aldehydes (Table 3.3). Different numbers of carbon atoms were measured for each category to see any variation in the fragmentation pattern.

The loss of OH from a carbonyl group molecule is observed in every tested compound with at least four carbon atoms (Figure 3.6) thus producing a cationic fragment $[M-OH]^+$. Aldehydes and ketones exhibited hydrogenated molecular cation $[M+1]^+$. A distinct fragment acylium cation at m/z 43 is observed in all carbonyl spectra.

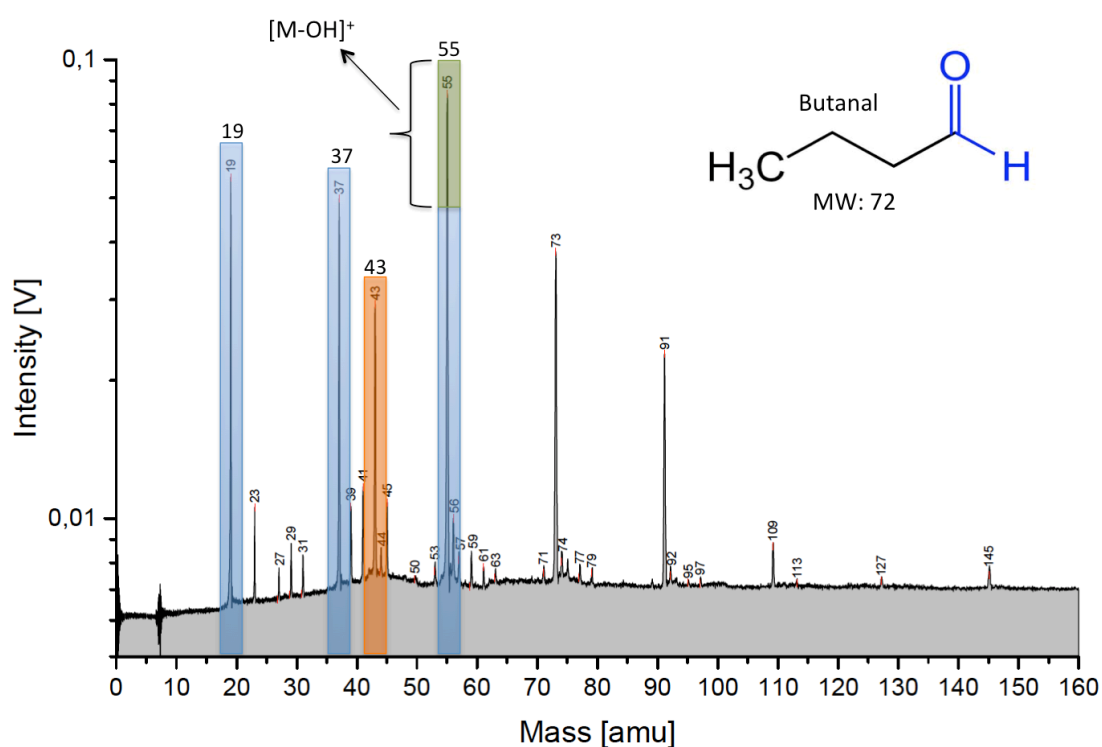


Figure 3.6: An intermediate delay time (see section 2.3) laboratory ToF mass spectrum of butanal at the concentration of 0.15 mol/kg in H_2O is shown. The rise of the amplitude at m/z 55 does not follow the peak pattern of water-cluster (in blue) species (for details of water-cluster patterns see section 2.4). The increased amplitude (in green) of the peak at m/z 55 indicates the presence of non-water specie, which in case of butanal would be $[M-OH]^+$.

Aldehydes and ketones undergo a molecular rearrangement known as McLafferty rearrangement (Figure 3.7) ((McLafferty & Turecek, 1993) & (Smith, 2004)). In this rearrangement hydrogen is transferred from the gamma-carbon of the carbonyl molecule to its double bonded oxygen. As a result an alkene is

eliminated, which leads to the formation of molecular fragment cation $[M-OH]^+$. For example the Butanal spectrum (Figure 3.6) shows a peak at m/z 55, which represents $[M-OH]^+$ in addition to the water-cluster. The loss of OH due to McLafferty rearrangement can be verified by an isotopic peak of $[M-OH]^+$ at m/z 56, which is an indicative of some non-water species at m/z 55.

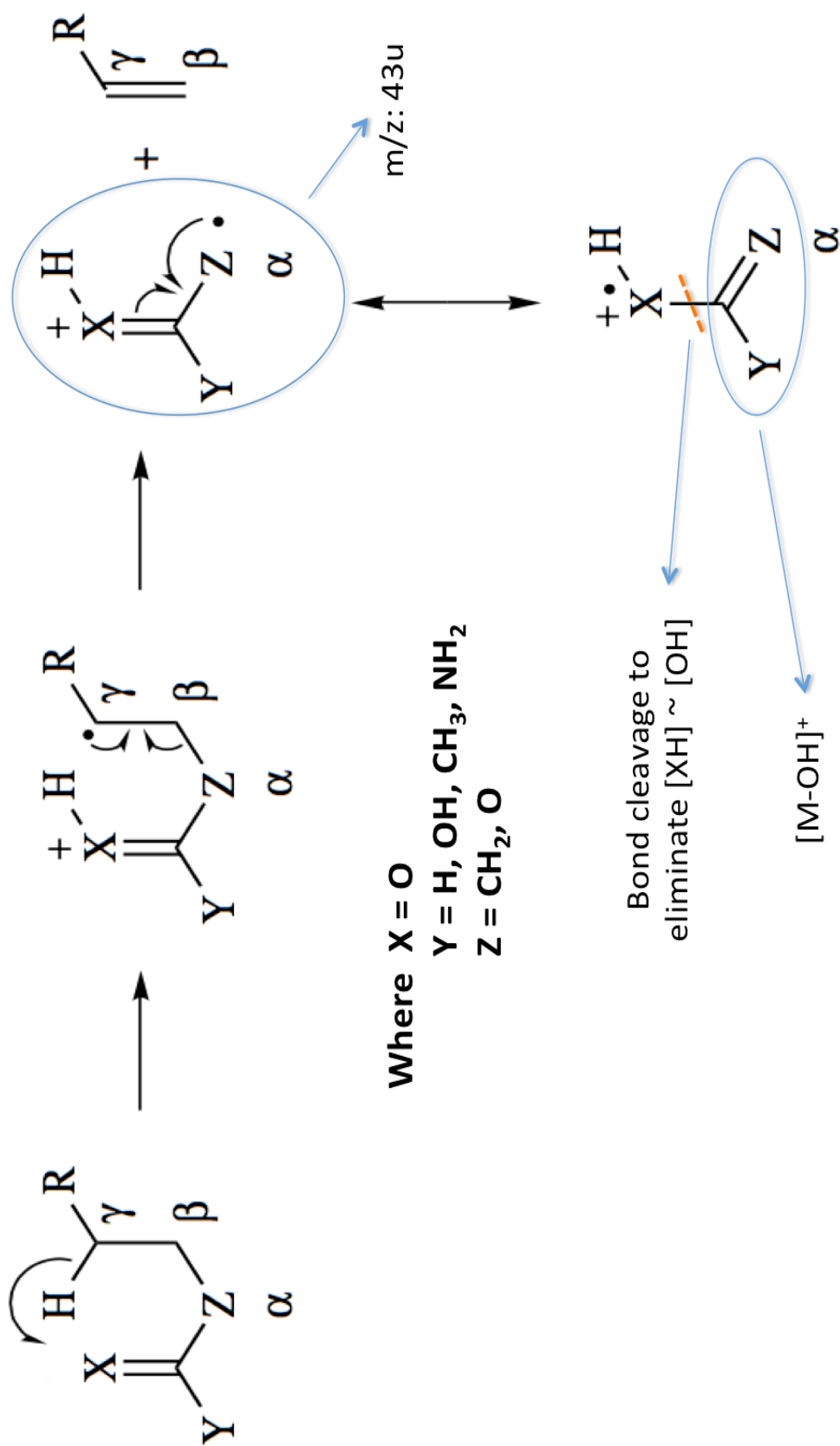


Figure 3.7 (Adapted and modified from (Smith, 2004)): A representation of the McLafferty rearrangement. The figure shows individual steps of the rearrangement of an H atom that is situated at the fourth C atom (gamma C), which contains functionality of the molecule. After the migration of an H atom from gamma C to the X atom ("O" in case of carbonyls) the carbonyl molecule transfers the double bond in between carbon (next to X) and the alpha C. At this stage the bond between alpha C and the beta C cleaves to produce an acylium cation ($m/z: 43u$). Simultaneously, the carbonyl molecule loses OH to produce $[\text{M}-\text{OH}]^+$ forming a respective peak in the mass spectrum.

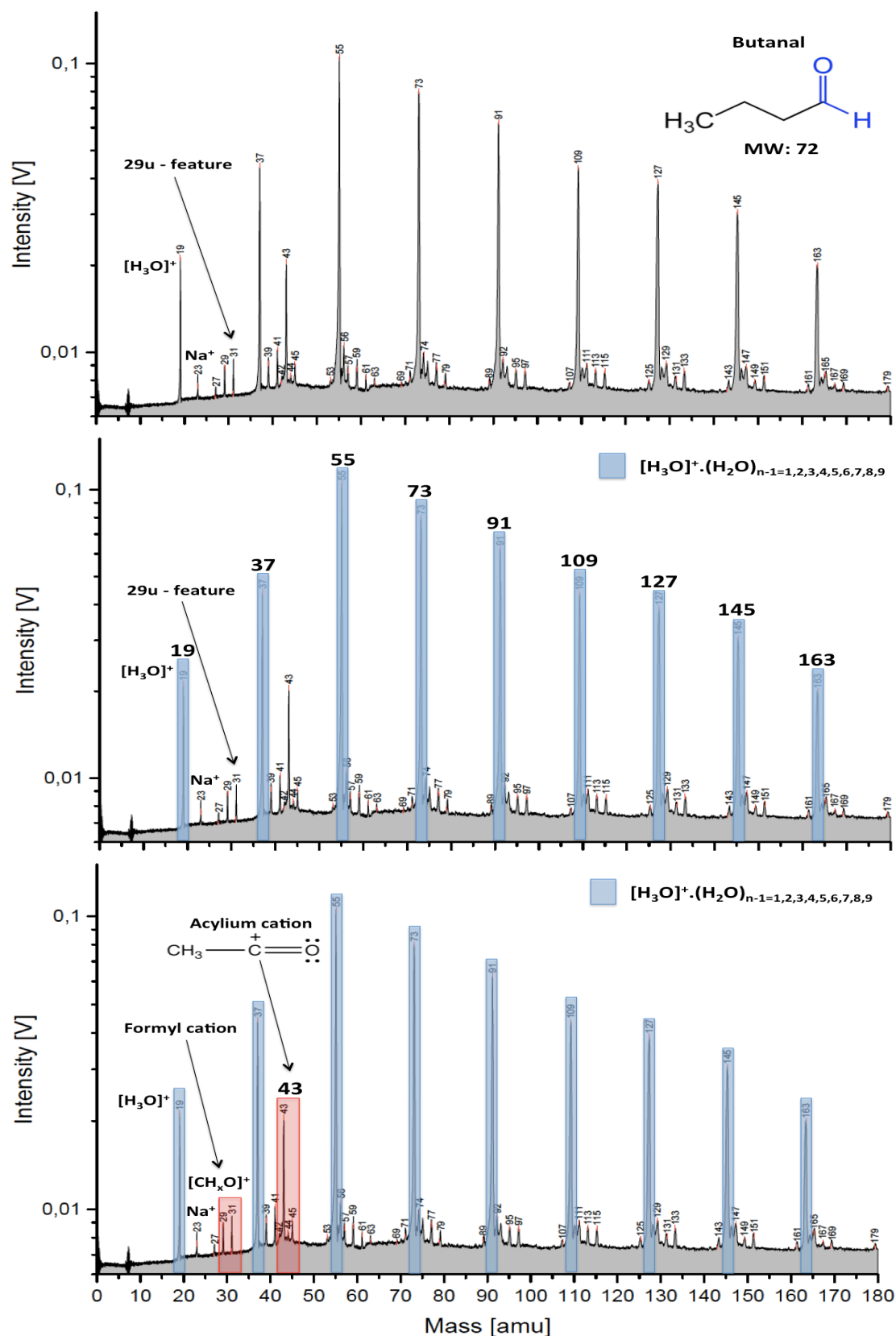


Figure 3.8: The analysis of a laboratory ToF mass spectrum of butanal at the concentration of 0.15 mol/kg in H_2O is shown in three steps. Different features in this spectrum are discussed systematically here. In the top spectrum hydronium and Na ions are labeled. Furthermore, species with m/z 27, 29, and 31 are labeled to be the equivalent to the 29u-feature in CDA spectra. In the middle spectrum

water-clusters are highlighted in blue. The bottom spectrum shows the characteristic acylium cation, of long-chained carbonyl group species. In addition a formyl cation is also shown in red. In CDA spectra a 29u-feature that is inclined towards the higher mass, due to the presence of $[\text{CH}_x\text{O}]^+$ with $x = 1$ or 3 (29 and 31u) can be indicative of carbonyl group species (see below).

3.2.2.2. Carbonyl species as seen in CDA Type-2 spectra

The main aim of this section is to discuss CDA ToF spectra of E ring ice grains, which show cations from carbonyl species. The laboratory spectra of carbonyl compounds (Figure 3.8) show the unique characteristic peak of carbonyls at m/z 43 $[\text{CH}_3\text{O}]^+$. Therefore, those CDA Type-2 spectra, which manifest a distinct peak at m/z 42.5—43.5, are considered as candidates for carbonyl Type-2 spectra. 6 % of the total analyzed Type-2 spectra are characterized as carbonyl Type-2 spectra. Like amines Type-2 spectra, most of the carbonyl Type-2 spectra were recorded at an impact speed below 8.5km/s. In the figure below (Figure 3.9), a typical CDA carbonyl-bearing spectrum is shown.

In figure 3.9(a), an analysis of carbonyl Type-2 mass spectrum is shown. The mass calibration is done with the know reference mass lines (see section 3.2). The water cluster species are highlighted in blue (Figure 3.9b). Hydronium peak and 29u-feature are also labeled. The characteristic fragments of carbonyls are shown in red (Figure 3.9c). In addition to m/z 43 $[\text{C}_2\text{H}_3\text{O}]^+$ the 29u-feature (in red) shows the tendency towards the higher end of its usual mass range (m/z 26 -31), which may represent $[\text{CH}_x\text{O}]^+$. Above 55u, mass lines turn broadened, indicative of the existence of water cluster with Na or organic species, along with the water clusters.

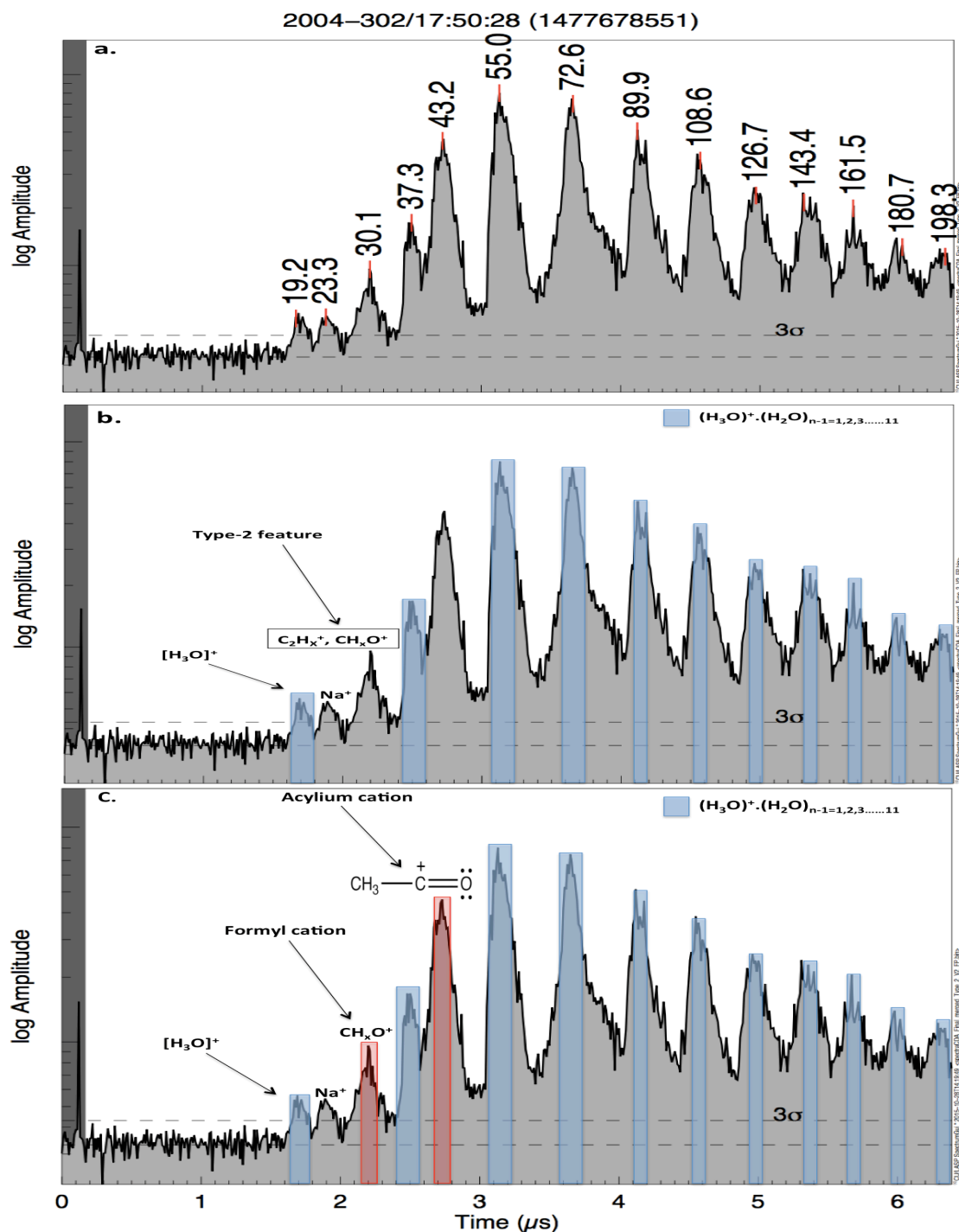


Figure 3.9: The analysis of a single ToF CDA Type-2 mass spectrum is presented in three steps. a) Mass calibration. b) Water-cluster species are highlighted in blue and possible Type-2 features are labeled. c) Acylium and formyl cations are shown in red, which are the most characteristic carbonyl fragments.

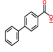
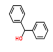
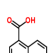
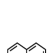

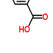
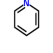
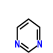
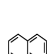

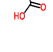
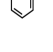
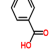
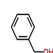
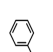
3.2.3. Identification of aromatic species in E-ring ice grains

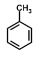
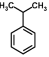
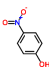
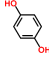
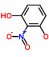
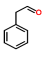
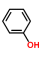
This section will demonstrate the identification of aromatic species in E ring ice grains. The laboratory ToF spectra will help to identify the characteristic fragment cations of aromatics species. The coincident pair of cationic fragments are also discussed and identified. In addition, complex organic features associated to aromatic species are also identified and discussed in the end of this section.

3.2.3.1. Laboratory measurements

The laboratory setup IR-MALDI-MS (see section 2.3) was used to identify and characterize the CDA aromatic Type-2 spectra. To investigate the pattern of aromatic fragments, different aromatic compounds were selected and measured (Table 3.4). Water solubility of aromatic compounds was the main selection criteria; specifically compounds exhibiting higher solubility at room temperature were preferred. Most of these compounds (Table 3.4) fragmented into a series of cations ($[C_nH_{\leq n}]^+$ where $n = 3,4,5,6,7$) known as aromatic cation series (McLafferty & Turecek, 1993). Although in some cases methanol and ethanol soluble compounds were also considered. Another important selection feature was to achieve the relative intensities of 76-79 (u) and 89-92 (u), as is observed in CDA spectra. Different classes of aromatics including N-cyclic, S-cyclic, O-cyclic and bi-cyclic were also measured to see the possibility of getting the characteristic fragment cation of aromatics i.e. 77u.

Table 3.4: List and summary of all aromatic compounds measured with the analogue experiment. Here, M^+ are molecular cations, $[M+1]^+$ and $[M+2]^+$ are hydrogenated molecular cations, $[M-1]^+$ are dehydrogenated molecular cations. Column 6 shows m/z values of detected fragments of the 7 shows significant fragment cations.

Molecule	Formula	Structural formula	Mol. weight	Mol. peak	Fragments of aromatic series	Other significant peaks
<i>Aromatics: Bi-cyclic</i>						
Biphenyl-4-carboxylic acid	$C_{13}H_{10}O_2$		198	---	---	---
Diphenylmethanol	$C_{13}H_{12}O$		184	$[M+1]^+$	---	$[M-OH]^+$ 102, 74
1-Naphthoic acid	$C_{11}H_8O_2$		172	$[M+1]^+$	---	$[M-OH]^+$, $[M-COOH+2H]^+$ 145
Naphthalene	$C_{10}H_8$		128	$[M-1]^+$	---	---
<i>Aromatics: N-cyclic</i>						
Nicotinic acid	$C_6H_5NO_2$		123	$[M+1]^+$	---	$[M-COOH+2H]^+$
Pyridine	C_5H_5N		79	$[M+1]^+$	---	$[2M+1]^+$
Pyrimidine	$C_4H_4N_2$		80	$[M+1]^+$	---	---
Quinoline	C_9H_7N		129	$[M+1]^+$, $[M+2]^+$	---	134, 136
<i>Aromatics: O-cyclic</i>						
2-Furoic acid	$C_5H_4O_3$		112	$[M+1]^+$	---	$[M-OH]^+$, $[M-COOH+2H]^+$
<i>Aromatics: 1-cyclic</i>						
Aniline	C_6H_7N		93	$[M+1]^+$	77, 67, 51, 39	---
Benzoic acid	$C_7H_6O_2$		122	$[M+1]^+$	79, 77, 67, 51	$[M-OH]^+$
Benzyl alcohol	C_7H_8O		108	$[M+1]^+$	91, 79, 65	---
Benzylamine	C_7H_9N		107	$[M-1]^+$	91, 79, 65	$[CH_2NH_2]^+$
Mandelonitrile	C_8H_7NO		133	$[M-1]^+$, M^+ $[M+1]^+$	79, 77, 51	$[M-OH]^+$, $[CH_2NH_2]^+$, $[NH_4]^+$
p-Toluenesulfonic acid	$C_7H_8O_3S$		172	$[M+1]^+$	91, 79, 65, 53, 39	$[M-OH]^+$ 107, 94, 81

Toluene	C ₇ H ₈		92	[M+1] ⁺	---	---
Cumene	C ₉ H ₁₂		120	[M+1] ⁺	---	---
4-Nitrophenol	C ₆ H ₅ NO ₃		139	[M+1] ⁺	---	[M-OH+H] ⁺ 93
Hydroquinone	C ₆ H ₆ O ₂		110	[M+1] ⁺	65	[M-OH] ⁺
2-Nitroresorcin	C ₆ H ₅ NO ₄		155	[M+1] ⁺	52	[M-OH] ⁺ , [M-NO ₂ +H] ⁺ , [NH ₄] ⁺ 82, 80, 70
Phenylacetaldehyde	C ₈ H ₈ O		120	[M+1]	91, 77, 79, 65	[M-OH] ⁺ , [M-CO+H] ⁺ [M-C ₆ H ₅] ⁺
Phenol	C ₆ H ₆ O		94	[M+1]	77, 67	---

Based on fragments of aromatic series (McLafferty & Turecek, 1993), as shown in table 3.4, I will discuss three groups of simple carbo-cyclic aromatic compounds (1-cyclic) in more detail (Figure 3.10), as most of them have good water solubility and they have shown aromatic cationic fragments.

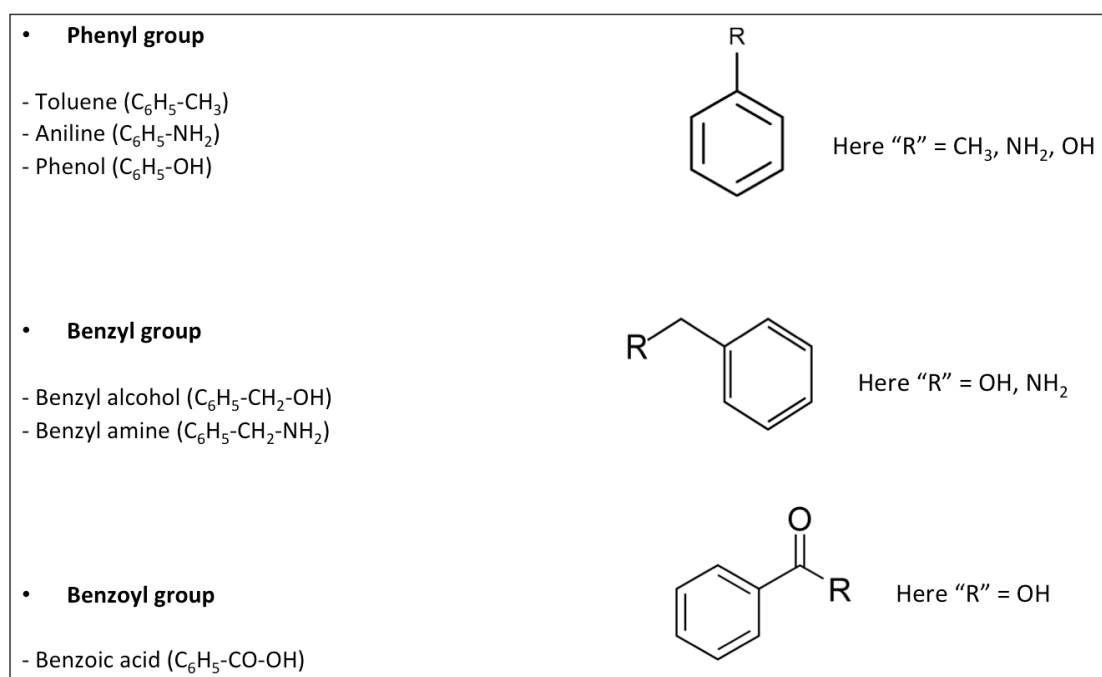


Figure 3.10: Three groups of aromatic compounds to study aromatic characteristic fragments.

In order to observe the characteristic fragments from each aromatic group, I used the laboratory spectra at the low delay time with 100% laser energy (see section 2.3) to avoid any possible interference from water cluster species or from any contaminant.

- Phenyl group species

The defining characteristic of phenyl group species is the functional group that is attached directly to a hexagonal benzene structure. Within this group, toluene ($C_6H_5-CH_3$), aniline ($C_6H_5-NH_2$) and phenol (C_6H_5-OH) were measured. Toluene has poor water solubility; therefore, the laboratory spectra of aniline and phenol were suited best to investigate the fragmentation process of phenyl group species.

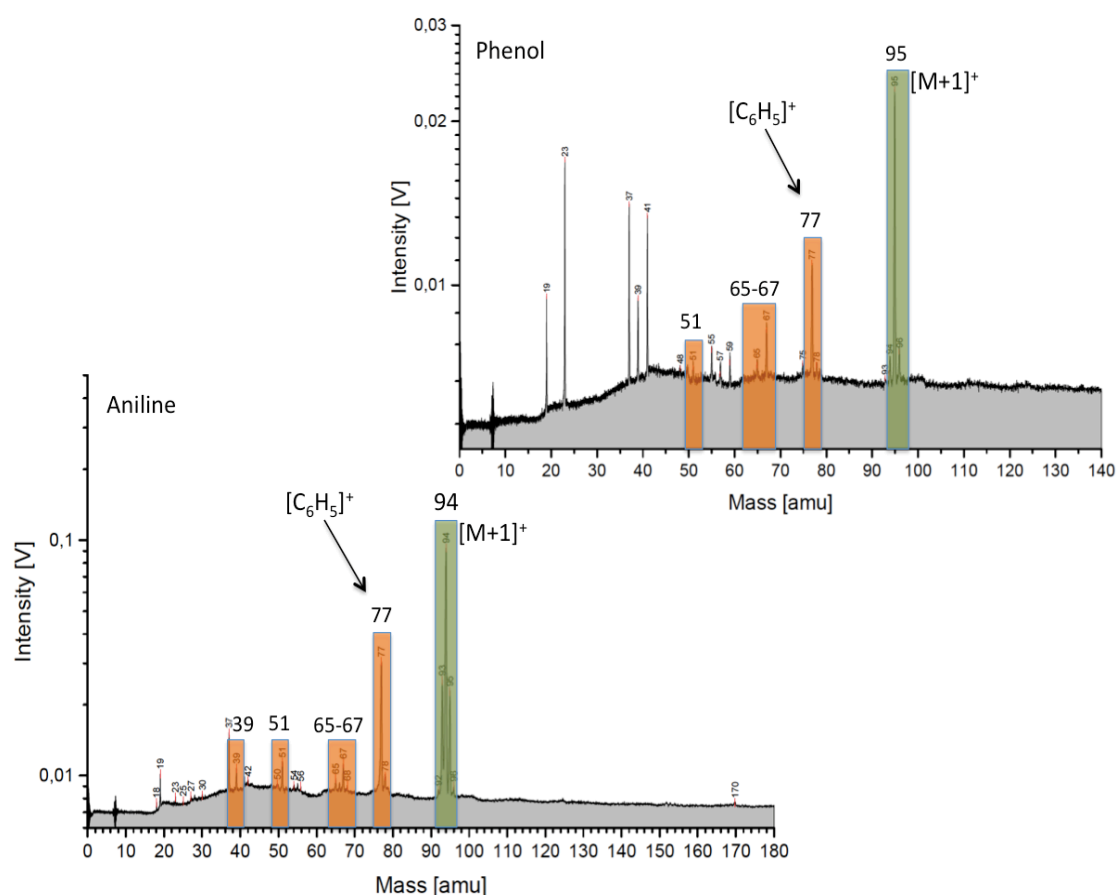


Figure 3.11: Laboratory spectra of phenol (Top) and aniline (Bottom) measured at concentrations of 0.05 mol/kg in H_2O . Protonated molecular peaks are shown in green. Aromatic cationic fragments are shown in orange. The characteristic fragment, a phenyl cation, of this aromatic group is also marked at m/z 77 as $[C_6H_5]^+$.

Figure 3.11 shows laboratory time of flight mass spectra of phenol and aniline. The abundant protonated molecular peak at $[M+1]^+$ is visible in both compounds. It is evident from the peak intensities that aniline ionizes easily (\sim 4-5 times higher amplitude) as compared to phenol. Both compounds show a prominent mass line at m/z 77, which is due to the cleavage of the bond between the benzene ring and the attached functional group. Aniline and phenol both lose

their respective functional groups, “NH₂” and “OH” to produce a phenyl cation, represented by mass line at 77u. Further fragmentation of the phenyl cation produces peaks at m/z 51-53 by losing neutral acetylene (C₂H₂), whereas another fragmentation pathway leads to cations with m/z 65-67 [C₅H_x]⁺. The distinct peak at m/z 39 might be due to the aromatic fragment [C₃H₃]⁺ at m/z 39 (Korth et al., 1989), but a contribution of K⁺ cannot be ruled out because of sample contamination. As an example (Figure 3.11) the mass line at 39u in the Phenol spectrum can be mostly due to K-contamination because the presence of Na at 23u indicates a general alkali metal contamination of the sample. In contrast, in the aniline spectrum the mass line at 39u is most likely an aromatic fragment indicated by the very low level of Na-contamination.

- Benzyl group species

In Benzyl group species, the functional group is attached to one or more hydrogen-saturated carbons (CH₂), attached to the benzene ring (C₆H₅-CH₂-R). Two Benzyl group compounds were analyzed, benzyl-alcohol and benzyl-amine.

Figure 3.12 shows the laboratory time of flight spectra of benzyl-alcohol and benzyl-amine. Comparing the peak intensities of both spectra shows that benzyl amine easily forms (~ 10-15 times higher amplitude) ionic fragments than benzyl alcohol. In contrast to phenyl group compounds, benzyl group species produce a dominant peak at m/z 91, known as the benzyl cation or tropylium cation. The bond between the functional group (R) and the rest of the molecule is cleaved to produce a benzyl cation [C₆H₅-CH₂]⁺, which then forms a resonance structure as tropylium cation [C₇H₇]⁺ (Figure 3.14). Both spectra show minor amounts of benzenium cations [C₆H₇]⁺ (also known as arenium) at m/z 79. The loss of neutral acetylene (C₂H₂) from a tropylium cation [C₇H₇]⁺ produces the species at m/z 65 [C₆H₅]⁺ and 39 [C₃H₃]⁺.

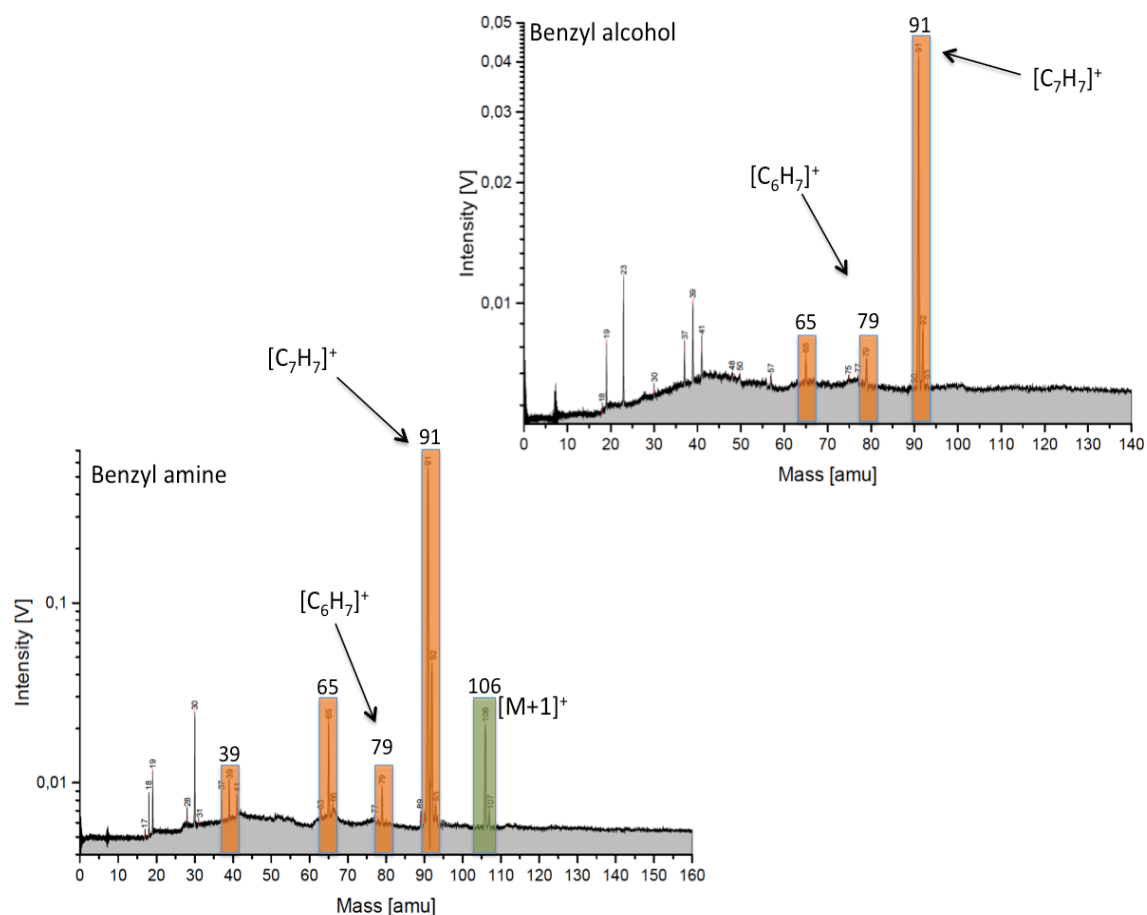


Figure 3.12: Laboratory spectra of benzyl alcohol (Top) and benzyl amine (Bottom) at concentration of 0.05 mol/kg in H_2O . The protonated molecular peak of benzyl amine is marked in green, whereas no molecular peak is observed in the benzyl alcohol spectrum. Aromatic cationic fragments are shown in orange. Tropylium and arenium (protonated benzene) cations are also marked as $[C_7H_7]^+$ and $[C_6H_7]^+$.

- Benzoyl group species

In Benzoyl group species, the hexagonal structure is directly attached to a carbon atom that has a double bond with oxygen (C_6H_5-CO-R). From this group, benzoic acid ($C_6H_5-CO-OH$) was analyzed.

Figure 3.13 shows the laboratory ToF mass spectrum of benzoic acid. Similar to benzyl amine and aniline, benzoic acid is also easy to ionize and to fragment. Similar to phenyl group compounds, Benzoyl group compounds produce a phenyl cation $[C_6H_5]^+$ at m/z 77, by cleavage of “CO-R” and the benzene ring. The prominent arenium ion at m/z 79, is striking $[C_6H_7]^+$. Minor peaks of the aromatic series (Table 3.5) at m/z = 65-76, 51-53 & 39 are also observed. The peak at m/z 105 $[M-OH]^+$ is very prominent, but is of less importance for this

analysis as in this case the loss of OH do not give any information of aromatic fragment series.

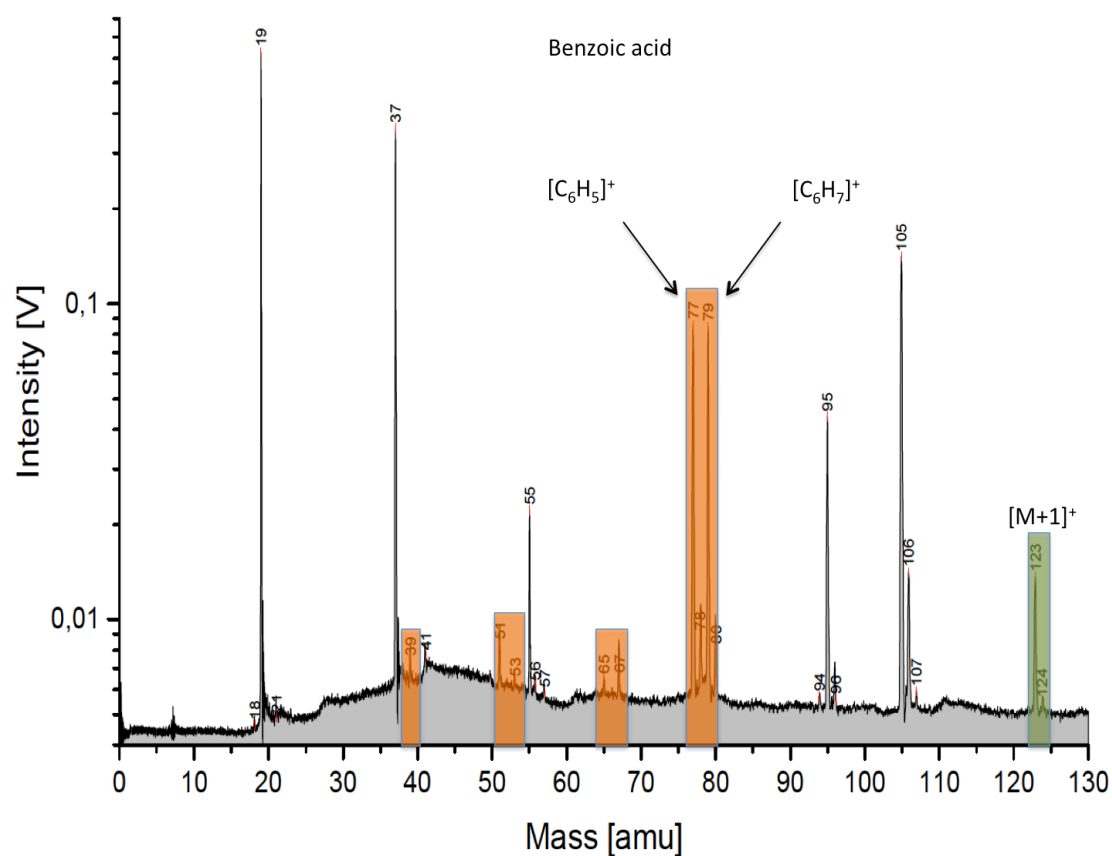


Figure 3.13: Laboratory spectrum of benzoic acid measured at the concentration of 0.025 mol/kg in H_2O . The protonated molecular peak of benzoic acid is shown in green. The prominent peak at m/z 105 shows the loss of OH from benzoic acid $[M-OH]^+$. Aromatic cationic fragments are shown in orange. Phenyl (deprotonated benzene) and arenium (protonated benzene) cations are also marked as $[C_6H_5]^+$ and $[C_6H_7]^+$.

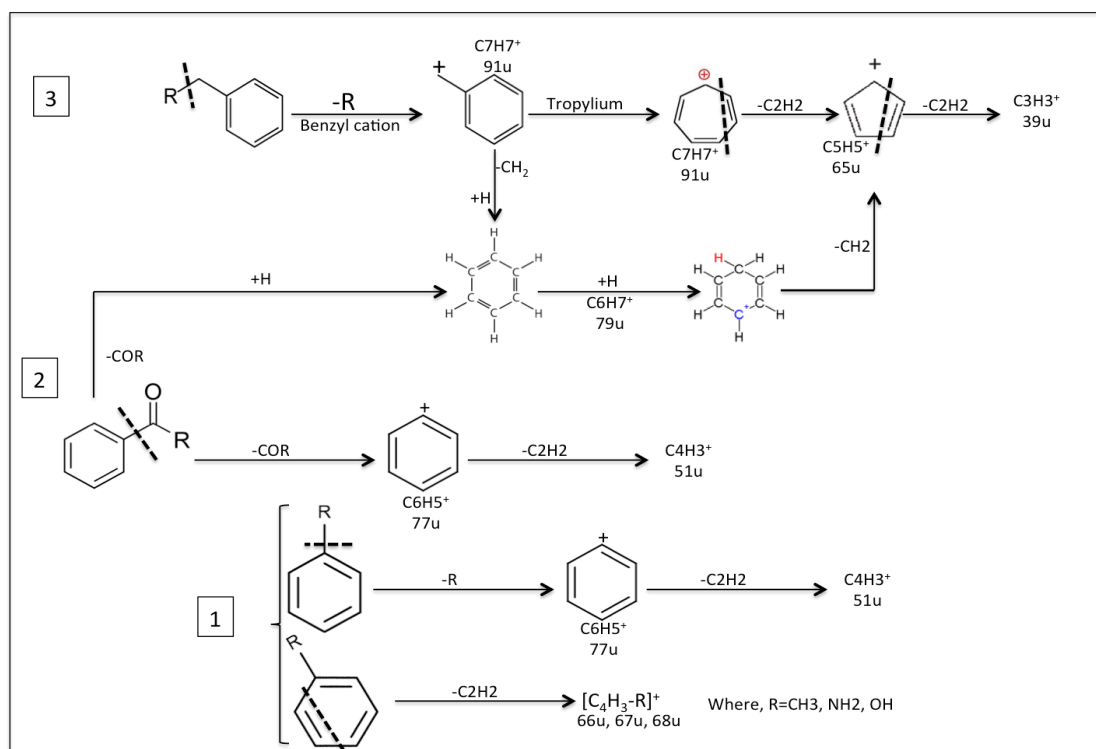


Figure 3.14: Fragmentation pathways of three aromatic families. (1) Phenyl group species: The most likely fragmentation mechanism for phenyl group compounds is to lose the attached functional group or rest (R) to produce a phenyl cation [C_6H_5] $^+$ at m/z 77. Subsequently, the phenyl cation can lose acetylene (C_2H_2) to produce a small peak [C_4H_3] $^+$ at m/z 51. In a less likely fragmentation pathway, phenyl group species can also produce minor peaks at m/z 66, 67 and 68. (2) Benzoyl group species: The most likely fragmentation pathway for benzoyl group compounds is to lose $CO-R$ to produce a phenyl cation at m/z 77. The phenyl cation can lose acetylene to produce a small peak at m/z 51. In an alternative pathway, benzoyl produces an arenium cation [C_7H_7] $^+$ at m/z 79, which again can lose acetylene to produce a cation at m/z 67 i.e., $65+2H$. (3) Benzyl group species: Benzyl group compounds lose its attached group (R) to produce a benzyl cation, which then rearranges itself to form a resonance stabilized structure known as tropylium cation at m/z 91. Alternatively, the Benzyl cation loses CH_2 , followed by protonation to produce an arenium cation at m/z 79. Tropylium cation fragmentation produces m/z 65 and 39 by losing neutral acetylene consecutively.

Based on the analysis of the analogue laboratory spectra the characteristic cationic fragments of aromatic compounds cation are explained and the criteria are set to identify aromatic species from CDA Type-2 spectra of E ring ice grains as shown in table 3.5. To identify aromatic species in CDA spectra the mass line(s) at m/z 76–79 and 89–91 (u) must be observed, which correspond to phenyl and tropylium cations. In addition the coincident fragments ($C_4H_x^+$ and $C_5H_x^+$) of phenyl and/or tropylium cation can support the evidence.

Table 3.5: Summary of the aromatic fragment series from three groups of aromatic compounds.

Aromatic series (m/z)	Cation	Phenyl group (C ₆ H ₅ -R)	Benzyl group (C ₆ H ₅ -CH ₂ -R)	Benzoyl group (C ₆ H ₅ -CO-R)
39	C ₃ H ₃ ⁺	minor	minor	minor
50-52 (53)	C ₄ H _x ⁺	Yes No	No No	Yes minor
63-65 (67)	C ₅ H _x ⁺	minor Yes	Yes No	minor Yes
76-78 (79)	C ₆ H _x ⁺	Yes No	No minor	Yes Yes
89-91 (93)	C ₇ H _x ⁺	No No	Yes No	No No

- The mixture – benzyl group specie + benzoyl group specie

Finally two different types of aromatic compounds were mixed (Figure 3.15) in certain proportions to observe full range of aromatic fragment series as shown in table 3.5. Also each member of this series is accompanied with the respective protonated peak. As shown in the figure 3.15, benzoic acid (i.e. benzoyl group) produces phenyl cations [C₆H₅]⁺, [C₆H₇]⁺ and phenyl acetaldehyde (i.e. benzyl group) produces tropylium cations [C₇H₇]⁺, [C₇H₉]⁺. Here a part of the aromatic fragment series i.e., 51-53, 77-79 (u) comes from benzoic acid and the remaining part i.e. 65-67, 91-93 (u) comes from phenyl acetaldehyde. This measurement shows the possibility that multiple aromatic compounds can reproduce similar aromatic features seen in CDA aromatic Type-2 spectra (see section 3.2.3.2).

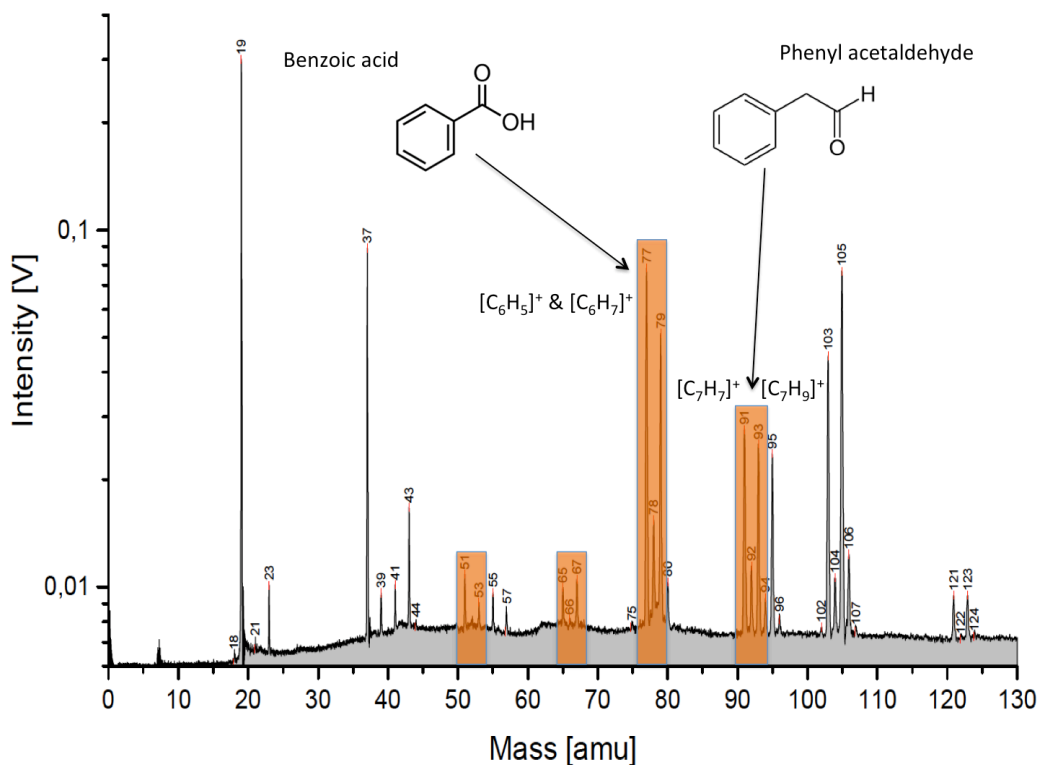


Figure 3.15: Laboratory spectrum of the mixture of benzoic acid and phenyl acetaldehyde measured at concentration of benzoic acid (0.026 mol/kg) and phenyl acetaldehyde (0.015 mol/kg) in H₂O. Aromatic cationic fragments are shown in orange.

3.2.3.2. Aromatic species as seen in CDA Type-2 spectra

About 7% of the analyzed Type-2 mass spectra show unique non-water features that I attribute to aromatic species. For instance, some of Type-2 spectra show a significant peak at m/z 76-79 and also obvious excess at m/z 89-92, which suggests the presence of aromatic compounds (Table 3.5). In these spectra other conjoint peaks at m/z 38-40, 50-53 and 63-67 can be often observed. This peak pattern indicates the presence of cationic aromatic fragments series (Table 3.1, 3.4 & 3.5).

2005-068/19:44:34 (1489090271)

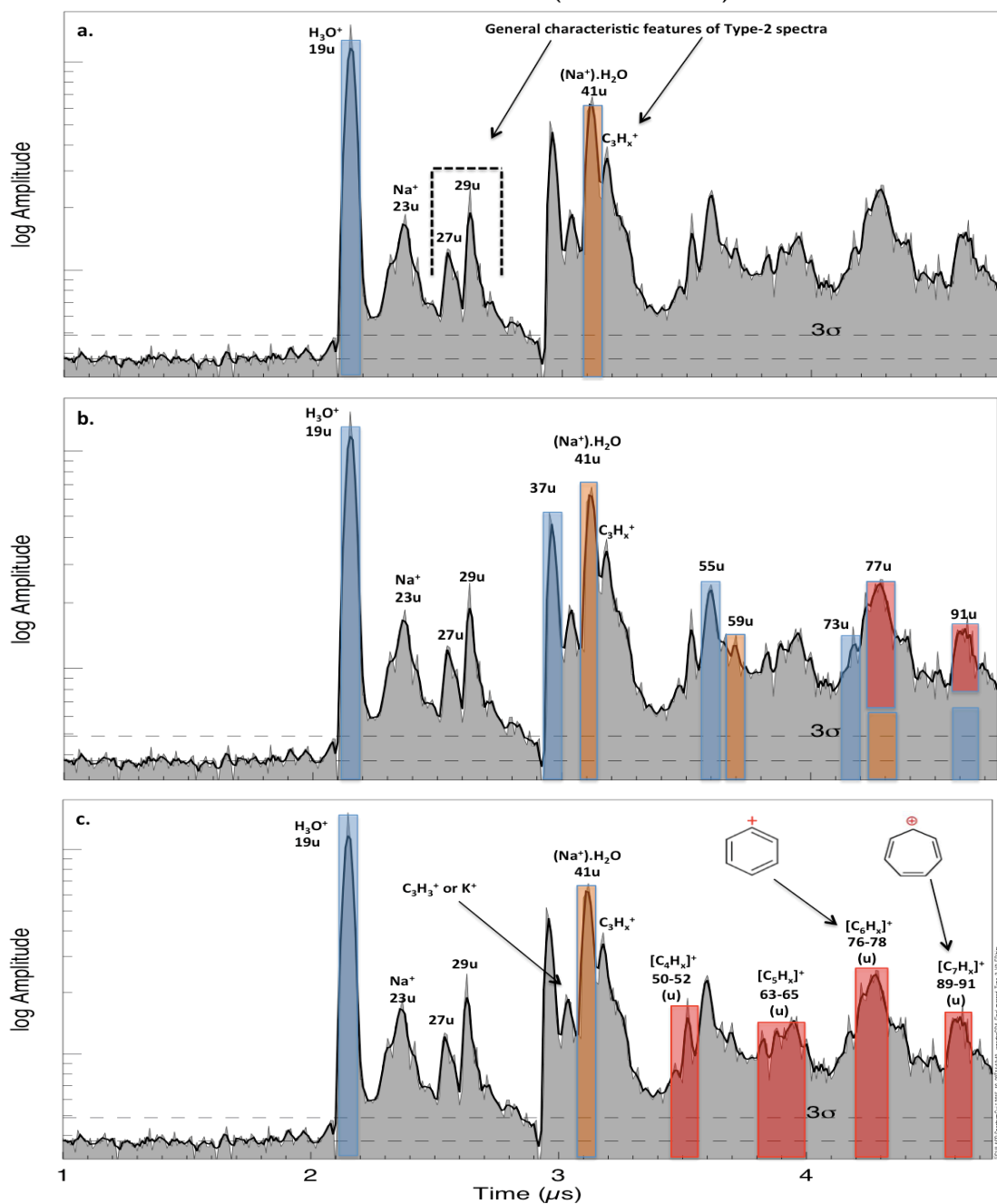


Figure 3.16: Systematic process to identify aromatic fragments. Shown is a single ToF Type-2 mass spectrum of an E-ring ice grain exhibiting signatures of aromatic compounds. In each part of figure 3.16 (a, b & c), peaks are labeled in a systematic way to identify non-water features, possibly, cationic aromatic fragments. The spectrum was recorded at an impact velocity of about 8 – 9 km/s. The pure water-clusters are highlighted in blue; possible Na-water clusters are shown in orange and aromatic characteristic species are highlighted in red stripes.

- **3.16a.** The mass calibration of the spectrum is done with the known reference mass lines (see section 3.2). The 29u-feature is also shown together with $[C_3H_x]^+$ species as general features of Type-2 spectra.

- **3.16b.** Pattern of water-clusters and Na-water clusters are shown in blue and orange stripes, respectively. The water-cluster species appear as $[\text{H}_3\text{O}]^+(\text{H}_2\text{O})_{n-1}$, where $n=1,2,3$, whereas Na-water clusters appear as $[\text{Na}]^+(\text{H}_2\text{O})_n$, where $n=1,2$ and already discussed in detail in section 2.4. The two colored stripes at m/z 77 and 91 each represent two or more unresolved.
- **3.16c.** The cationic fragments from organic compounds are emphasized. Only the first pure water-cluster and Na-water cluster species are highlighted. The peaks amplitudes at m/z 77 and 91 suggest conjoint identification of the phenyl cation $[\text{C}_6\text{H}_5]^+$ and tropylium cation $[\text{C}_7\text{H}_7]^+$. In addition, the cationic fragments $[\text{C}_5\text{H}_x]^+$ and $[\text{C}_4\text{H}_x]^+$ are also present. Another distinct peak at m/z 39 is observed that might be aromatic cation, cyclo-propenyl $[\text{C}_3\text{H}_3]^+$ or produced by unsaturated hydrocarbon chain $[\text{C}_n\text{H}_{2n-3}]^+$ (Korth et al., 1989 & 1990). However, this can also be due to potassium $[\text{K}]^+$ as described by (Postberg et al., 2008) (see also section 3.2.3.1— phenyl group species). The in general broad peaks in the spectrum indicate the possibility of ions from other organic species.

3.2.3.3. Complex aromatic material

Some CDA aromatic Type-2 spectra show a distinct sequence of mass lines at higher m/z values above 91u (Figure 3.17). The difference between mass lines in this consecutive pattern is $\Delta m \sim 11-13$, indicative of unsaturated organic fragments, probably from aromatic breakup. It extends to the end of CDA spectrum recording at about 190u, indicative of fragments from parent molecules far beyond the recorded mass range. About one third of aromatic Type-2 spectra show the above-mentioned sequence of m/z values above 76-79 (u).

Figure 3.17 (top) shows an aromatic Type-2 mass spectrum where peaks are labeled with m/z values of ions corresponding to their time of flights. The spectrum is calibrated with the hydronium peak at m/z 19.

The same spectrum, (Figure 3.17 bottom) is labeled in different colors to differentiate the aromatic and complex organic features from water-cluster species (blue).

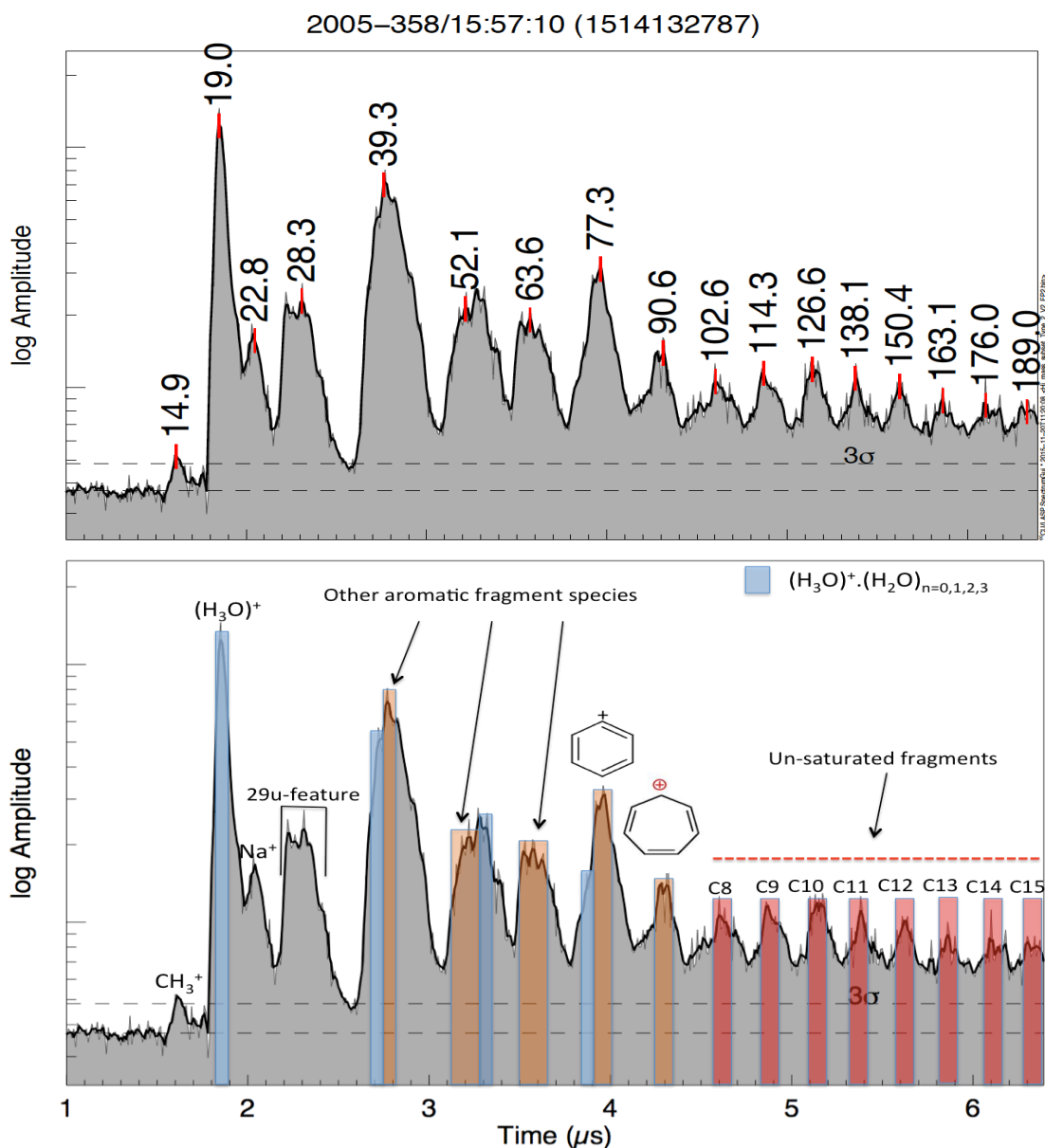


Figure 3.17: CDA aromatic Type-2 spectrum associated with highly un-saturated fragments of a complex organic material. (Top) Calibration of the spectrum is shown and peaks are marked by their m/z values corresponding to their time of flights. (Bottom) The peaks are colored differently to distinguish the pattern of each kind of species. In blue stripes, water clusters are shown. The aromatic fragments series is shown in orange stripes, whereas the carbon sequence of un-saturated fragments is shown in red. Structures of the phenyl $[\text{C}_6\text{H}_x]^+$ and tropylium $[\text{C}_7\text{H}_x]^+$ cations are shown. The coincident aromatic fragment cations ($[\text{C}_3\text{H}_x]^+$, $[\text{C}_4\text{H}_x]^+$ & $[\text{C}_5\text{H}_x]^+$) are pointed out here as “other aromatic fragment species”. Above the mass of the tropylium cation, a series of consecutive highly un-saturated ($\Delta m \sim 11\text{-}13$) fragment cations are labeled showing the hydrocarbon-sequence up-to $\sim \text{C}_{15}$.

3.3. Discussion and conclusion

Based on the peak patterns of certain CDA Type-2 spectra of Enceladian ice grains, the characteristic fragments of three organic families (amines, carbonyls & aromatics) were identified. These peak patterns along-with the characteristic cationic fragments were reproduced and verified by the analogue experiment (IR-MALDI-ToF-MS), by testing various organic compounds.

The defining fragments of amine, carbonyl and aromatic species were clearly visible in 8%, 6% and 7% of Type-2 spectra, respectively. However there were large numbers of Type-2 spectra that contain signatures of these organic fragments, but are less obvious and significant due to relatively low mass resolution of CDA spectra. In addition, some Type-2 spectra showed combined characteristic fragments of several or all three organic families i.e. amines, carbonyls and aromatics. Furthermore, many Type-2 spectra exhibited signatures that probably could be the fragments from other, yet unspecified, organic families that will be subject of future work.

The detailed discussion of each sub-type of Type-2 spectra is presented in the following sections.

3.3.1. Amines

The decisive mass line to ensure the presence of amines is the peak at m/z 18, which corresponds to $[\text{NH}_4]^+$.

A peak at m/z 18 in principle can also be due to $[\text{H}_2\text{O}]^+$ as observed in some of the non-amines laboratory spectra or Type 1 CDA spectra, where 18u appears as a minor peak. Previous studies ((Hillier et al., 2007b) & (Postberg et al., 2008)) also reported a minor peak at m/z 18 in E ring ice spectra and argued that besides $[\text{H}_3\text{O}]^+$ the peak at m/z 18 could also be $[\text{NH}_4]^+$. However, $[\text{H}_2\text{O}]^+$ is exclusively observed at the highest laser energy with low delay time (see section 2.3) in the lab and only at high impact speeds (> 12 km/s) in CDA spectra. Even in these high-energy impacts, the observed amplitude ratio of $[\text{H}_3\text{O}]^+ / [\text{H}_2\text{O}]^+$ is around 10 or higher.

In contrast a peak at m/z 18 is exclusively observed in Type 2 spectra at impact speeds ≤ 10 km/s, thus strongly indicating an organic origin. Therefore, one can safely identify $[\text{NH}_4]^+$ in cases where a strong mass line appears at 18u at speeds below 10 km/s.

Amine lab spectra also showed a pronounced peak at m/z 30, which is another characteristic amine fragment cation $[\text{CH}_2\text{NH}_2]^+$. In CDA amine Type-2 spectra, 30u is often undistinguishable as a single detached peak from the multitude of organic species around 29u. Therefore, 30u is not considered exclusively for the detection of amines species in CDA Type-2 spectra but can in some cases be used, together with the 18u mass line, as a supporting argument for amines.

3.3.2. Carbonyls

Analogue laboratory spectra show three characteristic fragment cations to identify carbonyl species; (i) $[\text{M-OH}]^+$ (ii) $[\text{CH}_x\text{O}^+ : 29-31 \text{ u}]$ and (iii) $[\text{C}_2\text{H}_3\text{O}^+ : 43\text{u}]$ (Figure 3.6 & 3.8).

To produce $[\text{M-OH}]^+$, the McLafferty mechanism requires a carbonyl molecule with at least 4 carbon atoms. In CDA spectra $[\text{M-OH}]^+$ can interfere with water cluster species or water/Na cluster species and is hence sometimes difficult to identify in Type-2 spectra.

The most important identifier of carbonyl species in CDA Type-2 spectra is the acylium cation, forming a mass line at m/z 43. Except formaldehyde all carbonyl group species produce acylium cations (Table 3.3). In this thesis, a positive detection of carbonyl Type-2 spectra is considered only, if 43u is higher than the adjacent peaks at 39 & 41, which are either $[\text{K}]^+$ and $[\text{Na}]^+(\text{H}_2\text{O})$ species or probably propyl cations $[\text{C}_3\text{H}_x]^+$. This assumption was largely investigated in the laboratory (Figure 3.8) using different carbonyl compounds (Table 3.3). In this way, the peak (43u) is clearly detached from the water-cluster peak at m/z 37 $[\text{H}_3\text{O}]^+(\text{H}_2\text{O})$. A strong acylium ion, mass line often forms water clusters of the acylium cation $[\text{C}_2\text{H}_3\text{O}]^+(\text{H}_2\text{O})_n$ that appear at the right flanks of pure water-clusters. The aforementioned stringent criterion was used to rule out the interference of other species around 43u in CDA carbonyl Type-2 spectra; therefore, there might be some carbonyl-bearing spectra that were not considered.

This distinct peak at m/z 43 is often supported by a '29u- feature' that peaks at about 31u, suggesting the presence of carbonyl species in E ring ice grains. Hillier et al., 2007b, identified 31u as a water-carbon cluster [$C(H_2O)^+$ and $C(H_2O)^+$]. Postberg et al., 2008 also considered 30-31 (u) as carbon water clusters and correlated the peak (s) with C^+ signature. In addition Postberg et al., 2008 also interpreted [CH_3O] $^+$ as an ion fragment of alcohols. Both studies did not mention carbonyl species as a possible source of the peak (s) 29-31 (u). In this work, the laboratory spectra of carbonyl showed mass lines m/z 29-31 that correspond to a formyl cation – a carbonyl fragment cation. Often the formyl cation is not distinguishable due to multitude of adjacent organic species (29u-feature) in CDA Type-2 spectra. As mentioned above, together with an acylium cation (43u) the tilted 29u-feature towards a higher mass are supporting evidence for the presence of carbonyl species.

The hydronium peak [H_3O] $^+$ is strongly suppressed in most carbonyl Type-2 spectra as compared to amines and aromatic Type-2 spectra. In contrast to amines (see section 3.2.1) and aromatic Type-2 spectra (see section 3.2.3), methyl cations [CH_3] $^+$ are not observed in most of the carbonyl Type-2 spectra.

3.3.3. Aromatics

In analogue laboratory spectra it was observed that phenyl and benzoyl groups compounds exclusively produce [$C_6H_5^+$: 77u, phenyl cation] as dominant aromatic fragment (Figure 3.11 & 3.13), whereas benzyl group species produce [$C_7H_7^+$: 91u, tropylium cation] as dominant aromatic fragment (Figure 3.12). In addition, the peaks at m/z 50-53 and 63-67 show the loss of neutral acetylene (C_2H_2) (Srama et al., 2009) from phenyl and tropylium cations.

In CDA aromatic Type-2 spectra, the most abundant non-water peak is observed at m/z 77-79 together with other coincidence peaks at m/z 38-39, 50-52, 63-65 and 89-91. In all these spectra, the peak amplitude of 91u is much lower than the one at 77u. After the hydronium peak, an exponential decrease is observed in the amplitude of water-cluster peaks. The pure-water and Na-water clusters species are highly suppressed by aromatic species after 37u and 59u, respectively.

A comparison of the laboratory and in-situ CDA spectra showed two possible scenarios to produce phenyl cation (77-79 (u)) as a dominant fragment together with the other coincident cations of aromatic fragment series: i) if a functional group (R) is directly attached to the benzene ring, as in the case of phenyl group or ii) if the carbon next to the benzene ring lacks hydrogen (un-saturated carbon in-terms of hydrogen), as shown in the case of benzoyl group. The laboratory spectra of phenyl and benzoyl groups verified the peak pattern of aromatic fragment cations (m/z 89-91, 76-78, 63-65, 50-52) in CDA Type-2 spectra.

The FWHM and amplitudes of the coincidence peaks at m/z 50-52 and 63-65 depends on the impact conditions. It is observed that the aromatic CDA spectra recorded at impact velocities ≥ 10 km/s show relatively well-resolved (thin) peaks at m/z 50-52 and 63-65. This means that at high impact speeds the aromatic fragments are better confined within a small mass range (e.g., 50-52) compared to lower impact speeds, where the distribution of fragment mass lines is generally broader. The increase in amplitudes of these species at higher impact velocities indicates abundant ion production from fragmentation of aromatic species.

In some of the high impact speed spectra the peak at m/z 63-65 shifts towards m/z i.e. 61-63, which might be due to the elimination of hydrogen (s) to produce highly unsaturated fragment specie.

In a previous study Postberg et al., 2008 observed features at m/z 75-78 and 64-68 in Typ-2 spectra, and pointed out an organic nature of these mass regions but did not discuss an aromatic origin. In another study, Cassini's INMS reported the evidence of benzene $[C_6H_6]^+$ in the plume (Waite et al., 2009). In general, the above-described findings are in agreement with the results presented in this work.

3.3.3.1. N- or O- bearing fragments ions

Some of CDA aromatic spectra show also the characteristic peaks of amines (m/z 18) and/or carbonyl (m/z 43), which could be an indication of N- and/or O-bearing aromatic species.

In addition a mass line at m/z 44-45 is occasionally observed. According to our analogue spectra amines, alcohols and carbonyls all can create a signature here. In case of amine the mass line at 44u $[\text{C}_2\text{H}_4\text{NH}_2]^+$ is a coincident fragment with the one at 30u $[\text{CH}_2\text{NH}_2]^+$ and 18u $[\text{NH}_4^+]$. Therefore the origin of 44u in aromatic Type-2 spectra could be attributed to amine species, if $[\text{NH}_4^+ : 18\text{u}]$ is present and the maxima of broad 29-feature is shifted toward higher mass. A distinct peak at 45u could be a fragment from alcohol as $[\text{C}_2\text{H}_4\text{OH}]^+$, if the 29-feature is shifted towards higher mass to represent $[\text{CH}_2\text{OH}]^+$. In the third case, peaks at m/z 43 and 45 could be from carbonyls, however in this case the amplitude of 43u i.e., $[\text{C}_2\text{H}_3\text{O}]^+$ must be higher than the peak at m/z 45 i.e., $[\text{C}_2\text{H}_4\text{OH}]^+$, which probably appears in the process of McLafferty rearrangement.

3.3.3.2. High mass cations

Another feature often associated to aromatic Type-2 spectra is the sequence of mass lines up-to $\sim \text{C}_{15}$. In Figure 3.17 the difference between m/z values of the consecutive peaks starting with m/z 77 is $\Delta m \sim 12-13$ indicating a highly unsaturated carbon sequence of $\text{C}/\text{H} \sim 2$, which suggests that they are fragments of a complex high mass aromatic molecule.

Figure 3.18. shows one of the possibilities to obtain un-saturated carbon periodic sequence from an aromatic compound. The impact ionization mass spectrum of polystyrene shows a dominating aromatic peak at m/z 91 (benzyl or tropylium cation). Other members of aromatic fragment series at m/z 77, 79, 65, 67, 51 and 39 are also visible. Above m/z 91, the difference between most of the consecutive mass lines is $\Delta m \sim 12-13$.

In similar hypervelocity impact ionization experiment of polypyrrole-coated polystyrene shot onto the CDA, periodic peaks were also observed above m/z 91, where each peak is separated by 12 to 14 (u) (Goldsworthy et al., 2003).

Therefore, it is plausible that CDA high mass aromatic Type-2 spectra show the presence of complex aromatic organic material in the E-ring ice grains e.g. aromatic polymer.

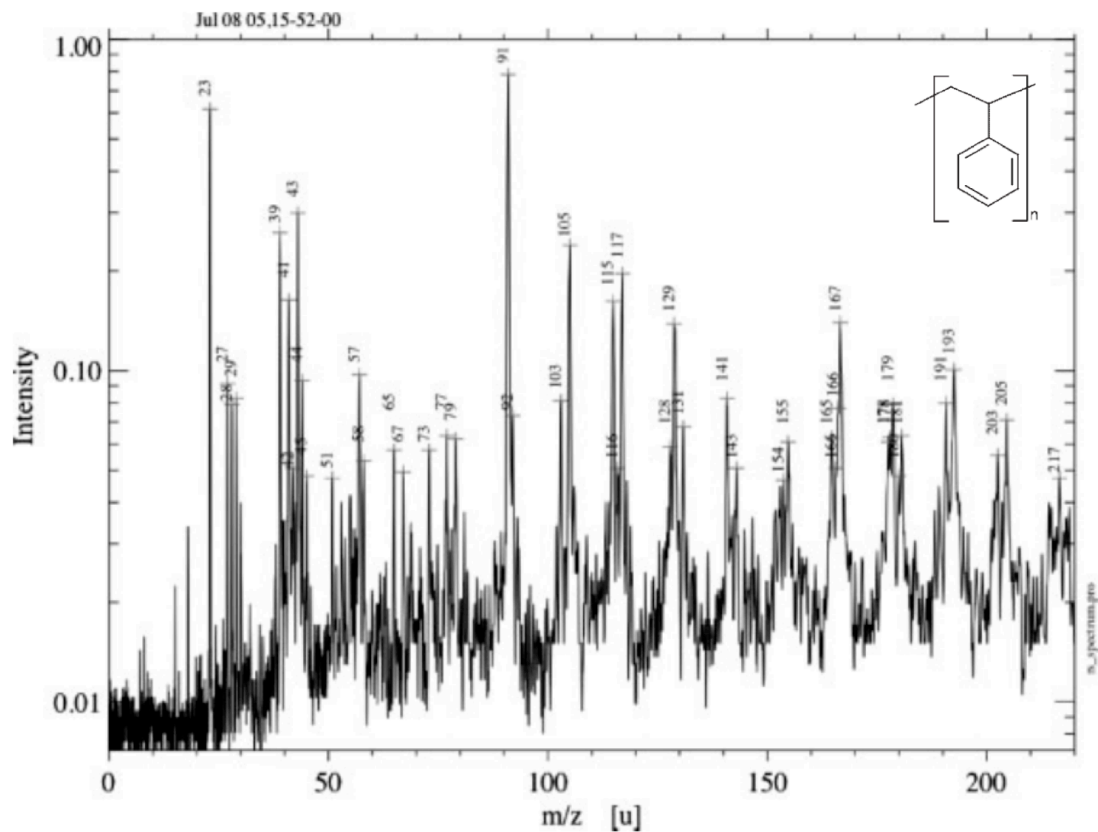


Figure 3.18 (Adapted and modified from (Srama et al., 2009)): Impact ionization cationic mass spectrum of polypyrrole-coated polystyrene latex particle ($\sim 0.6 \mu\text{m}$) that was obtained at an impact speed $\sim 5.2 \text{ km/s}$ at the 2MV Heidelberg Dust Accelerator. To accelerate the organic micro-grains in this electrostatic accelerator (Mocker et al., 2012), the particle surface must be electrically conductive and for this purpose polypyrrole-coated polystyrene particles were used.

4. Compositional mapping of the E ring in the vicinity of Rhea

4.1. Introduction

Rhea is the second largest satellite of Saturn, embedded in its diffuse E ring of icy dust particles (Figure 4.1), at an average distance of 527,040 kilometers from Saturn. The E ring extends from the orbit of Saturn's moon Mimas at $\sim 3 R_s$ (Saturn radius: $R_s = 60,268$ km) to the moon Titan at $\sim 20 R_s$. The diameter of Rhea is 1,528 kilometers. The radius of Rhea's hill sphere covers approximately the distance of ~ 7.7 times Rhea's radius (Jones et al., 2008). Inside the hill sphere Rhea's gravity dominates over Saturn's gravity.

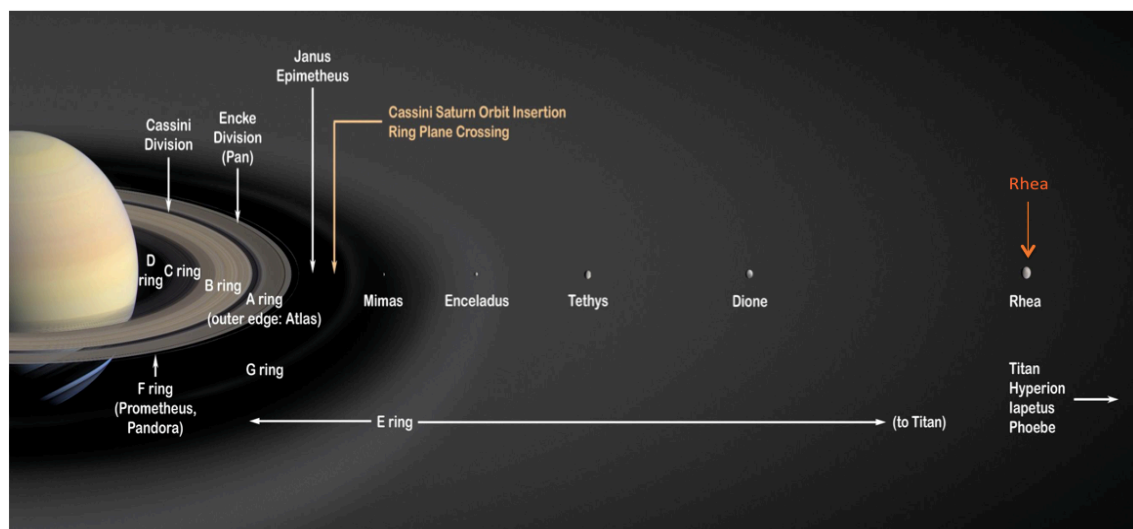


Figure 4.1 (courtesy NASA): Artistic view of Saturn and its rings and satellites. The diffuse E ring encompasses the major icy moons – from Mimas out to Titan. The embedded moon Rhea is pointed out in orange.

The Cassini spacecraft encountered Rhea on March 9, 2013 for a close flyby called 'R4'. The flyby speed was ~ 9.3 km/s and the closest approach was at ~ 997 km from Rhea's surface. On that occasion the CDA on-board Cassini sampled

the E ring environment of Rhea using its Chemical Analyzer (CA) subsystem to generate TOF mass spectra with high frequency (see section 2.2.1).

The spacecraft trajectory during the flyby was highly inclined with respect to the E ring equatorial plane; therefore the first aim of this work is to infer the vertical compositional profile of the E ring at Rhea's position. The other task is to investigate if dust particles ejected from Rhea's surface due to the bombardment of micrometeoroids can be identified. This would allow to access chemical footprints of surface material in the composition of the E ring. However, it was unclear if this footprint can be detected above to the background of E ring ice grains surrounding the moon.

4.1.1. The impactor-ejecta mechanism

In the solar system any body without an atmosphere is surrounded by clouds of dust particles, which are created by hypervelocity impacts of micrometeoroids onto the surfaces of the satellites. The steady bombardment of these interplanetary meteoroids produces ejecta dust clouds. Thus Satellites, even without any endogenic dust sources, are surrounded by micron- and submicron dust particles (Grün et al., 1985). The ejecta particles without atmospheric drag move ballistically, sometimes reaching a distance of several satellite radii (Figure 4.2).

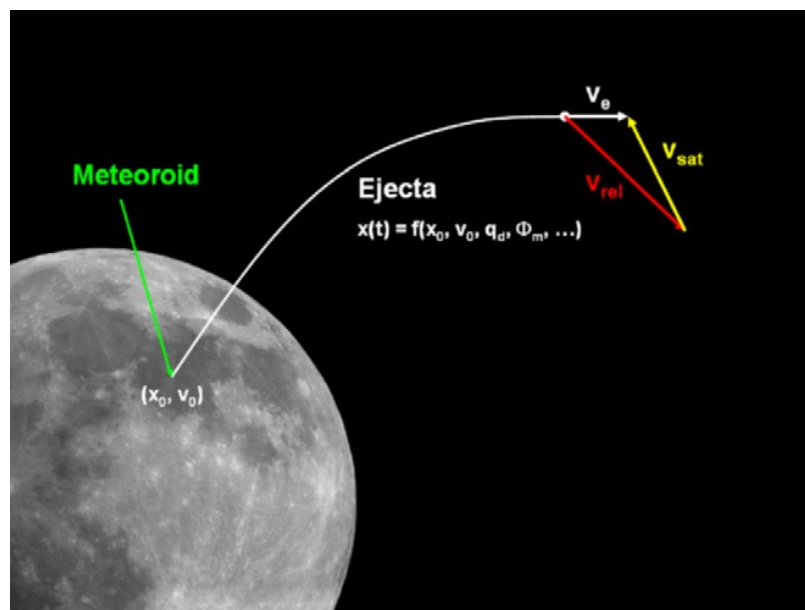


Figure 4.2 (Adapted from Postberg et al., 2011b): Schematic of the impact-ejecta mechanism. An energetic particle i.e. a micro-meteoroid hits on the surface

of a satellite with an impact velocity V_o at a position X_o . The impact creates ejecta particle, which leaves the surface at a certain velocity V_e . The compositional map of a satellite's surface can be inferred by tracking back the trajectory of the ejecta particle.

This process, called impactor-ejecta mechanism, is creating and sustaining ballistic clouds ((Krivov et al., 2003) & (Sremčević et al., 2005)), but also circumplanetary dust rings ((Hamilton & Burns, 1994) & (Showalter, 1998)). The clouds were first observed at Jupiter's Galilean moons (Krüger et al., 2003), by the dust detectors onboard Galileo (Grün et al., 1992b) but have also been found on the Earth's Moon (Horanyi et al., 2015) and have been predicted to occur on Saturn's moons as well (Spahn et al., 2006). However, the uncertainties in these models do not allow for a clear prediction if ejecta grains can be determined as a sub-population standing out from the E ring background.

4.1.2. The flyby geometry

During the R4 flyby (Figure 4.3), the Cassini spacecraft entered Rhea's hill sphere on March 9, 2013 at $\approx 18:08:00$ UTC (Coordinated Universal Time). It reached at the closest approach (CA) of 997 km from Rhea's surface at $\approx 18:17:27$ UTC ((Kriegel, 2013) & (Teolis & Waite, 2016)), crossed the equatorial plane of the E ring at $\approx 18:22:00$ UTC, and finally left the Hill sphere at $\approx 18:26:00$ UTC.

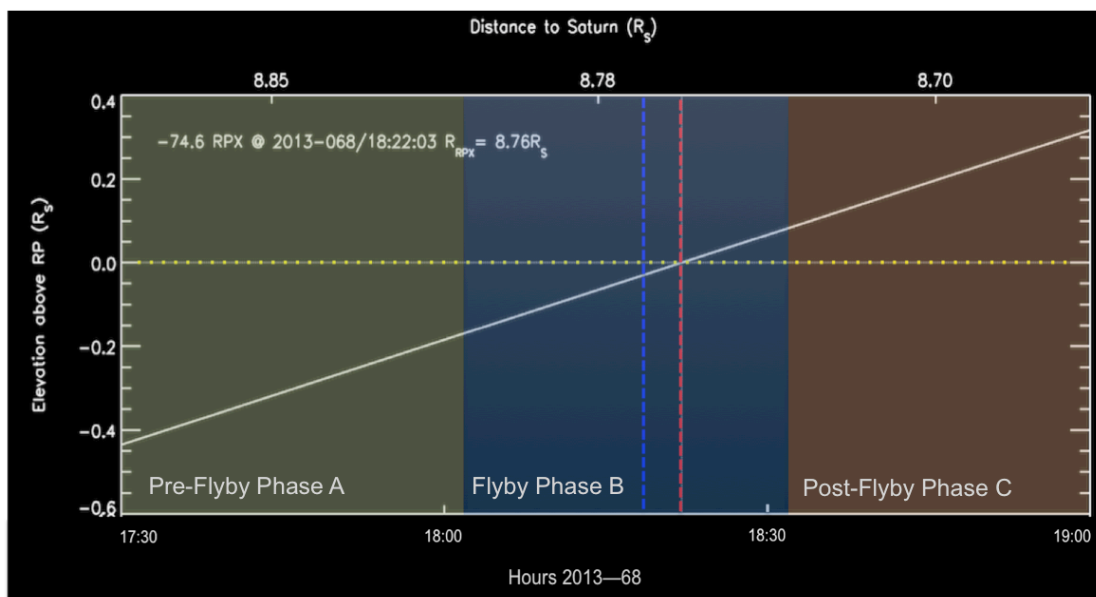


Figure 4.3: R4 Spacecraft trajectory. The lower x-axis shows the flyby time in UTC, whereas the upper axis shows distance to Saturn (R_s). The y-axis shows the elevation above the equatorial E ring plane (R_s). The yellow dotted line represents the E ring plane and the white solid line shows the spacecraft trajectory. The blue

vertical line points out the closest approach (CA) at 18:17 UTC, whereas red line shows the point at which spacecraft crossed E ring plane at 18:22 UTC. The entire flyby is divided into three phases (A, B & C) that are represented as green, blue and brown shades, respectively (for detail see table 4.1).

Table 4.1: Flyby phases. The analysis of the flyby data is divided into three phases specific to certain durations and regions in order to observe the variation in the profile pattern of the ice grains as a function of distance from Rhea's surface.

Flyby Phase	Duration (UTC)	Time from the Closest Approach-CA (minutes)	Region
A	17:30:00 18:02:00	-47 until -15 (min) before CA	South of E ring plane
B	18:02:00 18:32:00	$\approx \pm 15$ min from CA	Close to the equatorial plane of the E ring. / Inside Rhea's hill sphere ($\approx \pm 9.5$ min from CA)
C	18:32:00 19:00:00	+15 until +43 (min) from CA	North of E ring plane

4.2. Methods

Over 2000 TOF spectra were analyzed during the flyby from 17:30:00 to 19:00:00 (UTC). A spectrum analysis software is used for this work, which was developed in Interactive Data Language (IDL) by Prof. Dr. Sascha Kempf. In most cases, the spectra recording was triggered by $[\text{Na}]^+$ or $[\text{H}_3\text{O}]^+$ ions (for details of CDA spectra of ice grains see section 2.4) that resulted in the loss of cations with lower masses in the spectra. The best-fit stretch parameter "a" (see section 2.2.1.1) is set between 475 and 485 nanoseconds for this dataset. A few restrictions applied to the dataset: (i) The spectra were recorded in a compressed mode ("shrink 2") reducing the data volume of the spectra and allowed for a high transmission rate but compromised the mass resolution, (ii) The spectrum trigger threshold (QMA) was set as 12 (see section 2.2.1.1)(Srama et al., 2004), and (iii) Only peaks with the significance level 2.5σ above the noise are considered.

4.2.1. Classification of Spectra

About 93% of the total analyzed spectra (1911 out of 2050) were identified as one of the three compositional types of ice grains defined earlier by Postberg et al., 2008 & 2009a (for the detail of each type see section 2.4.1);

- Almost pure water – Type-1
- Organic enriched – Type-2
- Salt rich – Type-3

There were only 10 spectra that showed mixed characteristics of Type-1 and -3, and Type-2 and -3, which were regarded here as Type-3. The remaining 7% could not be attributed to one of the above three types that were almost uniformly distributed in all three flyby phases. Thus they do not have significance and were not considered for the compositional profile analysis. These spectra are described here briefly:

Type-?: The peak pattern of most these 47 spectra (2.3%) are water-rich spectra (Type-1 or Type-2) but their calibration was difficult due to unusual shift parameters “b” (see section 2.2.1.1) and hence the uncertain peak positions did not allow for a definite assignment to Type 1 or Type 2.

Type-5: These 50 spectra (2.4%) were triggered by the Na mass line and showed only one projectile mass line that is generally best matched with 39u (K⁺).

Type-w: These 35 spectra (1.7%) showed only three very broad peaks, which appeared as a “trident”. These broad features do not allow for an assignment to one of the three main types.

Type-x: These were 7 spectra (0,3%) that showed unique mass lines that do not fulfill the criteria of either of Type-1, Type-2, and/or Type-3.

4.2.2. Spectral count database

A count database of all spectra was prepared. The spectrum type of each impact projectile at a particular time (UTC) was counted. The database further classifies different size regimes of the detected ice grains, based on CDA’s QI signal. The QI amplitude is proportional to the number of ions produced by an impact projectile (see section 2.2.1.1), which is a function of particle’s mass and impact speed (Postberg et al., 2008). Impact speed is considered to be approximately

constant for this work. The size regimes of ice particles were defined on the basis of different ranges of their corresponding QI amplitude using the following equation (Srama, 2009).

$$\text{Log}(m_{\text{QI}}) = -4.15 + 0.558 \cdot \text{Log}(\text{QI}) - 5.59 \cdot \text{Log}(v) - 0.144 \cdot \text{Log}(v) \cdot \text{Log}(\text{QI})$$

Table 4.2: *QI amplitude ranges that are used as representations of different size regimes. The largest detected QI value (670) defines the upper boundary for the “Large” particles. QI Values below 2fC cannot be determined precisely with CDA. Therefore the lower boundary is an estimated value for 0.5fC.*

Relative size regimes	Particles' radius (µm)	QI range (fC)
Small	0.30 < r ≤ 0.38	QI ≤ 3
Intermediate	0.38 < r ≤ 0.41	3 < QI ≤ 5
Large	0.41 < r ≤ 0.81	QI > 5

The calibration equation above was determined with the CDA flight spare instrument in the dust accelerator using metallic dust grains. A calibration for ice grains is currently not available, but impact experiments onto ice targets indicate that it might be quite different from metals (Timmerman & Grün, 1991). Therefore, the sizes given in table 4.2 are only rough guidelines for the actual particle size.

A Boxcar analysis (BCA) (see section 2.5) was performed to analyze the compositional profile of the E ring grains during the flyby.

4.3. Results

The spectral analysis showed no unusual types of ice grains that pointed to the particles from Rhea's surface of specific composition. The few spectra that are not classified as one of the three main types (see section 4.2.1) did not show an increased abundance close to Rhea.

The rate of the registered impact events of ice particles that produced spectra does increase slightly along the spacecraft trajectory (Figure 4.4). This is expected because the E ring becomes denser closer to its main source Enceladus situated at 3.95 Rs. However, when the spacecraft approached the equatorial plane of the E ring, inside Rhea's hill sphere (Figure 4.3), a plateau is observed with a maximum around the closest approach from the surface of Rhea (Figure 4.4: spectral counts/10min).

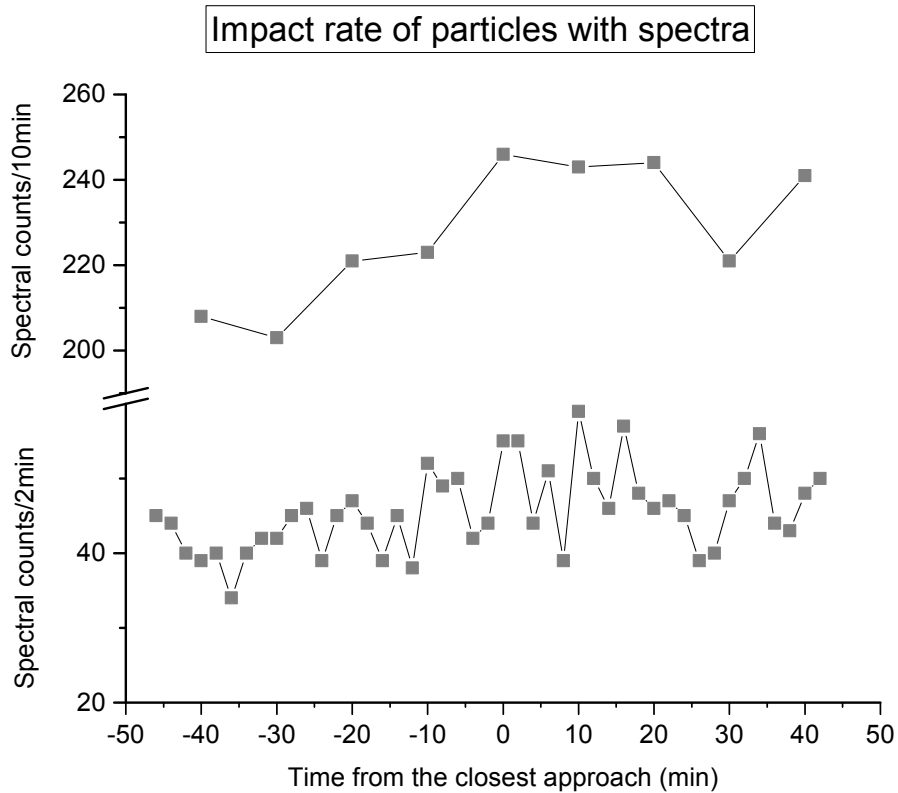


Figure 4.4: *Spectral counts rate along the spacecraft trajectory. Spectral counts per 2 minutes (bottom). Spectral counts per 10 minutes (top). The increase in counts around the closest approach is more obvious in 10 minutes rate plot.*

4.3.1. Compositional profiles

The compositional profile of E ring ice particles is plotted over time along the spacecraft trajectory (Figure 4.5). Overall the compositional profiles are almost featureless. The proportion of Type-1 ice grains dominates over Type-2 and Type-3 ice grains along the entire flyby. A minimum of weak significance in the proportion of Type-1 is observed around the closest approach, whereas the fraction of Type-2 grains is slightly increased at the same time. The proportion of salt rich Type-3 grains shows a weakly significant minimum during flyby phase B.

The overall compositional profile of E ring ice grains show no pronounced change in their proportions along the spacecraft trajectory. To investigate a size dependent compositional profile, the population of each type of ice grains is divided into different size regimes (see next section: 4.3.1.1).

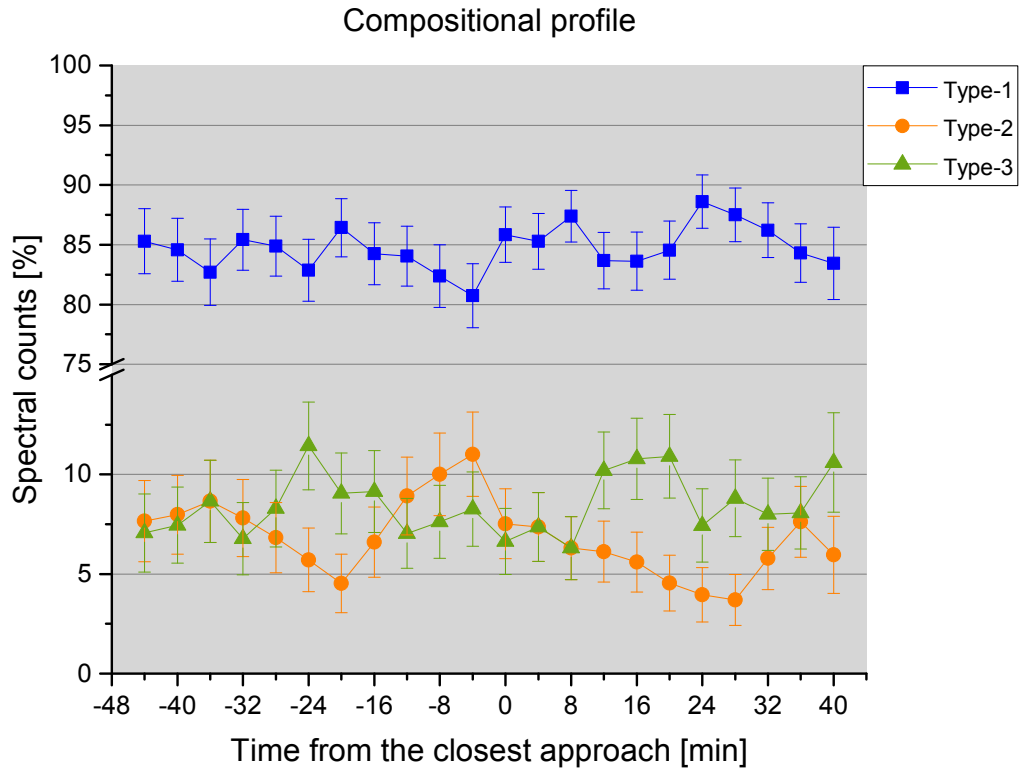


Figure 4.5: Boxcar plot (box size: 10 minutes; step size: 4 minutes) of the compositional profile. Populations of three types of ice grains (Type-1, Type-2 and Type-3) are plotted along the spacecraft trajectory across the closest approach from the surface of Rhea. Error bars, standard error of the mean (SEM), are derived as $SEM = \sqrt{p(1-p)/N}$. Here, p is the proportion of the particles of a spectrum type and N is the total number of particles of all spectrum types during a particular time interval (box size). The few spectra that are not classified as one of these three main types (see section 4.2.1) are not shown, but their frequency is evenly distributed all along the flyby and does not show clustering at any location.

4.3.1.1. Size dependent compositional profile

As described earlier (see section 4.2.2), the QI amplitude can be used to estimate the size of the particles; figure 4.6 compares proportions of the three types of ice particles in each size regime during each flyby phase. The results are summarized in table 4.3.

Table 4.3: Summary of the compositional profiles of different size regimes of ice grains. The table shows (%) proportions and their corresponding error bars of: (i) all sized particles corresponding to all QI values (ii) relatively small sized particles correspond to $QI \leq 3$ fC (iii) relatively intermediate sized particles correspond to $3 < QI \leq 5$ fC and (iv) relatively large sized particles correspond to $QI \geq 5$ fC.

Particle's size regimes	All sized particles (All QI values)			Relatively small particles $QI \leq 3$ (fC)			Relatively intermediate particles $3 < QI \leq 5$ (fC)			Relatively large particles $QI > 5$ (fC)		
	Spectra	626	669	616	375	413	341	136	157	158	115	99
Flyby phase	A	B	C	A	B	C	A	B	C	A	B	C
(%)												
Type-1	84.6 ±1.4	84.7 ±1.3	85.2 ±1.4	97.0 ±0.8	93.7 ±1.1	95.3 ±1.1	87.5 ±2.8	84.7 ±2.8	88.6 ±2.5	40.8 ±4.5	47.4 ±5.0	51.2 ±4.6
Type-2	6.8 ±1.0	8.0 ±1.0	5.3 ±0.9	1.6 ±0.6	3.3 ±0.8	2.3 ±0.8	7.3 ±2.2	10.8 ±2.4	6.3 ±1.9	23.4 ±3.9	23.2 ±4.2	12.8 ±3.0
Type-3	8.4 ±1.1	7.1 ±0.9	9.4 ±1.1	1.3 ±0.5	2.9 ±0.8	2.3 ±0.8	5.1 ±1.8	4.4 ±1.6	5.0 ±1.7	35.6 ±4.4	29.2 ±4.5	35.8 ±4.4

Type-1: During each flyby phase (A, B, C) Type-1 particles in all the three size regimes dominate over the entire population of E ring ice grains. The proportion of Type-1 particles is highest for small sizes ($\approx 95\%$) and lowest for large sizes ($\approx 50\%$) (Figures 4.6 & 4.7). In small and intermediate size regimes, the proportions of Type-1 particles show a weakly significant decrease during flyby phase-B close to the equatorial plane. In the larger size regime the proportions of these particles increase gradually as spacecraft moves to the inner E ring from phase A to C.

Type-2: The proportion of small sized Type-2 particles ($\approx 2.5\%$) is much lower as compared to intermediate ($\approx 8\%$) and large sized particles ($\approx 20\%$) (Figure 4.7). The proportion during flyby Phase-B is slightly increased for small and intermediate sizes, whereas for large size Type-2 particles it decreased sharply in phase-C.

Type-3: The proportion of Type-3 particles consecutively and dramatically increases as the size of the particles increases: from $\approx 3\%$ for small grains to $\approx 33\%$ for the large grains (Figure 4.7). For small and intermediate size regimes, the proportions of Type-3 particles remain unchanged during the entire flyby but show a slight decrease in phase-B for large size regime.

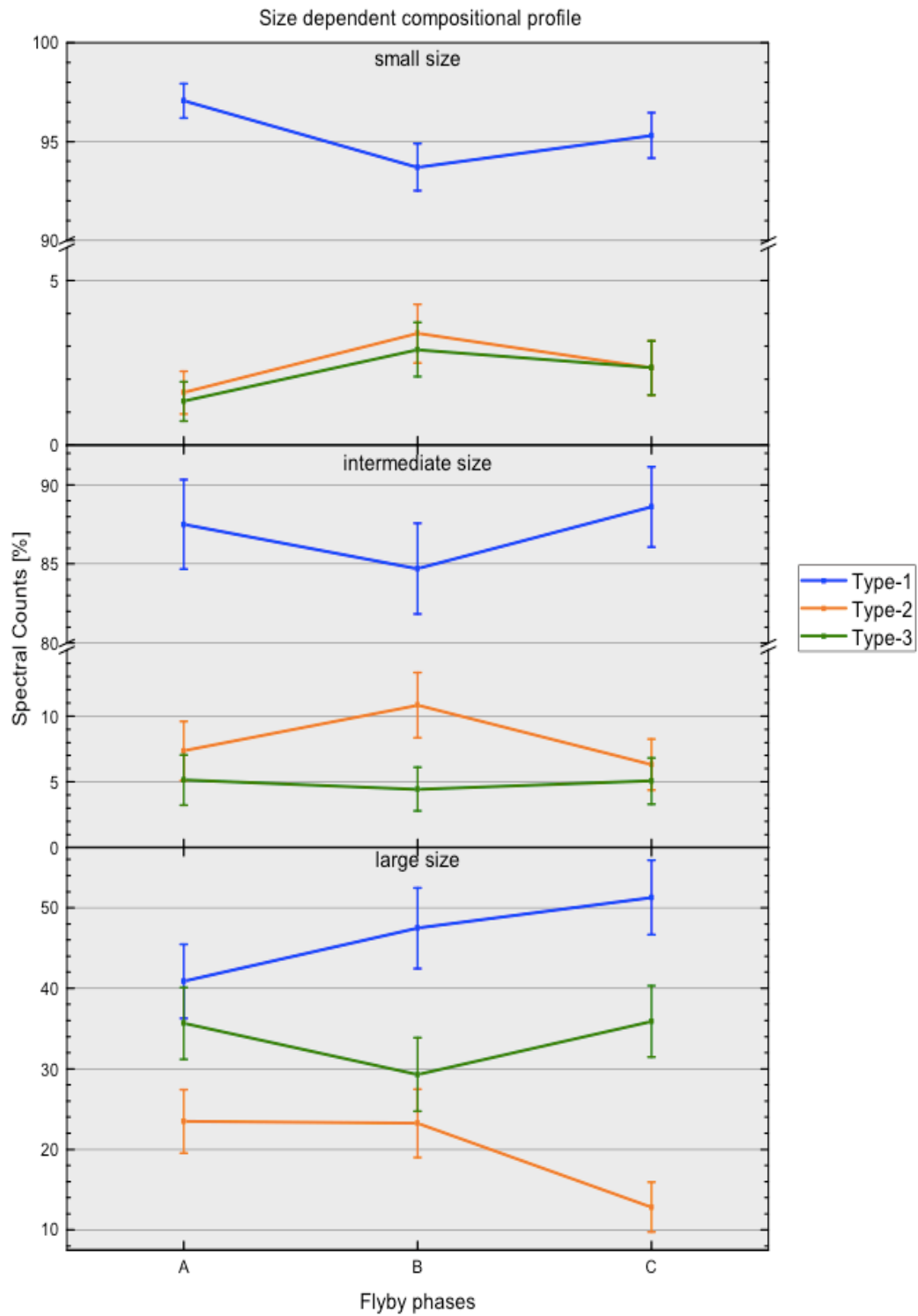


Figure 4.6: Size dependent compositional profile. The y-axis shows the proportion of spectral counts. (Top) small sized particles (Middle) intermediate sized particles and (Bottom) large sized particles. The x-axis shows the three flyby phases (see table 4.1).

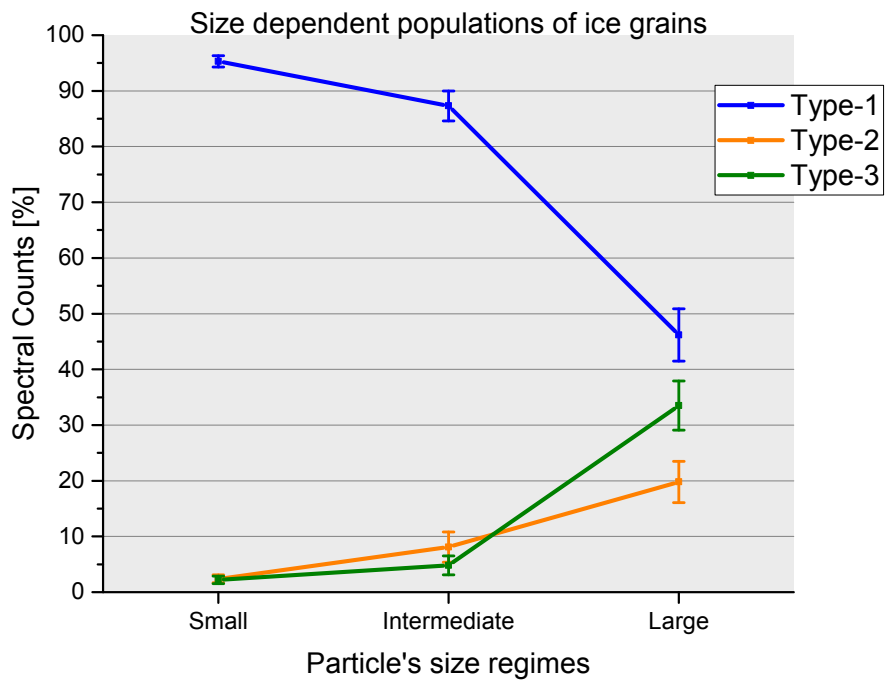


Figure 4.7: Proportions of spectral counts of each type of ice grains in three size regimes independent of flyby phases. A substantial increase in the proportion of Type-2 and Type-3 particles is observed in the large size regimes, whereas the fraction of Type-1 particles drops dramatically.

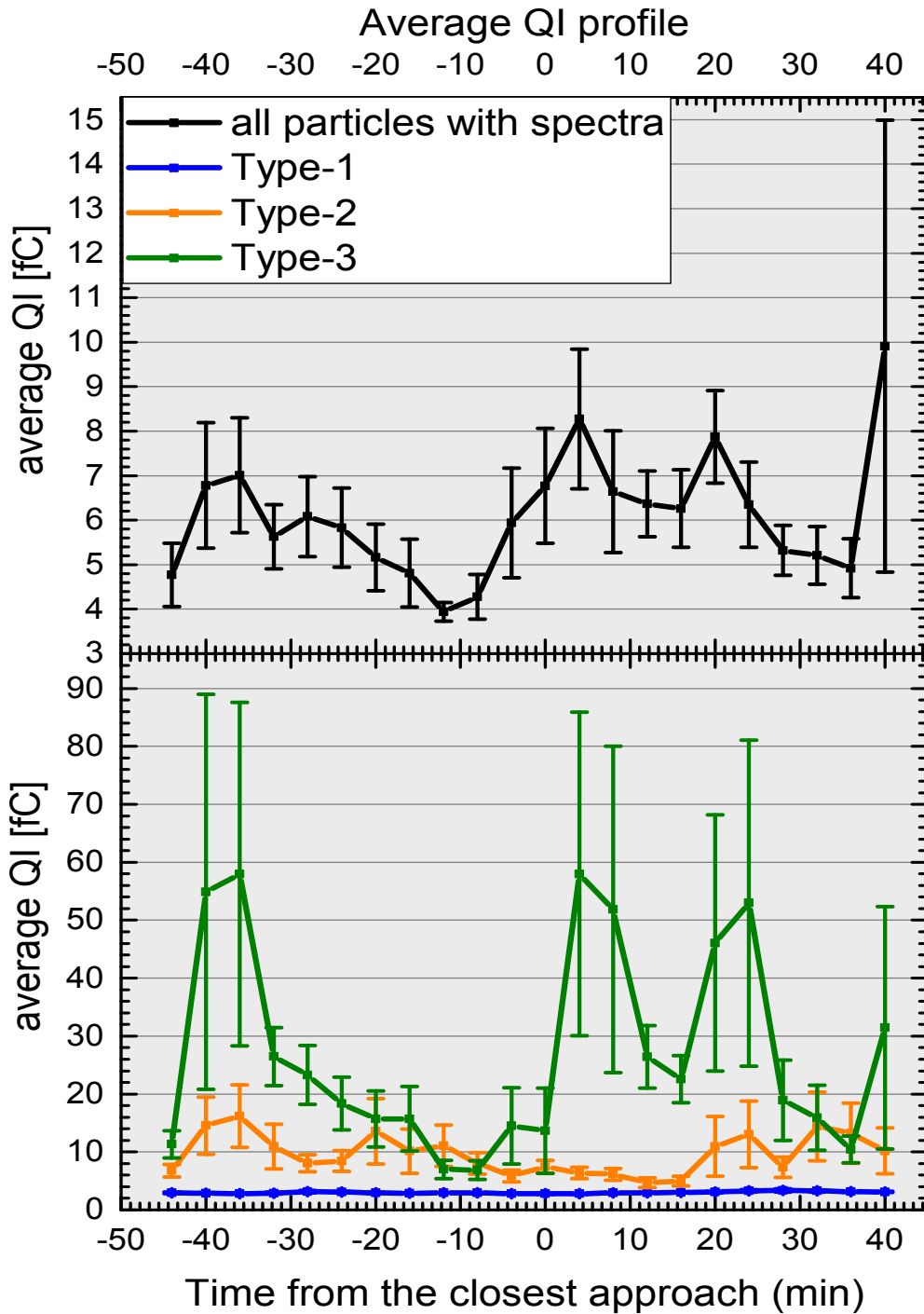


Figure 4.8: Boxcar plot (box size: 10 minutes & step size: 4 minutes) of the average ion yield (QI) profile along the spacecraft trajectory. (top) Ion yield for all ice particles. (bottom) Average ion yield for each of the three types of ice particles. As expected from Figure 4.7, the ion yield of Type-3 impacts is larger, whereas as of Type-2 is intermediate. The significant increase in the average QI of Type-3 in some cases is due to a few outliers with extremely high QI values (Figure 4.9).

There is a minimum average ion yield (QI) just before the closest approach from Rhea's surface, which increases after the closest approach. In the bottom figure 4.8, Type-3 particles show the highest average ion yield amongst the three types whereas Type-1 show the least average ion yield during the entire flyby and Type-2 particles show an intermediate ion yield.

The ion yield of Type-3 particles follows the average ion yield along the flyby. Thus, the overall QI profile (Figure 4.8 top) is largely governed by Type-3 particles (Figure 4.8 bottom). The large error bars in many Type-3 values (Figure 4.8 bottom) are due to outliers of a few very large individual Type 3 particles, as illustrated in figure below (Figure 4.9).

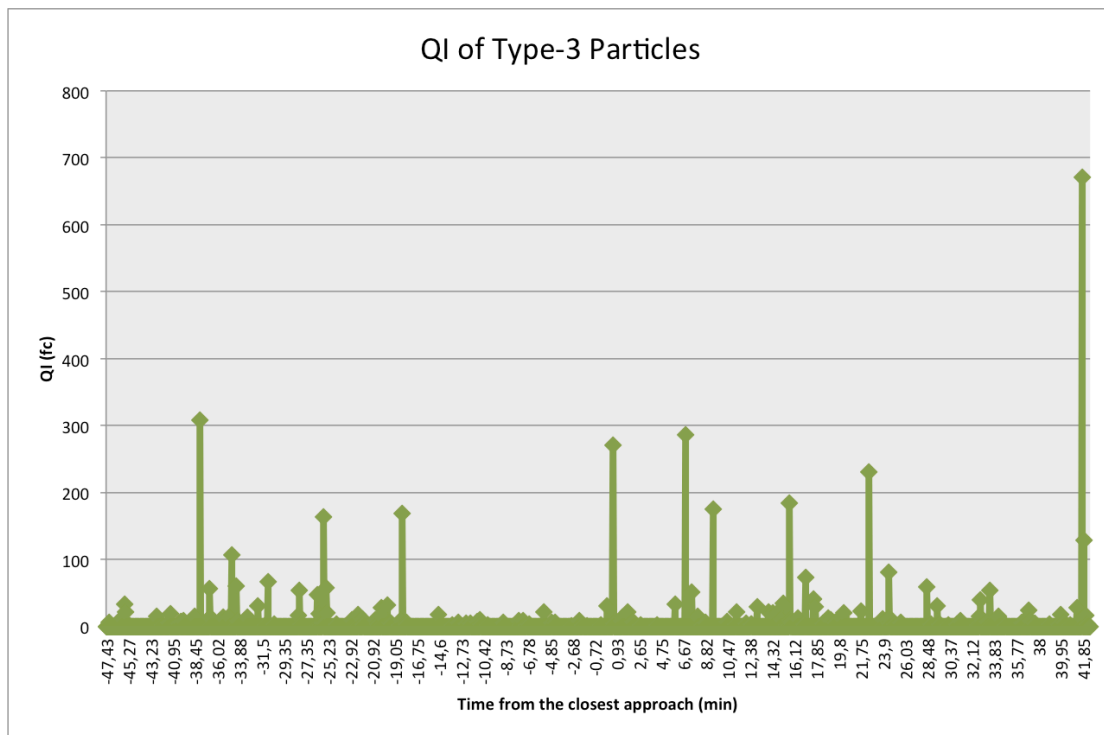


Figure 4.9: Shown is the QI amplitude of all Type-3 particles detected along the spacecraft trajectory. The x-axis shows the time in minutes from the closest approach when Type-3 spectrum was recorded and the y-axis represents related QI amplitude in absolute abundance.

4.4. Discussion and conclusion

The flyby (R4) results showed the same compositional types (Type-1, Type-2, Type-3) of E ring ice grains as were observed in previous work (Postberg et al., 2008, 2009a & 2011a).

The overall compositional profile (Figure 4.5) shows no striking change in the proportion of each type of ice grains during the entire flyby. However, in phase-B Type-2 particles of small sizes ($\leq 5\text{fC}$ ion yield) showed a slight increase in their proportion, whereas the proportion of Type-1 grains dropped slightly. This indicates that the number of organic bearing grains (Type-2) are increased by either a) particles from Rhea's surface, or b) particles with low inclination that preferably reside in the equatorial plane. For the flyby geometry investigated here, these two options cannot be distinguished from each other.

No unusual chemistry of particles was found in the vicinity of Rhea as compared with the E ring background. This implies that either the composition of Rhea's surface is similar to the E ring particles or Rhea's surface material is not contributing to the E ring composition even within its Hill sphere. However, the impact rate reaches a maximum (higher number density) inside Rhea's hill sphere that might indicate the presence of an ejecta cloud of particles with a composition that is not distinguishable from the E ring background. This is actually quite plausible because recent observation from the CIRS instrument of Cassini have shown that the moon is probably coated at least a meter of E ring "snow" (Howett et al., 2016). An alternative explanation for the higher detection rate might be that gravitational focussing of E ring grains by Rhea's gravity led to an increased detection of small particles.

Although a constant impact speed (9.3 km/s) was assumed for the whole flyby, in fact the impact speed changed slightly from 9.19 km/s at 17:30 to 9.32 km/s at 19:30. This theoretically leads to a systematic increase of the ion yield for identical grains of about 10%. However, this systematic change cannot be observed because it is small compared to the large ion yield fluctuations, probably due to changing grain sizes, along the flight path (Figure 4.8).

The average relative abundances of the three compositional types of this work are Type-1 $\approx 85\%$, Type-2 $\approx 7\%$, and Type-3 $\approx 8\%$. However, as observed in the previous analysis, the abundances (Figure 4.6) of compositional types showed

remarkable changes in their relative abundances. Gradually with the increase of the particle's size, Type-1 became less abundant (95% → 45%), whereas organic enriched (Type-2) and salt rich particles (Type-3) became relatively more abundant (3% → 20% and 3% → 33%, respectively) (Figure 4.7 & Table 4.3). In conclusion, Type-1 particles are generally of the smallest size mostly below about 0.5 μm in radius. Type-2 and specifically Type-3 particles are more abundant at larger sizes mostly above ≈ 0.5 μm in radius, which is in good agreement with previous results (Postberg et al., 2011a).

However, especially the proportions of Type 1 and 2 are different from the earlier results. Postberg et al., 2008 reported Type 1 and Type 2 grains in similar abundances. However there are several caveats. The analysis of Type 3 spectra was not included in Postberg et al. 2008. Moreover, spectrum recording there was triggered by particle impact, whereas on R4 it was triggered by mass line (H_3O^+ or Na^+), which reduced the probability to detect Type 2 spectra (Postberg et al. 2008) (for details about Type-2 spectral features see section 2.4.1). Furthermore, the relative impact speeds of the projectiles (ice grains) and their positions in E ring were also not mentioned. Therefore, abundances of different types, in the current work, are not comparable with Postberg et al., 2008.

In another E ring study (Postberg et al., 2009a) the proportions of Type-2 and -3 were ≈ 20% and ≈ 6-7%, respectively, whereas in this current work Type-2 is ≈ 7% and Type 3 is ≈ 8%. However, the proportion of ≈20 % Type-2 is in good agreement with the Type-2 proportion of large particles ($\geq 5\text{fc}$) measured in the current work (Figure 4.7). Although the average Type-3 proportion of 8% (Figure 4.5) of this work is in good agreement with Postberg et al., 2009a, the value for large particles ($\geq 5\text{fC}$) is much higher (≈ 33%, Figure 4.7).

In another data set obtained on the Cassini's flyby of Enceladus (E5) in 2008 Type-3 proportion was ≈ 10% in the E ring background (Postberg et al., 2011a), which is again in good agreement with the average Type- 3 proportion (Figure 4.5) on R4. Type-2, however, was significantly higher (≈ 30%) as compared even to the 20% in this work for large ion yields (Figure 4.7). However on E5 the flyby speed (≈ 17.7 km/s) was much higher and the instrument (CDA) was in saturation throughout the flyby (10 - 1000 impacts/sec). In addition, the instrument (CDA) was specifically configured for E5 with specific version of flight software.

In general a comparison of current abundances with previous findings is difficult. The differences in relative speed and position of the spacecraft in E ring seem to play an important role on the ice particles' abundances and therefore need to be considered for a detailed comparative study between flybys. Another important factor is the settings of instrument, in particular the trigger mechanism (impact or ion)(Srama et al., 2004)(see section 2.2.1.1) and the respective trigger thresholds for spectrum recording. Therefore, more elaborative comparative approaches are needed and comparison based only on ion yields is not feasible. All this was beyond the scope of this work.

As a result of this study R4 data set will be part of a comparative E ring analysis of wider scope in the near future. In this follow-up project, the abundances of the different compositional types will be monitored over a wide range of both, impact speeds and positions in the E ring and instrument settings will be considered.

5. Summary

This dissertation is comprised of two projects that are independently presented and discussed in chapter 3 and 4. In both projects, in situ analysis of ice grains in Saturn's E ring was performed to infer their composition and the proportions of different compositional types. This compositional data was obtained from the Cosmic Dust Analyzer (CDA) onboard the Cassini spacecraft. The Chemical Analyzer (CA) subsystem of CDA generated in-situ impact ionization cationic ToF mass spectra from individual impinging ice grains onto the instrument's target plate.

The aim of the first project is to use a novel analogue experiment for an in-depth compositional analysis of organic material in the ice grains ejected from the subsurface ocean of the moon Enceladus. The aim of the second project is to infer the compositional profile of E-ring ice grains in the vicinity of the moon Rhea and the influence of Rhea on this compositional profile.

Project-1:

729 organic ice grain spectra with organic mass lines (known as Type-2) recorded between 2004 and 2009 in Saturn's E ring were used for this analysis. Out of these, 320 spectra showed apparent characteristic signatures that could be associated with characteristic signatures from different compositional families of organic compounds. Laser-assisted laboratory analogue experiments with organic materials in a water matrix were carried out to simulate these signatures in CDA spectra. Various combinations of laser intensities and delay times were used to mimic the different CDA impact energies and to understand the varying cationic organic fragmentation patterns.

The main results are:

- Signatures of three fundamental families of organic compounds were identified in CDA Type-2 spectra. (i) Amine, (ii) Carbonyl and (iii) Aromatic. Furthermore, complex organic material with molecular masses in excess of 200u was observed associated with some of the aromatic spectra. These findings give insight into a largely varying and complex organic chemistry inside Enceladus.
- Amine: Can be identified by a distinct mass line at m/z 18 of ammonium cations $[\text{NH}_4]^+$. At least in 50% of amine spectra, ammonia cations form water cluster ($[\text{NH}_4]^+(\text{H}_2\text{O})_{1,2}$) at m/z 36 and 54 that can be used as supporting evidence.
- Carbonyl: Can be identified by a highly distinct cationic fragment at m/z 43, which corresponds to the acylium cation $[\text{C}_2\text{H}_3\text{O}]^+$. $[\text{CH}_2\text{OH}]^+$ (m/z 31) can be used as supporting evidence.
- Aromatic: Can be identified by a series of characteristic unsaturated cationic fragments ($[\text{C}_3\text{H}_x]^+$, $[\text{C}_4\text{H}_x]^+$, $[\text{C}_5\text{H}_x]^+$, $[\text{C}_6\text{H}_x]^+$, $[\text{C}_7\text{H}_x]^+$). The relative amplitudes of Phenyl $[\text{C}_6\text{H}_x]^+$ and Tropylium cations $[\text{C}_7\text{H}_x]^+$ imply that different aromatic structures must be conjointly present in these ice grains from Enceladus.
- Complex organics: Some spectra of the aromatic family (~ 37 %) show a sub-type with a periodic sequence of highly unsaturated fragments ($\Delta m \sim 11-13$) above 90u that extends over the entire mass range recorded by CDA ($\approx 200\text{u}$). These features are probably the breakup from much larger complex aromatic species with masses clearly above 200u.
- ≈ 11 % of the 320 spectra with the characteristic described above, showed signatures of more than one of the three identified organic families in a single ice grain.
- More, yet un-specified organic signatures in Type-2 were also observed. However, their characterization requires further investigation.

Project-2:

A Cassini flyby of Rhea, a moon embedded in the E ring, in 2013 was used for statistical analysis of three known different compositional types of the ice grains along the flight path. These types are organic-bearing (Type-2 as mentioned above), salt-rich (Type-3) and almost pure-water (Type-1) ice grains. A Boxcar Analysis (BCA) was performed, where relative proportions of these spectral Types were plotted as the compositional profile of the E ring along the flight path of the spacecraft.

The main results are:

- During the flyby no ice grains of unusual composition were observed that could be attributed exclusively to Rhea's surface. It is concluded that either the composition of particles lifted from Rhea surface is similar to the E-ring background or the geometry of the flyby did not allow observing the ejecta particles from the surface of Rhea.
- The overall detection rate slightly increased in the equatorial plane that almost coincided with Rhea's Hill sphere in the given flyby geometry. This might indicate the presence of an ejecta cloud of particles with a composition that is not distinguishable from the E ring background. That would actually quite plausible because the moon is probably coated by deposition of E ring "snow". An alternative explanation for the higher detection rate might be a general higher number density of grains in the equatorial plane (Kempf et al., 2008) or gravitational focussing of E ring grains by Rhea's gravity.
- Although overall variations in proportions of the three compositional types are very subtle along the flight path, the abundance of Type-1 showed a slight decrease in their proportions of small particles ($\leq 5\mu\text{m}$ ion yield) near Rhea, whereas the proportion of Type-2 grains increased slightly. This indicates that the number of organic bearing grains (Type-2) are increased by either a) particles from Rhea's surface, or b) particles with low inclination that preferably reside in the equatorial plane.

- The proportions of the observed compositional types vary greatly with particle size as described in the following:
 - Type-1 (pure water ice): The average relative proportion observed was ~85 (%), whereas previously it was reported as ~ 73 % (Postberg et al., 2009a) and ~ 60 % (Postberg et al., 2011a). These particles are generally of the smallest size, with radii mostly below about 0.5 μm . With the increase of particles' sizes Type-1 became less abundant (95% \rightarrow 45%).
 - Type-2 (organic-enriched): The average relative abundance observed was ~ 7 %, whereas in previous studies it was as ~ 20 % (Postberg et al., 2009a) and ~ 30 % (Postberg et al., 2011a). In contrast to Type-1, the organic enriched type became relatively more abundant (3% \rightarrow 20%) with the increase in particles' sizes. Thus, the previously reported abundance (20% in Postberg et al., 2009a) of Type-2 particles is in good agreement with the proportion of large Type-2 particles in this work.
 - Type-3 (salt-rich): The average relative proportion observed was ~ 8 %. Previous studies reported ~ 6-7 (%) (Postberg et al., 2009a) and ~ 10 % (Postberg et al., 2011a), which was in good agreement. Remarkably, this work showed a tremendous increase in the abundance of Type-3 (3% \rightarrow 33%) with the increase in particles' sizes. Generally grains with radii larger than 0.5 μm show the highest Type-3 proportion, which is in very good agreement with Postberg et al. 2011a.

References

- Altobelli, N., Postberg, F., Fiege, K., Trieloff, M., Kimura, H., Sterken, V. J., ... Gruen, E. (2016). Flux and composition of interstellar dust at Saturn from Cassini's Cosmic Dust Analyzer. *Science (New York, N.Y.)*, 352(6283), 312–8. <http://doi.org/10.1126/science.aac6397>
- Amari, S., & Lodders, K. (2007). Pre-solar grains from supernovae and novae. *Highlights of Astronomy*, 14, 349–352.
- Auer, S., & Sitte, K. (1968). Detection technique for micrometeoroids using impact ionization. *Earth and Planetary Science Letters*, 4, 178–183.
- Austin, D. E. (2003). *Impact-ionization mass spectrometry of cosmic dust (PhD Thesis)*. California Institute of Technology, Pasadena, California. <http://doi.org/CaltechETD:etd-11072002-135150>
- Baum, W. A., Kreidl, T., Westphal, J. A., Danielson, G. E., Seidelmann, P. K., Pascu, D., & Currie, D. G. (1981). Saturn's E ring. I. CCD observations of March 1980. *Icarus*, 47(1), 84–96. [http://doi.org/10.1016/0019-1035\(81\)90093-2](http://doi.org/10.1016/0019-1035(81)90093-2)
- Beinsen, A. (2011). *Bildgebung und chemische Analytik mit Laserdesorptions-Massenspektrometrie im Bereich Forensik und Astrophysik (PhD Thesis)*. Georg-August-Universität Göttingen, Germany.
- Binney, J., & Merrifield, M. (1998). *Galactic astronomy*. Princeton University Press. New Jersey.
- Cadek, O., Tobie, G., Van Hoolst, T., Masse, M., Choblet, G., Lefevre, A., ... Trinh, A. (2016). Enceladus' s internal ocean and ice shell constrained from Cassini gravity, shape and libration data. *Geophysical Research Letters*, 43(May), 5653–5660. <http://doi.org/10.1002/2016GL068634>
- Cameron, A. E., & Eggers, D. F. (1948). An ion "velocitron." *Review of Scientific Instruments*, 19(9), 605–607. <http://doi.org/10.1063/1.1741336>
- Charvat, A., & Abel, B. (2007). How to make big molecules fly out of liquid water: applications, features and physics of laser assisted liquid phase dispersion mass spectrometry. *Physical Chemistry Chemical Physics : PCCP*, 9(26), 3335–60. <http://doi.org/10.1039/b615114k>
- Charvat, A., Lugovoj, E., Faubel, M., & Abel, B. (2004). New design for a time-of-flight mass spectrometer with a liquid beam laser desorption ion source for the analysis of biomolecules. *Review of Scientific Instruments*, 75(5 PART 1), 1209–1218. <http://doi.org/10.1063/1.1710704>
- Collins, G. C., & Goodman, J. C. (2007). Enceladus' south polar sea. *Icarus*, 189(1), 72–82. <http://doi.org/10.1016/j.icarus.2007.01.010>
- Cotter, R. J. (1997). *Time-of-Flight Mass Spectrometry: Instrumentation and Applications in Biological Research (ACS Professional Reference Book)*. American Chemical Society.
- Courtin, R., Gautier, D., Marten, A., Bezard, B., & Hanel, R. (1984). The composition of Saturn's atmosphere at northern temperate latitudes from Voyager IRIS spectra - NH₃, PH₃, C₂H₂, C₂H₆, CH₃D, CH₄, and the Saturnian D/H isotopic ratio. *Astrophysical Journal*, 287, 899–916.
- de Pater, I., Martin, S. C., & Showalter, M. R. (2004). Keck near-infrared observations of Saturn's E and G rings during Earth's ring plane crossing in

- August 1995. *Icarus*, 172(2), 446–454.
<http://doi.org/10.1016/j.icarus.2004.07.012>
- Dorschner, J., & Henning, T. (1995). Dust metamorphosis in the galaxy. *The Astronomy and Astrophysics Review*, 6(4), 271–333.
<http://doi.org/10.1007/BF00873686>
- Dougherty, M. K., Khurana, K. K., Neubauer, F. M., Russell, C. T., Saur, J., Leisner, J. S., & Burton, M. E. (2006). Identification of a dynamic atmosphere at Enceladus with the Cassini magnetometer. *Science (New York, N.Y.)*, 311(March), 1406–1409. <http://doi.org/10.1126/science.1120985>
- Fiege, K. (2013). *Compositional Analysis of Interstellar Dust as seen by the Cassini Cosmic Dust Analyzer (PhD Thesis)*. The Ruperto-Carola Heidelberg University, Germany.
- Friichtenicht, J. F. (1964). Micrometeoroid simulation using nuclear accelerator techniques. *Nuclear Instruments and Methods*, 28(1), 70–78.
[http://doi.org/10.1016/0029-554X\(64\)90351-9](http://doi.org/10.1016/0029-554X(64)90351-9)
- Friichtenicht, J. F., Roy, N. L., & Moede, L. W. (1971). *Cosmic Dust Analyzer*. Technical Report NASA-CR-140241.
- Gebhardt, C. R., Schröder, H., & Kompa, K.-L. (1999). Surface impact ionization of polar-molecule clusters through pickup of alkali atoms. *Nature*, 400(5 August 1999), 544–547. <http://doi.org/10.1038/22984>
- Godfrey, D. A. (1988). A hexagonal feature around Saturn's north pole. *Icarus*, 76(2), 335–356. [http://doi.org/10.1016/0019-1035\(88\)90075-9](http://doi.org/10.1016/0019-1035(88)90075-9)
- Goldsworthy, B. J., Burchell, M. J., Cole, M. J., Armes, S. P., Khan, M. A., Lascelles, S. F., ... Bigger, S. W. (2003). Time of flight mass spectra of ions in plasmas produced by hypervelocity impacts of organic and mineralogical microparticles on a cosmic dust analyser. *A & A*, 409, 1151–1167.
<http://doi.org/10.1051/0004-6361:20031087>
- Greenberg, J. M., & Caro, G. M. M. (2000). Organics in space: from interstellar dust to comets (Vol. 197, pp. 331–342). Symposium - International Astronomical Union. <http://doi.org/http://dx.doi.org/10.1017/S0074180900164915>
- Grün, E., Fechtig, H., Hanner, M. S., Kissel, J., Lindblad, B. A., Linkert, D., ... Zook, H. A. (1992b). The Galileo Dust Detector. *Space Science Reviews*, 60(1–4), 317–340. <http://doi.org/10.1007/BF00216860>
- Grün, E., Fechtig, H., Kissel, J., Linkert, D., Maas, D., McDonnell, J., ... Giese, R. (1992a). The Ulysses dust experiment. *Astronomy and Astrophysics Supplement Series*, 92(2), 411–423. Retrieved from <http://adsabs.harvard.edu/full/1992A&AS...92..411G>
- Grün, E., Gustafson, B., Mann, I., Baguhl, M., Morfill, G. E., Staubach, P., ... Zook, H. A. (1994). Interstellar dust in the heliosphere. *Astron. Astrophys.*, 286, 915–924. Retrieved from <http://adsabs.harvard.edu/abs/1994A%26A...286..915G>
- Grün, E., Landgraf, M., Horányi, M., Kissel, J., Krüger, H., Srama, R., ... Withnell, P. (2000). Techniques for galactic dust measurements in the heliosphere. *Journal of Geophysical Research*, 105(A5), 10403–10410.
<http://doi.org/10.1029/1999JA900376>
- Grün, E., Pailer, N., Fechtig, H., & Kissel, J. (1980). Orbital and physical characteristics of micrometeoroids in the inner solar system as observed by Helios 1. *Planetary and Space Science*, 28(3), 333–349.
[http://doi.org/10.1016/0032-0633\(80\)90022-7](http://doi.org/10.1016/0032-0633(80)90022-7)

- Grün, E., Zook, H. A., Fechtig, H., & Giese, R. H. (1985). Collisional balance of the meteoritic complex. *Icarus*, 62(2), 244–272. [http://doi.org/10.1016/0019-1035\(85\)90121-6](http://doi.org/10.1016/0019-1035(85)90121-6)
- Guilhaus, M. (1995). Principles and instrumentation in time-of-flight mass spectrometry: Physical and instrumental concepts. *Journal of Mass Spectrometry*, 30(11), 1519–1532. <http://doi.org/10.1002/jms.1190301102>
- Hamilton, D., & Burns, J. (1994). Origin of Saturn's E ring: Self-sustained, naturally. *Science*, 264(5158), 550–553. <http://doi.org/10.1126/science.264.5158.550>
- Hansen, C. J., Esposito, L., Stewart, A. I. F., Colwell, J., Hendrix, A. R., Pryor, W. R., ... West, R. (2006). Enceladus' water vapor plume. *Science (New York, N.Y.)*, 311(March), 1422–1425. <http://doi.org/10.1126/science.1121254>
- Hillier, J. K., Green, S. F., McBride, N., Altobelli, N., Postberg, F., Kempf, S., ... Grün, E. (2007a). Interplanetary dust detected by the Cassini CDA Chemical Analyser. *Icarus*, 190(2), 643–654. <http://doi.org/10.1016/j.icarus.2007.03.024>
- Hillier, J. K., Green, S. F., McBride, N., Schwanethal, J. P., Postberg, F., Srama, R., ... Grün, E. (2007b). The composition of Saturn's e ring. *Monthly Notices of the Royal Astronomical Society*, 377(4), 1588–1596. <http://doi.org/10.1111/j.1365-2966.2007.11710.x>
- Hillier, J. K., McBride, N., Green, S. F., Kempf, S., & Srama, R. (2006). Modelling CDA mass spectra. *Planetary and Space Science*, 54(9–10), 1007–1013. <http://doi.org/10.1016/j.pss.2006.05.013>
- Horanyi, M., Szalay, J. R., Kempf, S., Schmidt, J., Grün, E., Srama, R., & Sternovsky, Z. (2015). A permanent, asymmetric dust cloud around the Moon. *Nature*, 522(7556), 324–326. <http://doi.org/10.1038/nature14479>
- Hornung, K., & Drapatz, S. (1981). *Residual ionization after impact of large dust particles*. The Comet Halley Probe. Plasma Environ. (ESA).
- Howett, C. J. A., Spencer, J. R., Hurford, T., Verbiscer, A., & Segura, M. (2016). Thermal properties of Rhea's poles: Evidence for a meter-deep unconsolidated subsurface layer. *Icarus*, 272, 140–148. <http://doi.org/10.1016/j.icarus.2016.02.033>
- Hsu, H.-W., Postberg, F., Sekine, Y., Shibuya, T., Kempf, S., Horányi, M., ... Srama, R. (2015). Ongoing hydrothermal activities within Enceladus. *Nature*, 519(7542), 207–10. <http://doi.org/10.1038/nature14262>
- Iess, L., Stevenson, D. J., Parisi, M., Hemingway, D., Jacobson, R. a, Lunine, J. I., ... Tortora, P. (2014). The Gravity Field and Interior Structure of Enceladus. *Science*, 344(6179), 78–80. <http://doi.org/10.1126/science.1250551>
- Jones, G. H., Roussos, E., Krupp, N., Beckmann, U., Coates, A. J., Crary, F. J., ... Young, D. (2008). The dust halo of Saturn's largest icy moon, Rhea. *Science (New York, N.Y.)*, 319(5868), 1380–1384. <http://doi.org/10.1126/science.1151524>
- Kempf, S. (2007). *Saturnian Dust: Rings, Ice Volcanoes, and Streams (Habilitationsschrift)*. MPI for Nuclear Physics, Heidelberg, Germany.
- Kempf, S., Beckmann, U., Moragas-Klostermeyer, G., Postberg, F., Srama, R., Economou, T., ... Grün, E. (2008). The E ring in the vicinity of Enceladus. I. Spatial distribution and properties of the ring particles. *Icarus*, 193(2), 420–437. <http://doi.org/10.1016/j.icarus.2007.06.027>
- Kempf, S., Srama, R., Postberg, F., Burton, M., Green, S. F., Helfert, S., ... Grün, E.

- (2005). Composition of saturnian stream particles. *Science (New York, N.Y.)*, 307(5713), 1274–1276. <http://doi.org/10.1126/science.1106218>
- Korth, A., Krueger, F. R., Mendis, D. A., & Mitchell, D. L. (1990). Organic ions in the coma of comet Halley (Vol. AMC89). Asteroid, comets, meteor III, proceedings of a meeting at the Astronomical Observatory of the Uppsala University. Retrieved from <http://adsabs.harvard.edu/abs/1990acm..proc..373K>
- Korth, A., Marconi, M. L., Mendis, D. A., Krueger, F. R., Richter, A. K., Lin, R. P., ... D'Uston, C. (1989). Probable detection of organic-dust-borne aromatic C₃H₃⁺ ions in the coma of comet Halley. *Nature*. <http://doi.org/10.1038/337053a0>
- Kriegel, H. (2013). *The Plasma Environments of Saturn's Moons Enceladus and Rhea: Modeling of Cassini Magnetic Field Data (PhD Thesis)*. Technische Universität Braunschweig, Germany.
- Krivov, A. V., Sremčević, M., Spahn, F., Dikarev, V. V., & Kholshchevnikov, K. V. (2003). Impact-generated dust clouds around planetary satellites: Spherically symmetric case. *Planetary and Space Science*, 51(3), 251–269. [http://doi.org/10.1016/S0032-0633\(02\)00147-2](http://doi.org/10.1016/S0032-0633(02)00147-2)
- Krüger, H., Krivov, A. V., Sremčević, M., & Grün, E. (2003). Impact-generated dust clouds surrounding the Galilean moons. *Icarus*, 164(1), 170–187. [http://doi.org/10.1016/S0019-1035\(03\)00127-1](http://doi.org/10.1016/S0019-1035(03)00127-1)
- Krüger, H., Linkert, G., Linkert, D., Moissl, R., & Grün, E. (2005). Galileo long-term dust monitoring in the jovian magnetosphere. *Planetary and Space Science*. <http://doi.org/10.1016/j.pss.2005.04.009>
- Larson, S. M., Fountain, J. W., Smith, B. A., & Reitsema, H. J. (1981). Observations of the Saturn E ring and a new satellite. *Icarus*, 47, 288–290.
- Lavila, P. (2002). *Analyzing time-of-flight spectra of CDA*. Max-Planck-Institut für Kernphysik, Heidelberg.
- McKinnon, W. B. (2015). Effect of Enceladus's rapid synchronous spin on interpretation of Cassini gravity. *Geophysical Research Letters*, 42(7), 2137–2143. <http://doi.org/10.1002/2015GL063384>
- McLafferty, F. W., & Turecek, F. (1993). *Interpretation of mass spectra*. University Science Books, California (Vol. 4).
- Mocker, A. (2011). *Comparison of impact ionisation plasma with laser ionisation (PhD Thesis)*. The Ruperto-Carola University of Heidelberg, Germany.
- Mocker, A., Grun, E., Sternovsky, Z., Drake, K., Kempf, S., Hornung, K., & Srama, R. (2012). On the applicability of laser ionization for simulating hypervelocity impacts. *Journal of Applied Physics*, 112(10). <http://doi.org/10.1063/1.4765716>
- NASA, ESA, and M. L. and the H. 20th A. T. (STScI). (2010). Starry-Eyed Hubble Celebrates 20 Years of Awe and Discovery. Retrieved August 3, 2016, from <http://hubblesite.org/newscenter/archive/releases/2010/13/image/f/>
- Nimmo, F., Spencer, J. R., Pappalardo, R. T., & Mullen, M. E. (2007). Shear heating as the origin of the plumes and heat flux on Enceladus. *Nature*, 447(7142), 289–291. <http://doi.org/10.1038/nature05783>
- Patthoff, D. A., & Kattenhorn, S. A. (2011). A fracture history on Enceladus provides evidence for a global ocean. *Geophysical Research Letters*, 38(18). <http://doi.org/10.1029/2011GL048387>
- Porco, C. C., Helfenstein, P., Thomas, P. C., Ingersoll, a P., Wisdom, J., West, R., ...

- Squyres, S. (2006). Cassini observes the active south pole of Enceladus. *Science (New York, N.Y.)*, 311(5766), 1393–1401. <http://doi.org/10.1126/science.1123013>
- Postberg, F. (2007). *A New View on the Composition of Dust in the Solar System: Results from the Cassini Dust Detector (PhD Thesis)*. The Ruperto-Carola Heidelberg University, Germany.
- Postberg, F., Grün, E., Horanyi, M., Kempf, S., Krüger, H., Schmidt, J., ... Trieloff, M. (2011b). Compositional mapping of planetary moons by mass spectrometry of dust ejecta. *Planetary and Space Science*, 59(14), 1815–1825. <http://doi.org/10.1016/j.pss.2011.05.001>
- Postberg, F., Kempf, S., Hillier, J. K., Srama, R., Green, S. F., McBride, N., & Grün, E. (2008). The E-ring in the vicinity of Enceladus. II. Probing the moon's interior-The composition of E-ring particles. *Icarus*, 193(2), 438–454. <http://doi.org/10.1016/j.icarus.2007.09.001>
- Postberg, F., Kempf, S., Schmidt, J., Brilliantov, N., Beinsen, a, Abel, B., ... Srama, R. (2009a). Sodium salts in E-ring ice grains from an ocean below the surface of Enceladus. *Nature*, 459(June), 1–4. <http://doi.org/10.1038/nature08046>
- Postberg, F., Schmidt, J., Hillier, J., Kempf, S., & Srama, R. (2011a). A salt-water reservoir as the source of a compositionally stratified plume on Enceladus. *Nature*, 474(7353), 620–622. <http://doi.org/10.1038/nature10175>
- Ratcliff, P. R., & Allahdadi, F. (1996). Characteristics of the plasma from a 94 kms⁻¹ micro-particle impact. *Advances in Space Research*, 17(12), 87–91. [http://doi.org/10.1016/0273-1177\(95\)00763-5](http://doi.org/10.1016/0273-1177(95)00763-5)
- Schmidt, J., Brilliantov, N., Spahn, F., & Kempf, S. (2008). Slow dust in Enceladus' plume from condensation and wall collisions in tiger stripe fractures. *Nature*, 451(7179), 685–688. <http://doi.org/10.1038/nature06491>
- Seal, D. (2004). Saturn Satellites, Rings. Retrieved September 5, 2016, from <https://saturn.jpl.nasa.gov/resources/1615/>
- Showalter, M. R. (1998). Detection of centimeter-sized meteoroid impact events in Saturn's F ring. *Science (New York, N.Y.)*, 282(5391), 1099–1102. <http://doi.org/10.1126/science.282.5391.1099>
- Smith, B. A., Soderblom, L., Batson, R., Bridges, P., Inge, J., Masursky, H., ... Suomi, V. E. (1982). A new look at the saturn system: the voyager 2 images. *Science (New York, N.Y.)*, 215(4532), 504–37. <http://doi.org/10.1126/science.215.4532.504>
- Smith, R. M. (2004). Understanding mass spectra: A basic approach. *John Wiley & Sons, Inc.*, 2, 287–352. <http://doi.org/10.1002/0471221074.anw1>
- Spahn, F. (2006). Cassini Dust Measurements at Enceladus and Implications for the Origin of the E Ring. *Science*, 311(5766), 1416–1418. <http://doi.org/10.1126/science.1121375>
- Spahn, F., Albers, N., Hörning, M., Kempf, S., Krivov, A. V., Makuch, M., ... Miodrag Sremcevic (2006). E ring dust sources: Implications from Cassini's dust measurements. *Planetary and Space Science*, 54(9–10), 1024–1032. <http://doi.org/10.1016/j.pss.2006.05.022>
- Spahn, F., Schmidt, J., Albers, N., Hörning, M., Makuch, M., Seiss, M., ... Grün, E. (2006). Cassini dust measurements at Enceladus and implications for the origin of the E ring. *Science (New York, N.Y.)*, 311(5766), 1416–1418. <http://doi.org/10.1126/science.1121375>
- Spencer, J. R., & Nimmo, F. (2013). Enceladus: An Active Ice World in the Saturn

- System. *Annual Review of Earth and Planetary Sciences*, 41(1), 693–717.
<http://doi.org/10.1146/annurev-earth-050212-124025>
- Spencer, J. R., Pearl, J. C., Segura, M., Flasar, F. M., Mamoutkine, a, Romani, P., ... Lopes, R. M. C. (2006). Cassini encounters Enceladus: background and the discovery of a south polar hot spot. *Science (New York, N.Y.)*, 311(5766), 1401–1405. <http://doi.org/10.1126/science.1121661>
- Srama, R. (2009). *Cassini-Huygens and Beyond-Tools for Dust Astronomy (Habilitationsschrift)*. Universität Stuttgart, Germany.
- Srama, R., Ahrens, T. J., Altobelli, N., Auer, S., & Bradley, J. G. (2004). THE CASSINI COSMIC DUST ANALYZER 1 . Introduction The Cassini-Huygens mission provides the opportunity for a thorough investigation of the interplanetary dust complex and the saturnian dust environment . The scientific objectives were stated in our prop, 465–518.
- Srama, R., Ahrens, T. J., Altobelli, N., Auer, S., Bradley, J. G., Burton, M., ... Zook, H. A. (2004). The Cassini cosmic dust analyzer. *Space Science Reviews*, 114(1–4), 465–518. <http://doi.org/10.1007/s11214-004-1435-z>
- Srama, R., Woiwode, W., Postberg, F., Armes, S. P., Fujii, S., Dupln, D., ... Gr??n, E. (2009). Mass spectrometry of hyper-velocity impacts of organic micrograins. *Rapid Communications in Mass Spectrometry*, 23(24), 3895–3906. <http://doi.org/10.1002/rcm.4318>
- Sremčević, M., Krivov, A. V., Krüger, H., & Spahn, F. (2005). Impact-generated dust clouds around planetary satellites: Model versus Galileo data. *Planetary and Space Science*, 53(6), 625–641.
<http://doi.org/10.1016/j.pss.2004.10.001>
- Teolis, B. D., & Waite, J. H. (2016). Dione and Rhea seasonal exospheres revealed by Cassini CAPS and INMS. *Icarus*, 272, 277–289.
<http://doi.org/10.1016/j.icarus.2016.02.031>
- Thomas, P. C., Tajeddine, R., Tiscareno, M. S., Burns, J. A., Joseph, J., Lored, T. J., ... Porco, C. (2016). Enceladus's measured physical libration requires a global subsurface ocean. *Icarus*, 264, 37–47.
<http://doi.org/10.1016/j.icarus.2015.08.037>
- Thomson, J. J. (1913). On the appearance of helium and neon in vacuum tubes. *Nature*, 90, 645–647.
- Timmerman, R., & Grün, E. (1991). Plasma emission from high velocity impacts of microparticles onto water ice. *IAU Colloq*, 126, 375–377.
- Tobie, G., Cadek, O., & Sotin, C. (2008). Solid tidal friction above a liquid water reservoir as the origin of the south pole hotspot on Enceladus. *Icarus*, 196(2), 642–652. <http://doi.org/10.1016/j.icarus.2008.03.008>
- Verbiscer, A. J., Skrutskie, M. F., & Hamilton, D. P. (2009). Saturn's largest ring. *Nature*, 461(7267), 1098–100. <http://doi.org/10.1038/nature08515>
- Waite, J. H., Combi, M. R., Ip, W.-H., Cravens, T. E., McNutt, R. L., Kasprzak, W., ... Tseng, W.-L. (2006). Cassini ion and neutral mass spectrometer: Enceladus plume composition and structure. *Science (New York, N.Y.)*, 311(5766), 1419–1422. <http://doi.org/10.1126/science.1121290>
- Waite Jr, J. H., Lewis, W. S., Magee, B. a., Lunine, J. I., McKinnon, W. B., Glein, C. R., ... Ip, W.-H. (2009). Liquid water on Enceladus from observations of ammonia and 40Ar in the plume. *Nature*, 460(7259), 1164–1164.
<http://doi.org/10.1038/nature08352>
- Wiederschein, F., Vöhringer-Martinez, E., Beinsen, A., Postberg, F., Schmidt, J.,

Srama, R., ... Abel, B. (2015). Charge separation and isolation in strong water droplet impacts. *Physical Chemistry Chemical Physics : PCCP*, 17(10), 6858–64. <http://doi.org/10.1039/c4cp05618c>

Acknowledgement

First and foremost, I want to thank my advisor PD. Dr. Frank Postberg for his multi-perspective and vigorous research approach. I am extremely thankful for his continuous support, patience, time and immense guidance to make my PhD research time productive. I highly regard the efforts he put in improving my skills, providing constructive criticism and being there during the tough times. I am sincerely thankful to him for embarking me into a number of scientific meetings and giving me opportunities to enrich my research experience.

Thanks to other members of my PhD committee: PD Dr.-Ing. Ralf Srama, Prof. Dr. Mario Trieloff and Prof. Dr. Frank Keppler. Special thanks goes to Dr. Ralf Srama for his valuable input and to Prof Mario Trieloff for his efforts to resolve many administrative issues during the entire period of my PhD. Thanks to Petra Fuchs for being so helpful and kind in all the official matters.

I acknowledge funding through the Deutsche Forschungsgesellschaft (DFG) by the grants PO 1015/2-1 and PO 1015/3-1.

I would like to say a sincere thanks to Prof. Dr. Sascha Kempf, Dr. Jon Hillier and Dr. Sean Hsu for their help and guidance. I highly appreciate Prof. Dr. H. F. Schöler and Tobias for their useful discussions during the course of my PhD.

I am grateful to the whole Cosmic-dust group, especially, Dr. Yanwei Li, Dr. Katherina Fiege, Sebastian Bugiel and Geo-Cosmo chemistry group, especially Dr. Winfried Schwarz. Thank you Elizabeth and Klaus for providing me homely environment during my entire stay with you. Thanks to Dr. Ritesh Kumar and, especially to Dr. Muhammad Kashif for his immense support during tough times.

Rene, I am grateful for your support during the entire period of my PhD that erased the boundary between colleague and friend. I appreciate Lenz and Fabian for their support to finalize my write-up. Thank you Massimo (PhD soon) for your help on many occasions.

Saira (PhD soon), thank you so much for always being there. Words would never be enough to thank you for your constant intellectual inputs, immense support and enjoyable coffee chats. Thanks a lot!

I am thankful from the core of my heart to my wife (Husna) and daughters (Raeha & Shifa) for their patience, love, encouragement and unshakable faith in me to bring dream into reality. Warm thanks to my brothers (Umair, Ayaz, Ozair, Asad) and my sister (Shumaila) for their continuous support, and to my parents-in-law, especially great affectionate (Late) Prof. Khadim Hussain for his prayers.

Finally, I am indebted to my parents (Muhammad A. Khawaja & Shamma Khawaja). The only motivation to fulfill this task was to present a gift to you in the form of my PhD. Thank you my dear "Abu Jee" (father in my language) to keep me motivated during all this time. I really owe this PhD to you.

**Eidesstattliche Versicherung gemäß § 8 der Promotionsordnung
der Naturwissenschaftlich-Mathematischen Gesamtfakultät
der Universität Heidelberg**

1. Bei der eingereichten Dissertation zu dem Thema

Organic compounds in Saturn's E-ring and its
compositional profile in the vicinity of Rhea

handelt es sich um meine eigenständig erbrachte Leistung.

2. Ich habe nur die angegebenen Quellen und Hilfsmittel benutzt und mich keiner unzulässigen Hilfe Dritter bedient. Insbesondere habe ich wörtlich oder sinngemäß aus anderen Werken übernommene Inhalte als solche kenntlich gemacht.

3. Die Arbeit oder Teile davon habe ich ~~wie folgt~~ bislang nicht¹⁾ an einer Hochschule des In- oder Auslands als Bestandteil einer Prüfungs- oder Qualifikationsleistung vorgelegt.

Titel der Arbeit: _____

Hochschule und Jahr: _____

Art der Prüfungs- oder Qualifikationsleistung: _____

4. Die Richtigkeit der vorstehenden Erklärungen bestätige ich.

5. Die Bedeutung der eidesstattlichen Versicherung und die strafrechtlichen Folgen einer unrichtigen oder unvollständigen eidesstattlichen Versicherung sind mir bekannt.

Ich versichere an Eides statt, dass ich nach bestem Wissen die reine Wahrheit erklärt und nichts verschwiegen habe.

Heidelberg, 15.11.2016

Ort und Datum

Unterschrift

¹⁾ Nicht Zutreffendes streichen. Bei Bejahung sind anzugeben: der Titel der andernorts vorgelegten Arbeit, die Hochschule, das Jahr der Vorlage und die Art der Prüfungs- oder Qualifikationsleistung.